

THREE-DIMENSIONAL SEGMENTATION OF AIR-VOID SYSTEM IN
HARDENED CONCRETE USING PHOTOMETRIC STEREO
AND ARTIFICIAL INTELLIGENCE METHODS

by

Jueqiang Tao, M.S.

A dissertation submitted to the Graduate Council of
Texas State University in partial fulfillment
of the requirements for the degree of
Doctor of Philosophy
with a Major in Material Science, Engineering, and Commercialization
August 2022

Committee Members:

Feng Wang, Chair

Anthony Torres

Byron Gao

Xijun Shi

Yaxiong Huang

COPYRIGHT

by

Jueqiang Tao

2022

FAIR USE AND AUTHOR'S PERMISSION STATEMENT

Fair Use

This work is protected by the Copyright Laws of the United States (Public Law 94-553, section 107). Consistent with fair use as defined in the Copyright Laws, brief quotations from this material are allowed with proper acknowledgement. Use of this material for financial gain without the author's express written permission is not allowed.

Duplication Permission

As the copyright holder of this work I, Jueqiang Tao, authorize duplication of this work, in whole or in part, for educational or scholarly purposes only.

ACKNOWLEDGEMENTS

First and foremost, I would like to thank my advisor, Dr. Feng Wang, for his continuous guidance and support throughout my Ph.D. study. Dr. Wang is a highly respected advisor with excellent professional experiences and great accomplishments. Working side-by-side with him was a great experience, which helped me to achieve my goal at Texas State University. Beyond academia, he has provided valuable advice on my career development. Thank you for sharing your research and life experience with me, which would benefit my whole life.

My greatest appreciation also goes to my dissertation committee members, Dr. Anthony Torres, Dr. Byron Gao, Dr. Robin Huang, and Dr. Xijun Shi. I have greatly benefited from their constructive advice and tremendous effort in improving my research.

I would like to extend my gratitude to all my Ph.D. fellows and friends, including Xiaohua Luo, and Haitao Gong. Without your help and accompany, it can be difficult for me to accomplish my dissertation.

Last but not the least, I want to thank my family for their understanding and support throughout my life. This journey would not have been possible without their solid backup.

TABLE OF CONTENTS

	Page
ACKNOWLEDGEMENTS.....	iv
LIST OF TABLES.....	viii
LIST OF FIGURES.....	ix
LIST OF ABBREVIATIONS.....	xi
ABSTRACT.....	xiii
CHAPTER	
1. INTRODUCTION.....	1
1.1 Statement of Problem.....	1
1.2 Objective of Research.....	2
1.3 Dissertation Organization.....	3
2. LITERATURE REVIEW.....	5
2.1 Air-Void Segmentation Methods.....	5
2.1.1 Conventional Approaches.....	5
2.1.2 Contrast Enhancement Based Approaches.....	6
2.1.3 X-ray CT Based Approaches.....	11
2.1.4 Deep Learning Based Approaches.....	13
2.2 Three-Dimension Reconstruction Methods - Photometric Stereo Method.....	16
2.3 Air-Void System Measurement Approaches.....	20
2.3.1 Conventional Approaches.....	20
2.3.2 Stereological Approaches.....	22
2.4 Summary.....	26
3. METHODOLOGY.....	29
3.1 Concrete Surface Normal Reconstruction Methods.....	29
3.1.1 Photometric Stereo.....	30
3.2 Air-Void Segmentation Approaches.....	35
3.2.1 Conventional Segmentation Methods.....	35

3.2.3 Convolution Neural Networks	39
3.3 Stereological Analysis – the Saltykov Method	41
3.3.1 Estimation of In-Section Air Voids	42
3.3.2 Estimation of Out-Section Air Voids.....	45
4. AUTOMATED IMAGE SEGMENTATION OF AIR VOIDS IN HARDENED CONCRETE USING PHOTOMETRIC STEREO THREE-DIMENSIONAL RECONSTRUCTION METHOD	47
4.1 Data Acquisition and Description.....	48
4.1.1 Instrument Setup	48
4.1.2 Hardened Concrete Samples	50
4.2 Accuracy Assessment	52
4.3 Results and Analysis.....	53
4.3.1 Surface Normal Reconstruction.....	53
4.3.2 Air-Void Segmentation.....	56
4.4 Summary.....	66
5. REFINEMENT OF THE AUTOMATED AIR-VOID SEGMENTATION RESULTS USING DEEP LEARNING METHODS	69
5.1 Data Acquisition and Description.....	70
5.1.1 Hardened Concrete Samples.....	70
5.1.2 Data Annotation and Registration.....	71
5.1.3 Surface Normal Image Capturing	73
5.2 Image Augmentation.....	75
5.3 Accuracy Assessment	76
5.4 Results and Analysis.....	77
5.4.1 Surface Normal Image Generated Using Photometric Stereo Method	77
5.4.2. Evaluation of Different Augmentation Strategies.....	80
5.4.3 Air-Void Segmentation Results of U-Net model.....	81
5.5 Summary.....	92
6. EVALUATION OF THE SALTYKOV METHOD FOR RESTORING SPATIAL AIR-VOID DISTRIBUTION	94
6.1. Synthetic Spatial Air-void Model	95
6.1.1 Construction of Spatial Air-Void Model	95
6.1.2 Visualization of Spatial Air-Void Model.....	100
6.2. Evaluation of Influence Factors for 2D and 3D PPV Analysis	104

6.3. Accuracy Assessment	108
6.4. Results and Analysis	110
6.4.1 In-Section Air Voids	112
6.4.2 Out-Section Air Voids	117
6.5 Summary	122
7. CONCLUSIONS.....	124
7.1 Summary of Observations.....	124
7.2 Innovations.....	126
7.3 Future Works	127
REFERENCES	129

LIST OF TABLES

Table	Page
1. Technical Specifications of Sony α 7R II CCD Camera and Sony FE 50 mm F2.8 Macro Lenses	50
2. Description of Concrete Samples.....	51
3. Segmentation Accuracy for Concrete Specimens.....	66
4. Description of experimental specimens	71
5. Augmentation strategies.....	75
6. Training results of U-Net model using different augmentation strategies.....	81
7. Accuracy measurement for testing samples.....	88
8. U-Net models trained with different image sizes	88
9. Accuracy measurement for testing samples using U-Net512	90
10. Air-void Parameters Measured on U-Net512 results and Ground Truth using Point Count Method	91
11. Parameters used for the construction of synthetic air-void model.....	100

LIST OF FIGURES

Figure	Page
1. Contrast Enhancement Based Automated Air-Void Segmentation Method.....	8
2. Schematic Diagram of Photometric Stereo.....	19
3. The Cross Profile of Air Voids in Polished Concrete Surface.....	21
4. The illustration of the piecewise linear function.....	34
5. Flow chart of 3D air voids segmentation.....	36
6. N_t , N_{xoy} and θ on concrete surface	37
7. U-Net for image with resolution of 256 pixels \times 256 pixels	40
8. Steps of U-Net model training.....	41
9. Six LED light photometric stereo system	48
10. Concrete specimen images.....	52
11. Concrete specimen surface	54
12. Reconstructed 3D surfaces.....	55
13 . Gaussian filter processed concrete surface profile.....	57
14. Air voids segmentation result with rectified concrete surface.....	58
15. Measurement results of surface angle θ	60
16. Air voids segmentation results with surface angle thresholds 15°, 27° and 35°	61
17. Segmentation result using FillHole.....	63
18. Segmentation result using AreaRatio.....	64
19. Segmentation accuracy under various of area ratios.....	64
20. An example of the manually annotated air-void image.	73

21. Illustration of surface normal vector on a concrete surface.....	74
22. Mapping surface normal to RGB space.....	74
23. Augmented images using different augmentation strategies	76
24. The air voids in original concrete surface image and surface normal image.....	78
25. Air-void appearances and air-void like noises generated by components on concrete surfaces.	79
26. The loss and MIoU curves of the U-Net model training.	81
27. Accuracy measurement of test samples with different thresholds.....	83
28. Air-void segmentation results of test concrete samples.....	84
29. Random cropping using different cut sizes.....	87
30. Air-void segmentation results of test concrete samples using U-Net512.....	89
31. Flow chart for constructing the synthetic air-void model.....	99
32. Visualization of the synthetic air-void model.....	101
33. The distribution and probability plot of the air void count distribution in each synthetic air-void model	102
34. Diagram for the in-section and out-section air voids intersected with a concrete plane.....	106
35. PPV analysis using the air-void information from 2D and 3D perspective.....	107
36. Diagram of difference between two distributions.....	110
37. Diagram for appending air-void intersections from different slices.....	111
38. Unfolding error rate with different air-void observations and bin classes.....	114
39. Comparison of actual void distribution and unfolding results.....	116
40. Unfolding results for out-section air voids	117
41. Unfolding results for out-section air voids with error rate	119

LIST OF ABBREVIATIONS

Abbreviation	Description
1D	One dimensional
2D	Two dimensional
3D	Three dimensional
ACE	Automated Concrete Evaluation
AI	Artificial Intelligence
BRDF	Bidirectional Reflectance Distribution Function
CCD	Charge-Coupled Device
CMOS	Complementary Metal Oxide Semiconductor
CRF	conditional random field
CT	Computed Tomography
DCNN	Deep Convolutional Neural Networks
DL	Deep Learning
FCN	Fully Convolutional Network
GPUs	Graphics Processing Units
LED	Light-Emitting Diode
MIoU	Mean of Intersection over Union
MoDOT	Missouri Department of Transportation
MRFs	Markov Random Fields
PPV	Protected Paste Volume

RCNN	Region-based Convolutional Neural Network
RGB	Red, Green, and Blue
RGB-D	Red, Green, Blue, and Depth
SBL	Sparse Bayesian Regression method
TxDOT	Texas Department of Transportation

ABSTRACT

A well-distributed air-void system inside a hardened concrete can help protect the concrete structure from being damaged by freeze-thaw cycles. The concrete air-void petrographic test, which is specified in ASTM C457, is the standard test procedure for characterizing the air-void system and evaluating the freeze-thaw performance of hardened concrete samples. Specifically, the linear-traverse method (Procedure A) and the modified point-count method (Procedure B) are two manual methods described in ASTM C457. These two methods are based on manually microscopical observation. In addition, considering the fact that air voids in hardened concrete surfaces are difficult to be observed with the naked eye due to the low contrast between air voids and hardened cement paste, the identification of air voids is difficult and subjective. Consequently, Procedures A and B are error-prone and labor-intensive. The contrast enhanced method (Procedure C) was introduced in ASTM C457 as a computer-aided air-void system measurement method. Procedure C requires the aid of contrast enhancement, in which the air voids are manually highlighted with color on the concrete surface by an experienced human rater. Then, the air-void system can be automatically measured with the assistance of computer-aided image processing techniques. However, during the contrast enhancement procedure, voids in aggregates and cracks can also be filled with white powders, which is not wanted and needs to be carefully checked and avoided. As a result, although Procedure C reduces human labor to some degree, it is still labor-intensive and time-intensive. Therefore, a more efficient air-void measurement method that can

automatically identify the air voids from hardened concrete surfaces needs to be developed.

This dissertation aims to investigating the detection of the air-void system in hardened concrete surfaces using three-dimensional (3D) reconstruction and Artificial Intelligence (AI) techniques. The proposed method can be considered as an extension of Procedure C but is free from the manual contrast enhancement procedures. In this dissertation, a new air-void detection method was proposed to automatically segment the air-void system from the solid phase in an automated manner. The proposed method includes: 1) a 3D image reconstruction system based on two-dimensional (2D) image data collection, and a delicate and novel engineering design for hardware; 2) an automated air-void segmentation method without using contrast enhancement pre-processing. According to our knowledge, the method is innovative and has not been attempted before. Unlike other existing methods that have been used in the research and industry, the method we proposed has the following potential advantages: less labor/time-intensity, higher cost-effectiveness, and higher accuracy. The research results showed that the basic photometric stereo method is able to contrast the air voids in hardened concrete surfaces to some extent using the 3D nature of air voids. It took 10-15 seconds for the basic photometric stereo method to reconstruct the surface normal image for each concrete sample. However, the polished concrete surface cannot be considered as an ideal Lambertian surface, and some air-void like noises can be generated due to the bias of the basic photometric stereo method. The deep learning based image segmentation method

provided good robustness to differentiate most of the noises from true positive air voids. The experimental results showed that the deep learning based methods can accurately distinguish air voids from hardened concrete images with the detection accuracy of over 0.9 in only less than a minute. The accuracy rates for air content, specific surface, and spacing factor were 0.92, 0.91, and 0.89, respectively.

In addition, considering the limitations of using 2D air-void segmentation for concrete petrographic analysis, the reliability of using the Saltykov method to restore the 3D air-void radius was also evaluated. The recovered spatial air-void distribution can be used to simulate the actual air-void system inside hardened concrete and then provide insights into the percentage of the hardened concrete paste that is protected by the air-void system. In this research, the unfolding results of both in-section air voids and out-section air voids are evaluated using the Minkowski Distance metric. The research results showed that the up-to-date methods can accurately unfold the size distribution of in-section air voids, while the methods failed to achieve an accurate estimation for out-section air voids.

1. INTRODUCTION

1.1 Statement of Problem

Concrete is widely used in buildings, bridges, pavements, airports, and dams due to its high strength, long durability, and low maintenance needs. The concrete transportation infrastructures in cold regions are exposed to frost penetration and freezing conditions. Freezing water expands by 9% in volume and produces pressure in the pores of the concrete (Yeon and Kim 2018). The accumulative effects of successive freeze-thaw cycles and loads could eventually lead to cracking, scaling, and spalling on concrete pavements and then cause deterioration of pavement performance (Adkins and Christiansen 1989). The air-void system with uniformly dispersed small air bubbles shortens the distance between any point in cement paste and an air void and helps the concrete release the pressure build-up under freezing conditions (Walker et al. 2006).

Characterization of the air-void system in hardened concrete and explaining the mechanism of the protection of air voids has been a difficult challenge for many years. Powers and his colleague first introduced the concept of spacing factor of air voids and tried using the hydraulic pressure theory to explain the freeze-thaw resistance of concrete (Powers and Willis 1950). Though Power's theory is generally accepted, several refined theories have been suggested that better reconcile experimental observations with theory (Rashed and Williamson 1991, Chatterji 2003). Currently, linear-traverse method and modified point count method which are specified in the ASTM C457 'Standard Test Method for Microscopical Determination of Parameters of the Air-Void System in Hardened Concrete' are common methods used for air-void parameter measurement (ASTM 2012). Both methods are human operator dependent, and the

measurement results are subjective. In addition, these methods can be considered as sampling surveys and the measurement is limited to one-dimension (1D), while the air voids are actually distributed in a three-dimensional (3D) space in hardened concrete. Snyder et al. (Snyder et al. 1991) conducted an analytical investigation of the effect of the number of air voids on the minimum expected error. The research results showed that no accuracy can be further achieved until more than 2,000 air voids are observed and thus the conventional air-void measurement method is time-consuming, labor-intensive, and error-prone.

1.2 Objective of Research

Conventional air-void measurement methods are tedious and hard on the eyes. A single determination of the air-void parameters of a concrete specimen by means of the linear traverse method can take up to 7h, depending on the size and quantity of the voids. A technician cannot spend more than 4h per day doing this sort of work on a day-to-day basis(Walker et al. 2006). Due to the heavy labor, air-void analysis using ASTM C457 costs approximately \$450 to \$500 for each concrete sample(Anon). Many research studies have been done on replacing human operators with machine vision or automated image analysis (Peterson et al. 2001b, Pleau et al. 2001, Liu et al. 2017). In these studies, a concrete surface is commonly contrast-enhanced to make it easier for computers to distinguish air voids from the solid phase (aggregates and paste). The contrast enhancement method creates a contrast between the air voids and the solid phase by blackening the entire surface with black ink and filling the voids with white powder. Although the workload of the original ASTM C457 measurement has been significantly reduced by these innovations, the cost for contrast enhancement work is still

considerable. In addition, inappropriate selection of contrast enhancement materials will lead to a significantly biased result. Consequently, there is a need to develop a fully automated air-void analysis solution without contrast enhancement.

In this dissertation research, considering the 3D nature of air voids in hardened concrete surfaces, the feasibility of utilizing 3D information (e.g. depth and gradient) to distinguish the air voids in hardened concrete surfaces was investigated. The photometric stereo method, one major component of vision-based 3D techniques, which has been effectively used in reverse engineering, industrial testing, and archaeology due to its advantages of simple operation, high resolution, and low cost was utilized to capture the 3D information of the air voids. Consequently, an automated air-void segmentation method without using contrast enhanced pre-processing was proposed, which further reduces the labor cost and improves the measurement accuracy of the ASTM C457 procedure. Finally, the Saltykov method, a stereological analysis method that infers the true spatial air-void distribution in the hardened paste will be evaluated.

1.3 Dissertation Organization

The remainder of this dissertation is organized as follows:

Chapter 2 provided a comprehensive review of the state-of-the-art research on image segmentation methods, 3D reconstruction methods, and stereological methods. The limitation and applicability of current research studies were analyzed.

Chapter 3 described the details of 3D reconstruction methods, image segmentation methods, and stereological analysis methods used in this research.

Chapter 4 compared various 3D reconstruction methods for the restoration of the 3D

hardened concrete surfaces. A conventional image segmentation procedure was proposed for segmenting the air voids from the 3D concrete surface images based on the profile and depth information.

Chapter 5 investigated the adoption of using deep learning based methods to furtherly refine the air-void segmentation using the 3D concrete surface images. An image dataset with original hardened concrete surface images, concrete surface normal images, and pixel-level air-void annotations was developed. The effect of different image augmentation techniques and hyperparameter settings were investigated.

Chapter 6 investigated the reliability of the Saltykov method for restoring spatial air-void distribution. A set of synthetic air-void models were developed as ground truth. Various influence factors such as the number of air-void observations and bin classes were analyzed.

Chapter 7 presented the main conclusion drawn upon the entire dissertation research. The innovations of the research study were also highlighted. In addition, future works were demonstrated to refine and improve the current dissertation research study.

2. LITERATURE REVIEW

2.1 Air-Void Segmentation Methods

The spacing factor is an air-void parameter that is frequently used to measure the relative distance between air voids and the measurement value is equal to half of the average distance between air voids (ASTM 2012). Several segmentation methods have been developed to identify the air voids from the hardened concrete for measuring the air-void distribution parameters. In the following subsections, the existing measurement methods, and associated standards and procedures are introduced and reviewed.

2.1.1 Conventional Approaches

In ASTM C457, linear-traverse and modified point count methods are commonly utilized for microscopical determinations of the spacing factor (ASTM 2012). Both methods are human operator-dependent, and the measurement results are subjective. In addition, these methods are considered as sampling surveys and the measurement results are sensitive to the number of air voids observed.

According to ASTM C457, air-void parameters are manually determined and evaluated by human operators who are pre-trained to identify air voids, paste, and aggregates. The judgments which are made by pre-trained human operators are subjective and the results are operator-dependent, which makes the air-void measurement results error-prone. Linear-traverse method and modified point count method are two conventional methods that are commonly utilized for microscopical determinations of the spacing factor (ASTM 2012). In a research study conducted by Saucier et al. (Saucier et al. 1996), 6 concrete specimens were examined by 18 experienced operators, and

significant variations were found from one operator to another. In addition, the manual examination is also time-consuming and requires huge heavy laboring hours. To overcome the low efficiency and the limitations of the subjective manual evaluation process, computer vision based automated air-void segmentation methods were proposed.

2.1.2 Contrast Enhancement Based Approaches

Many research studies have been done on replacing human operators with machine vision or automated image analysis (Peterson et al. 2001b, Pleau et al. 2001, Liu et al. 2017). In these studies, the air voids and solid phase (aggregates and paste) in a concrete surface are commonly contrast-enhanced to make it easier for computers to distinguish. Pleau et al. (Pleau et al. 2001) compared the results from image analysis and visual examination. They found that for air voids in the size interval range of 0–80 μm , the number of air voids identified by the image analysis test system was 50–70% higher than the number of air voids identified by a human operator.

The segmentation of air voids in hardened concrete surfaces is among the most essential and challenging steps for automated air-void measurement. Charge Coupled Device (CCD) camera and flatbed scanner are two main technologies utilized to capture two-dimensional (2D) concrete surface images. The analysis of the air-void system in hardened concrete using 2D digital images was first introduced by Chatterji et al. (Chatterji and Gudmundsson 1977). A contrast enhancement step that made the air voids appear white and the solid phase appear black was proposed in the research. In later studies, the contrast enhancement method was widely adopted for automated air-void system analysis with 2D digital images. The RapidAir 457 proposed by Pade et al. (Pade et al. 2002) was the most widely used contrast enhancement-based automated system.

However, this method was not fully automated, and an operator-determined threshold for segmentation was required. In addition, because additional scans for the same specimen with a CCD camera were required for separating the phase of cement paste, failure to achieve the calibration could make the analysis accuracy jeopardized. Comparing with CCD cameras, a flatbed scanner scans the whole of the specimen surface and fewer calibrations are required for the setting of specimens. Peterson et al. (Peterson et al. 2001b) first introduced the flatbed scanner to collect the polished concrete surfaces. The process is shown in Figure 1.

The air voids, cement paste, and aggregates were well distinguished by manually increasing the contrast between the three phases. Non-stained images, phenolphthalein-stained images, and black & white treated images were the three kinds of images that were taken after each contrast enhancement process. The different Red, Green, and Blue (RGB) channels of these captured images were combined to generate a contrast-enhanced image for image analysis. However, the air voids, paste, and aggregates were still segmented by thresholds that were set manually. Even though the air voids and the solid phase were in enhanced contrast, the grey levels of air voids and solid phase in 2D images could still vary under various lighting conditions.

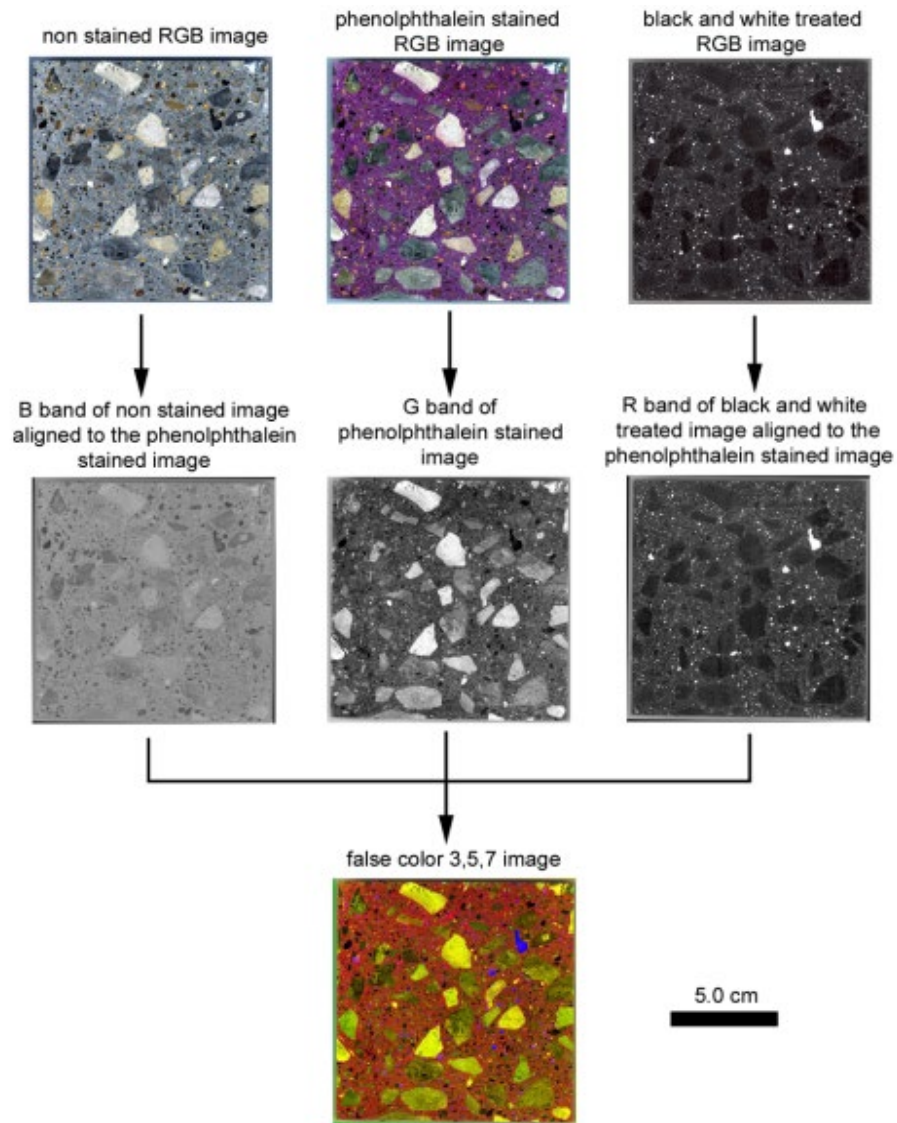


Figure 1. Contrast Enhancement Based Automated Air-Void Segmentation Method

(Peterson et al. 2001b)

Several other automated thresholding strategies were then proposed for the extraction of air voids. The multi-spectral analysis is one of the most widely used methods for air-void thresholding (Peterson et al. 2016). Three RGB histograms were utilized by Zalocha et al. (Zalocha and Kasperkiewicz 2005) to segment air voids and solid phase. Each histogram represented a different channel of an RGB image. The peaks

of the 3 RGB histograms were considered as binarization thresholds for air voids, paste, and aggregates. Fonseca et al. (Fonseca and Scherer 2015) applied an Otsu's method to improve the automation of the air-void segmentation process. In another research study conducted by Song et al. (Song et al. 2017), 20 images were scanned from 6 contrast-enhanced concrete specimens with a flatbed scanner. The spectral-spatial ECHO classifier algorithm which considered both spectral and spatial characteristics of air voids was utilized to automatically classify air voids and the solid phase in the concrete surface. The research results showed a good correlation between the measurement value and reference value.

In 2016, the contrast enhancement based method was included in ASTM C457 as an official procedure. However, the deficiency also quickly revealed itself. The contrast enhancement methods ignore the interior surface of an air void which would be needed for judging whether an observed void is an air void, a hollow fly ash particle, a porosity in aggregates, or a pull-out accidentally made during specimen preparation (Schouenborg et al. 1995). In addition, the pigment which is used for contrast enhancement would fill up air voids, and then the filled air voids later become inaccessible to the white substance (Wolter et al. 2019). According to the description of the sample preparation procedure in ASTM C457, additional verification and rectification would be required for a trained petrographer or technician to either determine the applicability of the contrast enhancement based method to a specific concrete specimen before a contrast enhancement treatment or cover false positive air voids with a very thin tip black sharpie after the contrast enhance treatment (ASTM 2012). Many attempts were done for replacing the contrast-enhancement method by directly distinguishing air voids, paste,

and aggregates. The Missouri Department of Transportation (MoDOT) developed an Automated Concrete Evaluation (ACE) system for automated air-void measurement (Baumgart et al. 2006). The system used a neural network based fuzzy logic classifier method to separate air voids from other features in 2D images using the area and shape characteristics of air voids. Although the ACE system showed good potential for replacing the manual method with an automated image processing method, it was still based on 2D images. One of the advantages of using 3D images is that the uncolored concrete surface is captured and recorded, which gives human raters and the associated computer hardware/software systems the opportunities to review and validate the automated segmentation results. The aforementioned problems could be fundamentally avoided if the air-void segmentation can be done directly on uncolored samples. Song et al. (Song et al. 2020b) first introduced the deep learning techniques for concrete petrographic analysis. The research made a great contribution in segmenting the paste and aggregates without contrast enhancement. The segmentation result was robust to concrete samples with different types of aggregates and paste, and also outperformed the contrast enhancement based method. However, the air voids still need to be contrast-enhanced. In the research conducted by Wolter et al. (Wolter et al. 2019), a photogrammetry method was utilized for the 3D reconstruction of concrete surfaces. The method showed the potential of utilizing 3D reconstruction for air-void segmentation, but large differences were observed between the experiment result and the ground truth. Furthermore, the photogrammetry method was borrowed from commercial software which seems like a black box to other researchers.

2.1.3 X-ray CT Based Approaches

Considering the three-dimensional (3D) nature of air voids, it is reasonable to use 3D technologies to segment the air voids in the polished concrete surface. X-ray Computed Tomography (CT) is a typical non-destructive 3D method that has been widely adopted for the microstructural characterization of materials (Stock 2008). However, the high price of X-ray CT equipment makes it unlikely for practical use for air-void measurement.

Air voids are distributed in the 3D space of hardened concrete and the 3D characteristics of air voids are useful information for distinguishing air voids from other features in a concrete surface image. Consequently, 3D technology could be a useful method to segment air voids in concrete specimens without contrast enhancement. Computed Tomography (CT) has therefore been employed for reliable measurement of air voids. The method not only provides alternative means of measurement, but also presents a unique advantage with its capacity to capture the exact 3D location of all objects of interest and the air-void size distribution, and the derived air-void parameters that are not available to traditional 2D test methods (Lu et al. 2017, Boshoff 2019). However, the air-void analysis of X-ray CT scanned images is also dependent on the thresholding strategies for the segmentation of air voids and solid phase in hardened concrete. Plessis et al. (Du Plessis et al. 2016) introduced a simplified image analysis procedure for air-void segmentation. A global threshold value was first calculated based on the grey value histogram of CT scanned concrete images and the central value between the peaks of material and air voids was selected. Lu et al. (Lu et al. 2018) extracted air voids from Portland cement concrete images using a micro X-ray CT. Both

greyscale value and possible morphologies of air voids were considered in the region-growth based algorithm as an energy function for segmenting air voids from the solid phase. The calculated threshold succeeded in segmenting air voids in hardened cement concrete, while this method was not fully automated because the specific threshold calculated in this research was solely dependent on the specific investigated concrete material. Yun et al. (Yun et al. 2012) quantified and evaluated the paste-void spacing factor in concrete using a CT scanner. In the study, 10,000 random points were selected within an area outside the air voids and the distance from each point to its nearest air-void boundary was measured. The 95th percentile of the cumulative distribution function of the measured data correlated well with the actual spacing factors. Actually, the research revealed one of the resolution defects of the CT method. To achieve a high-resolution CT result for capturing the smallest air voids in hardened concrete, only a small concrete specimen size with 12 mm diameter and 10 mm height was drilled. Therefore, it might be quite challenging to use the CT-based detection method to characterize air voids in large-size specimens or specimens with coarse aggregates. In the research conducted by Lu et al. (Lu et al. 2017), a solution was provided for capturing the air voids in large-size specimens or coarse aggregates in specimens. Two scans were performed on 50 mm and 6 mm cylindrical samples, respectively. The scan on the 50 mm cylindrical sample achieved a resolution of 55 $\mu\text{m}/\text{pixel}$ and could capture the large (entrapped) air voids in hardened concrete. The scan on the 6 mm cylindrical sample achieved a resolution of 9 $\mu\text{m}/\text{pixel}$ and could capture the small (entrained) air voids in hardened concrete. A power law curve was then drawn to generate the distribution of different sizes of air voids.

Bernardes et al. (Bernardes et al. 2015) investigated the influence of the selection of

sample regions on air-void structural parameters. Several cement concrete specimens from different regions of interest were considered in this research. A μ -CT was utilized to scan the porosity of concrete specimens on the 7th and the 28th days, respectively. A reduced porosity was found in the interior of the concrete specimen within 28 days of testing age, but no pronounced reduction near the surface of the samples was found. This highlighted the importance of a good sampling selection for accurate bulk air content estimation and the small specimen size would harm the final measurement results. In addition, the expense of using CT equipment is another issue in practical applications because of the high costs for acquiring and using the equipment (Aboufoul et al. 2019), and the fact that CT equipment is generally inaccessible in the field or near a field testing environment.

2.1.4 Deep Learning Based Approaches

Recent developments in artificial intelligence and computer vision play an important role in guiding scientific research. Deep learning based semantic segmentation, which is a subset of machine learning and aims to classifying an image at the pixel level, has achieved significant success in many image segmentation related fields, including autonomous driving (Cordts et al. 2016), pavement condition survey (Zhang et al. 2018), face recognition (Liu et al. 2017), and image search engines (Wan et al. 2014). The key advantage of deep learning based semantic segmentation techniques is the ability to learn appropriate feature representation of pixels in each category in an end-to-end manner. The deep learning techniques substantially improved the accuracy and efficiency of semantic segmentation tasks. However, despite the deep learning based semantic segmentation technique is highly relevant to the objective of concrete petrographic

analysis, the potential of this technique has not been widely studied.

R. Girshick et al. (Girshick et al. 2014) proposed a region-based convolutional neural network (RCNN). The method first utilized selective search (Uijlings et al. 2013) to extract numerous object regions, and then a set of features were extracted from each of the extracted regions. Finally, a classifier was utilized to classify regions into each category. Compared with conventional hand-crafted methods, the RCNN was able to address more complicated tasks and achieved a higher accuracy. A 30% improvement was found compared with the previous best model. However, the RCNN also suffers from many drawbacks for image segmentation tasks. Hariharan et al. (Hariharan et al. 2014) argued that the network RCNN was actually fine-tuned to classify bounding boxes, making it suboptimal to extract foreground features. Guo et al. (Guo et al. 2018) stated that the features extracted by RCNN did not contain sufficient spatial information, which leads to fuzzy boundaries in segmented images. Many improvements have been made to address these issues (Hariharan et al. 2014, Dai et al. 2015, He et al. 2015). Built over the successes of classification neural networks, Long et al. (Long et al. 2015) proposed the Fully Convolutional Network (FCN) which was the basis of many state-of-the-art deep learning based semantic segmentation methods. They replaced the fully connected layers of various CNNs like AlexNet (Krizhevsky et al. 2012), VGG (Simonyan and Zisserman 2014), GoogLeNet (Szegedy et al. 2015), and ResNet (He et al. 2016) with fully convolutional layers. The structure first realized end-to-end image semantic segmentation at the pixel level. While, the conventional FCN model did not consider the global context information, which inherently limited the spatial precision for semantic segmentation. Mostajabi et al. (Mostajabi et al. 2015) and Szegedy et al. (Szegedy et al. 2014)

illustrated the importance of adopting global context information for accurate image segmentation. As for semantic segmentation, per-pixel classification was often ambiguous in the presence of only local information. However, the task became much simpler if contextual information, from the whole image, was available. Chen et al. (Chen et al. 2014) introduced the idea of conditional random field (CRF) into FCN and proposed DeepLab. The CRF significantly refined object boundaries in the segmented image with an improved efficiency. Dilated convolutions (Zhou et al. 2015) expanded the receptive field of CNN by enlarge convolution filters without increasing parameters. The key advantage of dilated convolutions was improving the ability of global information integration without additional computation cost. The multi-scale context aggregation module (Yu and Koltun 2015), improved DeepLab (Chen et al. 2017), and the ENet (Paszke et al. 2016) all adopted dilated convolutions as a method to integrate global information. Feature fusion is another way to enlarge the receptive field of CNN. Liu et al. (Liu et al. 2015) proposed the ParseNet which concatenated global features with local features to form combined features. The combined features were then convoluted for classification. Chen et al (Chen et al. 2017) utilized Atrous Spatial Pyramid Pooling to combine the output of dilated convolutions with various dilation rates together to enlarge the field of view without increasing the number of parameters. U-Net, which is a variant of FCN, improved with skipped connections was proposed by Ronneberger et al. (Ronneberger et al. 2015). The U-Net consisted of an encoder and decoder. The skip connections combined low-level features with higher-level features, which improved pixel-level localization. The U-Net architecture has been validated to be powerful for binary image segmentation. It is currently one of the most used algorithms in biomedical

image segmentation (Chang and Liao 2019) and has been gradually extended to the other semantic segmentation tasks in many other fields (Lau et al. 2020, Shi et al. 2021). To make the U-Net architecture more suitable for the other tasks, Terausnet and Terausnetv2 networks first proposed a VGG combination of a pre-trained VGG network as the encoder of the U-Net. The proposed networks were powerful in satellite image segmentation (Iglovikov et al. 2018, Iglovikov and Shvets 2018). Wen et al. (Chang and Liao 2019) compared the encoder of U-Net with variants of VGG, ResNet18, DenseNet121, and variants of Inception for the segmentation of biomedical images. The VGG13 encoder U-Net outperformed the other architectures and deeper encoder architectures were not guaranteed to obtain better segmentation results. Buslaev et al. (Buslaev et al. 2018) utilized ResNet-34 as an encoder of conventional U-Net for satellite image segmentation and showed a good result. Tasar et al. (Tasar et al. 2019) considered the compromise between complexity and performance, and then adopted VGG16 as the encoder of the U-Net for segmenting large-scale remote sensing data. Even though the variants of U-Net with different encoder architectures were adopted in many research studies for various segmentation tasks. There were no generalized principles that could provide guidelines on architecture selection. Whether a modified architecture would improve segmentation results depends on the dataset size, image type (RGB, Depth, or greyscale), and segmentation objects.

2.2 Three-Dimension Reconstruction Methods - Photometric Stereo Method

As discussed previously, the air voids in the hardened concrete surface have similar greyscale values as the paste on concrete surfaces. A contrast-enhancement process is needed to make the air voids distinguishable from the solid phase. However, unlike the

solid phase which provides only color information, the air voids are hollows that embed in the hardened concrete surface. The 3D information (e.g. depth and gradient) is a valuable feature for air voids extraction and helps to distinguish the air voids from the solid phase. The utilization of 3D reconstruction methods is an effective way to obtain depth information within the air-void region. Generally, the state-of-the-art 3D reconstruction approaches can be classified as passive and active methods.

Passive 3D imaging approaches reconstruct the 3D surface of an object without introducing new energy (e.g. light) into the environment (Bianco et al. 2013). Numerous technologies and methods are employing this approach, including multi-view stereo (Pound et al. 2014, Pound et al. 2016), structure from motion (Jay et al. 2015), light-field (plenoptic) cameras (Bernotas et al. 2019), and space-carving techniques (Gibbs et al. 2018). Binocular stereo is the most common multiview stereo approach (Biskup et al. 2007, Burgess et al. 2017). Two cameras are utilized to capture pictures from slightly different two viewpoints. By analyzing the disparity between the objects in the two pictures, the relative depth can be calculated. However, calculating the disparity is not so straightforward for a computer. The correspondence problem is well known in the machine vision literature and refers to the difficulty in locating matching points in the two images. Wolter et al. (Wolter et al. 2019) made the first study on 3D air-void segmentation by using a photogrammetry method. The working principle of photogrammetry is similar to binocular stereo. The research investigated the potential of utilizing 3D reconstruction for air-void segmentation, but large differences were observed between the experiment results and the ground truth. An explanation could be the concrete surfaces were texture-less, which increased the difficulty of solving the

correspondence problem. Space-carving and light-field systems overcome the correspondence problem. However, space-carving systems require many different views and may fail to reconstruct the crowded areas (Bernotas et al. 2019). Light-field systems rely on expensive camera technology to capture high resolution data and thus make the air-void analysis system not cost-effective.

Active 3D imaging approaches introduce outside energy sources to help 3D reconstruction and overcome many problems of the passive approaches. The time-of-flight 3D laser scanner is an active scanner that uses laser light to probe the subject (Herrero-Huerta et al. 2018, Thapa et al. 2018). At the heart of this type of scanner is a time-of-flight laser rangefinder. The laser rangefinder finds the distance of a surface by timing the round-trip time of a pulse of light. The laser rangefinder only detects the distance of one point in its direction of view. Thus, the scanner scans its entire field of view one point at a time by changing the range finder's direction of view to scan different points. The advantage of time-of-flight range finders is that they are capable of operating over very long distances, about kilometers (Besl and McKay 1992). These scanners are thus suitable for scanning large structures like buildings or geographic features. The disadvantage of time-of-flight range finders is accuracy. Due to the high speed of light, timing the round-trip time is difficult and the accuracy of the distance measurement is relatively low, about millimeters. Triangulation is another active 3D imaging approach (Paulus et al. 2014). The triangulation laser shines a laser on the subject and exploits a camera to look for the location of the laser dots. Depending on how far away the laser strikes a surface, the laser dot appears at different places in the camera's field of view. The laser dot, the camera, and the laser emitter form a triangle, which makes the depth

measurement possible. Triangulation laser scanners are slow and susceptible to occlusions. Air-void regions may be obscured by air-void edges.

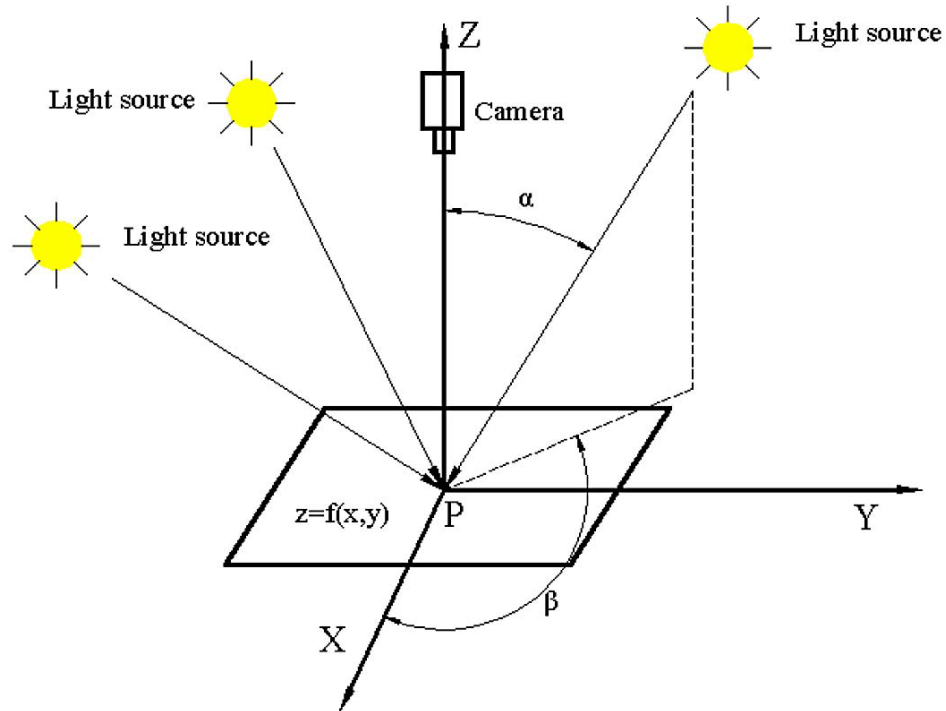


Figure 2. Schematic Diagram of Photometric Stereo (Sun and Wang 2017)

Photometric stereo is an active imaging technique that is low-cost and can achieve high image resolutions and fast capture speeds (Woodham 1980). The photometric stereo method, as shown in Figure 2, estimates the 3D surface of objects based on the relationship between image intensity and the surface normal under various lighting conditions. The photometric stereo method has the key advantage of achieving automation while reducing test time, which is a cost-effective and real access to high-resolution 3D images, easy to be implemented, and robust to be reconstructed on textured or texture-less surfaces.

2.3 Air-Void System Measurement Approaches

2.3.1 Conventional Approaches

The air-void system restores the ice formed under low temperatures and releases the pressure build-up induced by the freezing effect. Good freeze-thawing durability can be achieved through the presence of many small air voids distributed throughout the cement paste phase of the concrete (Snyder 1998). The spacing of air voids is of high importance to characterize the air-void system with the presumption that the concretes with different air-void spacings present different freeze-thawing performances.

Powers et al. (Powers and Willis 1950) characterized the air-void spacings. They hypothesized that freeze-thawing damages were caused by hydraulic pressure generated in the capillary pores during freezing which exceeded the tensile strength of the cement paste. The well-distributed air-void system provided extra spaces for the capillary pores to release hydraulic pressure and avoid damage. Power's theory is the most widely used and accepted method for measuring air-void spacing. However, Power's theory fails to provide a precise estimation of the actual spacing of air voids in concrete. It has been found that even the same sample processed following the ASTM C457 procedures gave out test results calculated by Power's spacing equation with considerable deviations (Simon 2005). Philleo et al. (Philleo 1983) refined Power's theory by quantifying the volume fraction of paste within the shell of an air void system. A Hertz distribution was adopted to approximate the paste-void proximity distribution for zero-radius points, and then this distribution was modified to account for finite-sized spheres by renormalizing the cumulative distribution to account for the air content. Attiogbe et al. (Attiogbe 1993) proposed a new spacing factor equation to calculate the mean air-void spacing voids by

taking geometric probability and stereological principles into consideration. The effects of large air voids for releasing the pressure build-up during the freeze-thawing cycles were considered in Attiogbe's equation. However, in the research conducted by Snyder (Snyder 1998), Attiogbe's equation did not accurately estimate the parameters of a simulated air void system. A possible explanation could be the indirectly measured air-void size distribution induced biases in the air-void parameter calculation. The actual air voids are spatially distributed in hardened concrete, while the aforementioned methods estimated the actual air-void size distribution from the information retrieved on a 1D level.

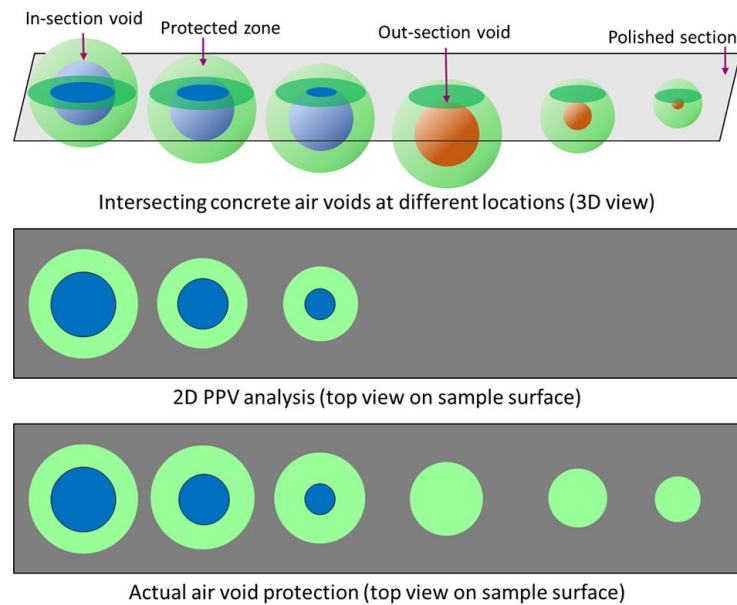


Figure 3. The Cross Profile of Air Voids in Polished Concrete Surface (Song et al. 2021)

As shown in Figure 3, the circles presented on the three-phase image cannot be treated as spheres in the paste and the 2D distribution is not proportional to that on a 3D level, since the sizes of circles in 2D do not follow the one-to-one correspondence with the sizes of spheres in 3D (Song et al. 2020a). And also, the effects of many out-section

air voids are neglected by a 2D air-void analysis. As the distance between the centroid and cross-section becomes even longer, the paste adjacent to the air void can be still protected by it, but there is no evidence indicating this kind of protection on a 2D surface. Therefore, knowing the information on 3D air-void distribution is critical to improving the reliability of the measurement results.

2.3.2 Stereological Approaches

Even though the techniques like CT scans can obtain the inner structure of hardened concrete precisely on a 3D level. The cost and availability of CT equipment can be a big hinder in practicals. The ASTM C457, which uses visual inspection to analyze the three phases of a hardened concrete surface, is still the most widely used and accepted method. However, linear-traverse method and modified point count method measure the air-void system in hardened concrete on a 1D level (linear-traverse method) or a 0D level (modified point count method). Considering the 2D nature of the hardened concrete surface, both linear-traverse method and modified point count method can be considered as sampling surveys and partial concrete surfaces are selected during the air-void measurement process. The utilization of ASTM C457 methods for air-void measurement is a trade-off between accuracy and cost.

Numerous studies have been done to characterize stereological air-void properties based on segmented 2D concrete images. The stereological analysis technic, which is a probabilistic approach to restore the 3D sizes of objects based on the statistical distribution of their 2D slices that appeared in an image, is the most commonly used approach for the analysis of air-void spatial distribution in hardened concrete. Murotani et al. (Murotani et al. 2019) proposed a simple method to estimate the air-void spacing

factor. The method assumed the air-void system as a mono-sized sphere system. The median distance and the characteristic distance, which were separately defined using the distance between the air-void centroids and the mean diameter of air voids, were proposed to measure the air-void system. The research found that the proposed parameters correlated well with the Power's spacing factor. However, during the freeze-thawing process, water was thought to move through the pore space in the cement paste to the surface of an air void, not to its centroid (Scherer and Valenza 2005). The distance between the air-void surfaces could better represent the capability of hardened concrete that releases the pressure during the freeze-thawing process whereby water escapes into empty air voids. To measure the distance between the air-void surfaces, the actual 3D size distribution of air voids should be estimated in advance.

Fonseca et al. (Fonseca and Scherer 2015) segmented the air voids in the contrast enhanced concrete surface by using Otsu's method which classified the grey value pixels by maximizing the intra-class grey value variance and minimized the inter-class grey value variance. An unfolding method – the Saltykov method, which estimated the 3D size distribution of air voids by using the size distribution of 2D profiles on a plane, was first applied for calculating the bulk volume of air voids inside the hardened concrete. The Saltykov method assumes that the center of 3D spheres is randomly distributed, and the 3D spheres are non-overlapping (Saltykov 1958). For a 3D sphere of radius R , the probability of its 2D intersections $P(r)$ with a radius of r follows Equation (1).

$$P(r) = \frac{r}{R\sqrt{R^2 - r^2}} \quad (1)$$

The 2D air-void size was first classified into several classes with a fixed class width.

And then, the radius of the largest 2D intersection was used as the radius of the largest 3D air void. The number of 3D air voids from each 2D air-void class was inversely calculated according to Equation (1). Mostly, concrete void size distribution follows a lognormal trend (Yun et al. 2012, Fonseca and Scherer 2015). The fixed class width could lead to the number of observations of profiles in some classes being lower than the expected value, and furtherly caused a negative number of spheres to be estimated from those classes. A large class width was utilized to solve this problem, which reduced the accuracy of the 2D-to-3D unfolding process. Mayerisk et al. (Mayercsik et al. 2014) introduced a two-step approach to measure the air-void parameters based on the estimated 3D air-void distribution. The first step estimated the 3D air voids distribution by extracting the line segment length probability and the chord length probability from the 2D air-void intersections. By deriving these two distribution functions, the volume fraction of air voids, the number density of air voids, and the first three moments of the size distribution were obtained and utilized to evaluate the 3D air-void system inside hardened concrete. And then, in the second step, a nearest-surface distribution function, which was first derived by Lu and Torquato (Lu and Torquato 1992), was utilized to estimate the spatial arrangement between any point in the cement paste and its proximity to the surface of a nearby air void. The reciprocal value of the 95% percentile of the nearest-surface distribution function was used to approximate the spacing factor. The Protected Paste Volume (PPV) method which was originally proposed by Larson et al. (Larson et al. 1967) has been utilized for estimating free-thaw performance using 2D concrete images (Peterson et al. 2001a, Wawrzeńczyk and Kozak 2016). The PPV method assumed that the paste within a certain distance from the air-void surface was

protected from freeze-thawing damages. Song et al. stated that the PPV method is more reliable and understandable than Power's approach (Song et al. 2020a). In the research by Song et al., the PPV method was introduced for air-void analysis from a 3D perspective. The Saltykov method, which has been adopted in Fonseca et al.'s (Fonseca and Scherer 2015) research, was utilized for back-calculation of 3D air-void distribution. The unfolding results were evaluated by the protect region which was approximated using the Powers' spacing factor. The Powers' spacing factor measures the maximum distance from a point in the paste to the adjacent air void. The research report that around 98% of the pastes were protected by the estimated 3D air-void system. The result was aligned with the research findings in Yun et al.'s research (Yun et al. 2012). In another research conducted by Song et al. (Song et al. 2021), the factors that influence the 3D unfolding method were investigated. The research results showed that the unfolding accuracy was significantly affected by air-void class numbers. Increasing the number of air-void classes increased the unfolding accuracy, while reducing the number of air voids in each class. The logarithmic binning strategy, which optimizes the class count and the class size, was introduced to classify the air voids into different classes. The logarithmic binning strategy maximized the class number for the small air voids and increased the number of air voids in large air-void classes. The unfolding method which adopted the logarithmic binning strategy back-calculated the 3D air-void distribution with less bias and improved smoothness. The logarithmic binning strategy effectively improves the unfolding method used by Fonseca et al. (Fonseca and Scherer 2015). However, no study has precisely analyzed the reliability of using the Saltykov method to estimate the 3D air-void distribution. Most of the studies acknowledged the reliability of Power's method due to

its aggressive assumptions and unreliable measurement results, nevertheless, they still use air-void parameters measured by Power's method as ground truth to evaluate the 3D air-void distribution estimated using the Saltykov method. Consequently, the reliability of the Saltykov method need to be evaluated in a more intuitive way.

2.4 Summary

In this chapter, the related research studies for 3D reconstruction methods, image segmentation methods, and stereological analysis methods were discussed. Based on the literature review, the findings can be summarized below:

(1). The low contrast between the air voids and cement paste makes the distinguishment of air voids in hardened concrete surfaces using computer-aided image processing methods a challenging work. The air voids in the hardened concrete surface have similar pixel intensities to the cement paste. The contrast enhancement-based method normally takes 3~4 hours for one concrete sample to be contrasted. The profile and depth information of air voids can be effectively used as a feature to distinguish the air voids from the background. Consequently, a 3D reconstruction method is required to capture those features. Compared with various conventional 3D reconstruction methods, the photometric stereo method can be considered a qualified 3D reconstruction method for 3D concrete surface reconstruction.

(2). According to ASTM C457 standard, the automated measurement of the air-void parameters needs to be conducted on a segmented concrete surface image in which the air voids and hardened concrete surfaces need to be differentiated. The image segmentation method classifies each image pixel into different classes. Many conventional image

processing methods have been conducted on contrast-enhanced concrete surface images to segment the air voids. The color and shape variances of the air voids are important features that can be utilized to segment the air voids. The advantages of the conventional image processing methods are simple and easy to apply. The disadvantages of the conventional image processing methods are objective and inaccurate.

(3). Deep convolution neural networks (DCNN), which are subareas of deep learning, present significantly higher robustness and generalizability compared with conventional image processing methods. However, very limited research adopted DCNN for air-void segmentation, and there is a lack of experience with air-void segmentation using DCNN. Considering the advance of DCNN, it is necessary to investigate the feasibility of using DCNN to segment the air voids in hardened concrete surfaces.

(4). The reliability of the Power's spacing factor has been debated in many research studies. A lot of attention has been paid to proposing a new evaluation index for the freeze-thawing performance of hardened concrete. The protected Paste Volume (PPV) method has been proved as a new way to characterize the freeze-thaw performance of hardened concrete. The necessity of 3D air-void distribution has been demonstrated for PPV methods. As a stereological method, the Saltykov method has been used to estimate the actual 3D air-void distribution. However, no study has precisely analyzed the reliability of using the Saltykov method to estimate the 3D air-void distribution. Most of the studies acknowledged the reliability of Power's method due to its aggressive assumptions and unreliable measurement results, nevertheless, they still use air-void parameters measured by Power's method as ground truth to evaluate the 3D air-void distribution estimated using the Saltykov method. The reliability of the Saltykov method

needs to be evaluated in a more intuitive way.

3. METHODOLOGY

In this chapter, the details of 3D reconstruction methods, image segmentation methods, and stereological analysis methods used in this research are described.

3.1 Concrete Surface Normal Reconstruction Methods

As discussed in section ‘Literature Review’, the low contrast between the air voids and cement paste challenges the air-void measurement using computer-aided image processing methods. One of the explanations is that the low contrast makes edge detection using image processing methods become impossible. Considering the 3D nature of the air voids inside hardened concrete surfaces, it is worth to adopt the 3D information of air voids and make the air voids distinguishable from the cement paste. Therefore, in this research study, 3D reconstruction methods were utilized to obtain the 3D information of the air voids as well as the concrete surfaces. The captured 3D information would be useful for air-void segmentation.

The photometric stereo method estimates the 3D surface of objects based on the relationship between image intensity and the surface normal under various lighting conditions. A diagram for the photometric stereo method is shown in Figure 2. Compared to conventional air-void detection methods, the photometric stereo method has the key advantage of achieving automation while reducing test time, which is a cost-effective and real access to high-resolution 3D images, easy to be implemented, and robust to be reconstructed on textured or texture-less surfaces. Shadow and specularities are two kinds of surface corruptions that can be observed on concrete surfaces under various lighting directions. It is important to properly address these surface corruptions during

photometric stereo procedures.

3.1.1 Photometric Stereo

The photometric stereo methods were originally designed for Lambertian surfaces. The Lambertian surfaces are ideal smooth and diffusely reflecting surfaces. The apparent brightness of a Lambertian surface to an observer is the same regardless of the observer's angle of view. However, the polished hardened concrete surfaces cannot be considered as ideal diffusely reflecting surfaces. Specularities can be observed under specific observation angles. Also, the air voids inside hardened concrete surfaces generate the unevenness, which cause the hardened concrete surfaces cannot be considered as ideal smooth surfaces as well. Consequently, it is important to investigate different photometric stereo methods and to understand the impact of the corruptions to 3D reconstruction results.

3.1.1.1 Lambertian Surfaces

Woodham (Woodham 1980) first proposed the photometric stereo method by assuming an ideal Lambertian surface. The surface normal (vector or matrix) at each pixel can be calculated when the number of illuminations $k \in \mathcal{R}$ is over three. The photometric stereo method estimates the surface normal by calculating the relationship between incoming lighting direction $L \in \mathcal{R}^{k \times 3}$, surface normal $N \in \mathcal{R}^{3 \times 1}$, and observed intensity $I \in \mathcal{R}^{k \times 1}$ through Equation (2).

$$\begin{bmatrix} i_1 \\ i_2 \\ \vdots \\ i_k \end{bmatrix} = \begin{bmatrix} L_1 \\ L_2 \\ \vdots \\ L_k \end{bmatrix} \cdot \begin{bmatrix} n_x \\ n_y \\ n_z \end{bmatrix} \quad (2)$$

For the 3D reconstruction of an ideal Lambertian surface, Equation (2) can be used to compute the surface normals as the Least Squares solution to a set of linear equations that relate the observations and known lighting directions. Such Least Squares solutions are accurate if only small magnitude of Gaussian noise exists. However, Polished concrete surface cannot be considered as an ideal smooth Lambertian surface, because attached shadow and specularities are likely to be observed on the polished concrete surface. Both of the two corruption effects are considered non-Lambertian. Several studies were conducted to make the photometric stereo method more robust to the non-Lambertian effects. Specular reflections and shadowing effects can both be commonly observed from polished hardened concrete surfaces, which can affect the accuracy of Least Squares solutions and result in incorrect estimates of surface normal.

3.1.1.2 Non-Lambertian Surfaces

(1) Low-rank Minimization Method

Bidirectional Reflectance Distribution Function (BRDF) which encodes the diverse appearances of real-world objects is utilized to relate the observed intensity I to the associated surface normal N , the incoming lighting direction L , and viewing direction V . Shafer (Shafer 1985) stated that the observed intensity I at a given point from a smooth real-world object is a linear combination of diffuse and specular reflectance as shown in Equation (3).

$$I = f_d(N, L) + f_s(N, L, V) \quad (3)$$

Some of the photometric stereo methods consider the non-Lambertian effects as outliers. Tang et al. (Tang et al. 2005) introduced two coupled Markov Random Fields

(MRFs) to model the photometric stereo problem and a tensorial belief propagation method was utilized to approximate the solution of the Markov network. The research results of the study showed that the MRFs method tended to over-smooth the surface normal map. Miyazaki et al. (Miyazaki et al. 2010) proposed a median-filter based method and the outliers were refined by the median estimate of neighboring pixels. Wu et al. (Wu et al. 2010) proposed a Low-rank minimization method which performed well in several research studies. The observations were first decomposed into a low-rank Lambertian structure $I_A \in \mathcal{R}^k$ and sparse non-Lambertian outliers $E \in \mathcal{R}^k$ as shown in Equation (4).

$$I = I_A + E \quad (4)$$

Consequently, the Low-rank minimization method which is shown in Equation (5) was utilized to solve the normal vector of the observed surface.

$$\min_{I_A, E} \|E\|_F \quad s. t. Rank(I_A) \leq r, I = I_A + E \quad (5)$$

where $\|E\|_F$ is Frobenius norm of matrix E .

Several algorithms have been developed to solve the low-rank matrix approximation problem, for example, iteration threshold algorithm, accelerated proximal gradient algorithm, dual algorithm, and augmented Lagrange multiplier (ALM) algorithm are commonly used algorithms for solving the low-rank matrix approximation problem. In a comparison study by Shi et al. (Shi et al. 2013), the ALM algorithm outperforms the other algorithms with faster computation speed and lower computation cost. Consequently, the ALM algorithm was selected in this study to solve the low-rank matrix approximation problem.

(2) Sparse Bayesian Regression method

Even though the Low-rank minimization method that considers non-Lambertian observations as outliers could improve the result to some extent, it may also discard useful information in the non-Lambertian region. In order to retain the information, some methods incorporate the non-Lambertian effects E like shadows, specularity and inter-reflections into the BRDF model.

$$I = f_d(N, L) + f_s(N, L, V) + E \quad (6)$$

The Sparse Bayesian Regression method (SBL) is one of the robust photometric stereo models that is commonly utilized to solve the surface normal in Equation (6) (Ikehata et al. 2012). In this method, a piecewise linear function was first introduced to approximate the BRDF model which is shown in Equation (7).

$$N^T l_j = \sum_{h=1}^p a_h g_h(i_j) + e_j \quad (7)$$

where a_h are unknown parameters; p is the number of inverse functions used; $g_h(i_j)$ is an inverse function $N^T l_j = g_h(i_j)$ which is represented by a piecewise linear function which is shown in Equation (8).

$$g_h(i_j) = \begin{cases} 0, & (0 < i_j < b_{h-1}) \\ i_j - b_{h-1}, & (b_{h-1} \leq i_j < b_h) \\ b_h - b_{h-1}, & (i_j \geq b_h) \end{cases} \quad (8)$$

where b_h is the point where the h^{th} linear segment ends and the $(h+1)^{\text{th}}$ segment begins.

The illustration of the piecewise linear function is showed in Figure 4. As shown in Figure 4, each basis function can be defined as a polylinear function which has a breaking

point, and the piecewise linear function is defined as the summation of these basis functions.

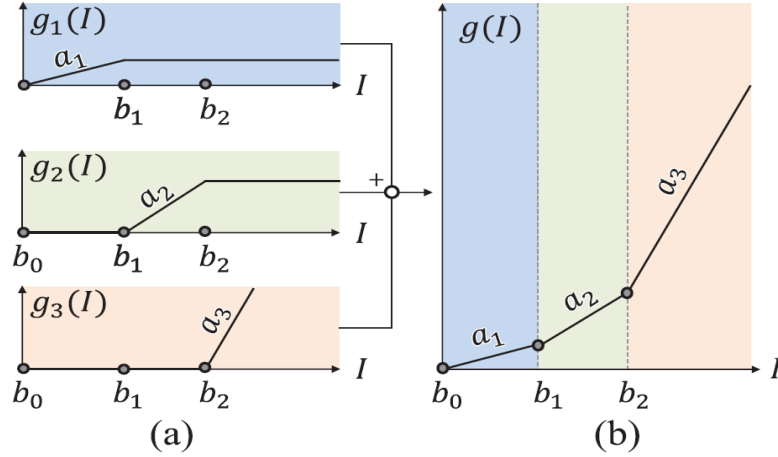


Figure 4. The illustration of the piecewise linear function (Ikehata et al. 2012)

Assuming k illumination directions are observed for one object, then Equation (6) can be represented by matrix manipulation and transferred into a linear problem.

$$AD + E = 0 \quad (9)$$

where D is an unknown parameter vector and $D = [n_x, n_y, n_z, a_1, \dots, a_{p-1}, a_p]^T$; A is a matrix with known experiment parameters $A = [A_1, A_2, \dots, A_j, \dots, A_k]$ where $A_j = [-l_x^j, -l_y^j, -l_z^j, b_1 - b_0, \dots, b_{h-1} - b_{h-2}, i_j - b_{h-1}, 0, \dots, 0]$; E is an unknown non-Lambertian vector and $E = [e_1, e_2, \dots, e_k]^T$.

Equation (8) is not a constrained problem because the number of independent functions k is always smaller than the number of unknowns $(3+p+k)$ (vectors D and E). Finally, the SBL is utilized to estimate the unknown parameter vectors D and E of Equation (9) by applying an independent, zero-mean Gaussian prior distributions on both

D and *E* (Tipping 2001).

The computation of surface normal is the fundamental step to get accurate concrete surface profile information. Considering the polished concrete surface is not an ideal Lambertian surface, the performance of the basic photometric stereo method, the Low-rank minimization method, and the SBL method should be evaluated before surface normal integration and air-void segmentation.

3.2 Air-Void Segmentation Approaches

In this research, both conventional image processing methods and deep learning based image processing methods were introduced for air-void segmentation. The segmented air-void images can be used for air-void parameter measurements.

3.2.1 Conventional Segmentation Methods

Two different air-void segmentation approaches were proposed in this study to extract air voids from the 3D concrete surface profile. One approach directly extracted air voids from the normal map. A threshold of the slant angle of surface normal was calculated to distinguish the air voids region from the concrete surface. The other approach first reconstructed the 3D surface of the concrete specimens using surface integration which is the sequential step after the surface normal reconstruction step as shown in Figure 5. Then, the air voids were segmented using a regressed surface plane from the reconstructed 3D surface. The details of these two approaches are described in 3.2.1.1 ‘Normal Map Method’ and 3.2.1.2 ‘Surface Plane Method’ sub-sections. A flow chart is shown in Figure 5 to give an overview of the computation process.

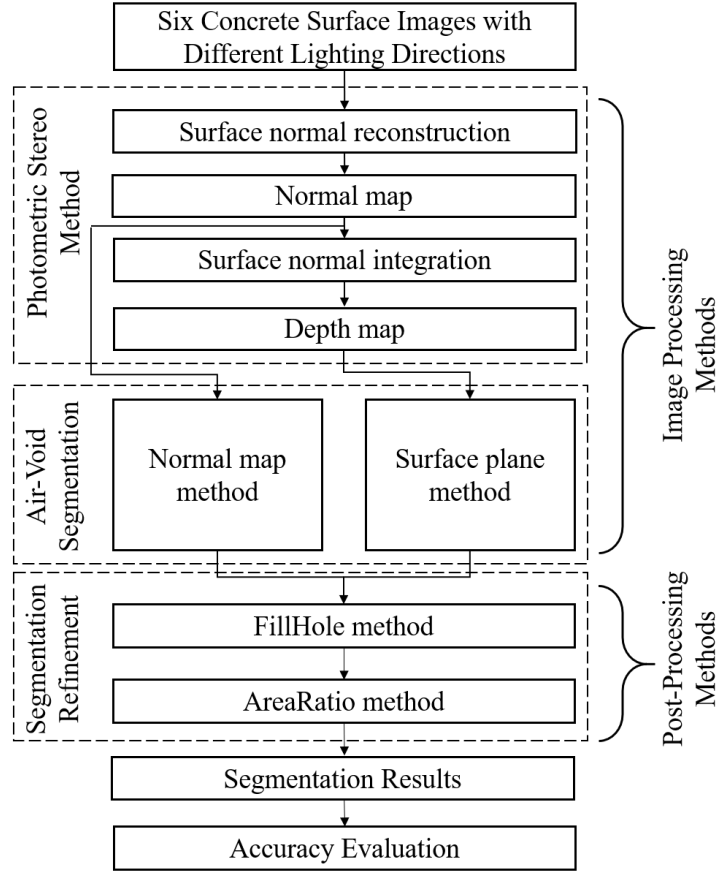


Figure 5. Flow chart of 3D air voids segmentation

3.2.1.1 Normal Map Approach

The normal map approach uses the generated concrete surface normal map to segment the air voids. For each pixel in the normal map, the surface gradient is represented by a surface normal vector, N_i . The normal vector of concrete surface plane is denoted as N_{xoy} , or the Z axis.

$$N_{xoy} = [0, 0, 1] \quad (10)$$

Then, the surface angle θ can be calculated by Equation (11).

$$\theta = \arccos \left(\frac{N_t \cdot N_{xoy}}{|N_t| |N_{xoy}|} \right) \quad (11)$$

The normal map method assumes that the air voids have a sharper surface gradient and the concrete surface has a flatter surface gradient. Therefore, the pixels in the normal map that have a small θ could be concrete surface and the pixels in the normal map that have a large θ could be air voids. The relationship between N_t , N_{xoy} and θ is shown in Figure 6.

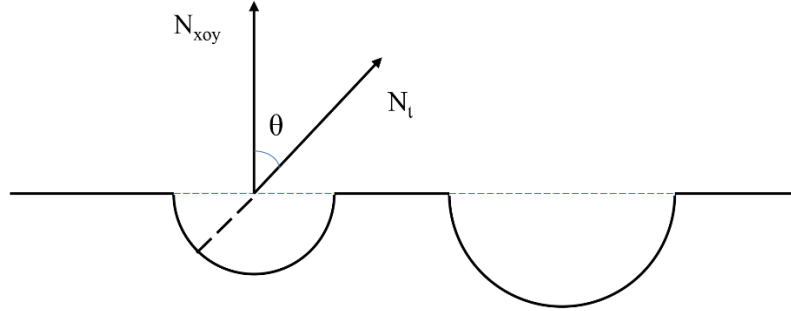


Figure 6. N_t , N_{xoy} and θ on concrete surface

3.2.1.2 Surface Plane Approach

The surface plane method uses the generated concrete surface depth map to estimate the structure of air voids. A surface plane equation which is shown in Equation (12) is regressed using the least square method where a , b , c , and d are regression coefficients.

$$ax + by + cz + d = 0 \quad (12)$$

The surface plane method assumes the integrated concrete surface as a flat plane. A bent/slant concrete surface can lead to inaccurate segmentation results by using the

surface plane method. A 2D Gaussian filter can rectify the surface profile. The generic 1D Gaussian filter can be expressed as:

$$\text{Gaussian}(\psi) = \frac{1}{\sqrt{2\pi}\sigma} e^{-(\psi-\mu)^2/2\sigma^2} \quad (13)$$

where ψ is an independent random variable; σ^2 and μ are the variance and mean of the distribution; π and e are constant values.

3.2.1.3 Segmentation Refinement

A set of image processing procedures were designed and utilized to remove the errors in air-void segmentation results. 1) A FillHole method was introduced to eliminate the false negatives at the bottom of air voids. The FillHole method identified and filled up the internal contour of each segmented shape. 2) An AreaRatio method was furtherly introduced to eliminate the false positives caused by dark or transparent aggregates based on the segmentation results refined by the FillHole method. The AreaRatio method can be considered as a kind of active contour line based method. Different from most of the segmentation methods such as global thresholding, spectral analysis, and random fields, the active contour line based method could segment the region of interest based on shape information. In a research conducted by Lu et al. (Lu et al. 2017), the concrete specimen was scanned by X-ray CT and the active contour line based method was used to differentiate the voids in cement paste and aggregates. In another study, the active contour line based method was used to differentiate the void space and solid phase in X-ray CT scanned concrete images (Lu et al. 2018). Few applications of the active contour line based method were reported for concrete air-void segmentation, but its effectiveness of differentiating the objects with various shapes was revealed. In this research, the

AreaRatio method assumed that most of the aggregates have an irregular shape and most of the air voids have a round shape. The AreaRatio method first identified the external contour of each segmented shape and an enclosing circle was generated for each external contour. The area ratio for each segmented contour was calculated by Equation (14). In this way, a perfectly round shape could have an area ratio approximate to 1, while an extremely irregular shape could have an area ratio much less than 1.

$$area\ ratio = \frac{the\ area\ of\ segmented\ shape}{the\ area\ of\ coresponding\ enclosing\ circle} \quad (14)$$

3.2.3 Convolution Neural Networks

As a subarea in artificial intelligence (AI), deep learning (DL) has achieved great success in semantic segmentation. During the semantic segmentation process, a classification label is predicted on each pixel, which may greatly fulfill the objectives of air-void segmentation. The deep convolutional neural networks (DCNN), which is an important branch in DL, show good potential in detecting target objects in noisy images at pixel resolution.

U-Net, which is a variant of Fully Connected Networks (FCN) and improved with skipped connections, was adopted for air-void segmentation in this study (Ronneberger et al. 2015). As shown in Figure 7, the U-Net consists of an encoder structure and a decoder structure. Skip connections between the encoder and decoder combine lower-level features with higher-level features. The combined features can improve pixel-level localization. The U-Net architecture has been validated to be powerful for image segmentation. It is currently one of the most used algorithms in biomedical image

segmentation (Chang and Liao 2019) and has been successfully extended to the other semantic segmentation tasks in many other fields (Lau et al. 2020). In addition, the U-Net model can generate a comparable result using a small dataset. In the study, the algorithm was coded and implemented with TensorFlow, an open-source deep learning library in Python. The training processes were conducted on the Google Colab Pro which provides Graphics Processing Units (GPUs) for deep learning purposes and one NVIDIA® Tesla® V100 GPU with 16GB of RAM. A flow chart that includes the major works of training the U-Net model is shown in Figure 8.

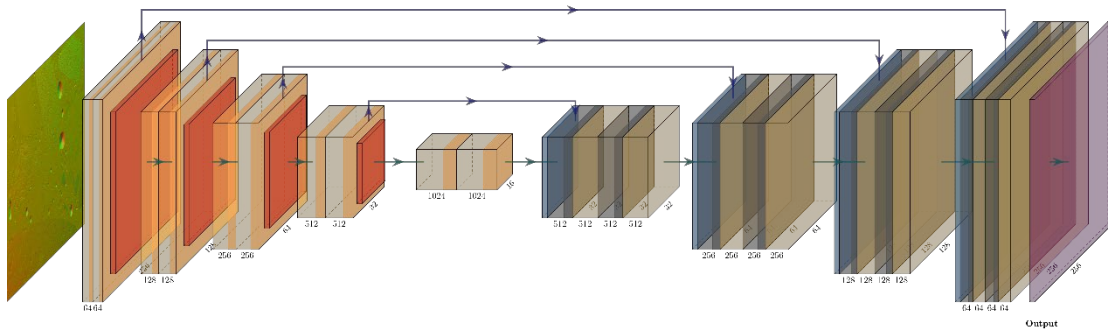


Figure 7. U-Net for image with resolution of 256 pixels \times 256 pixels

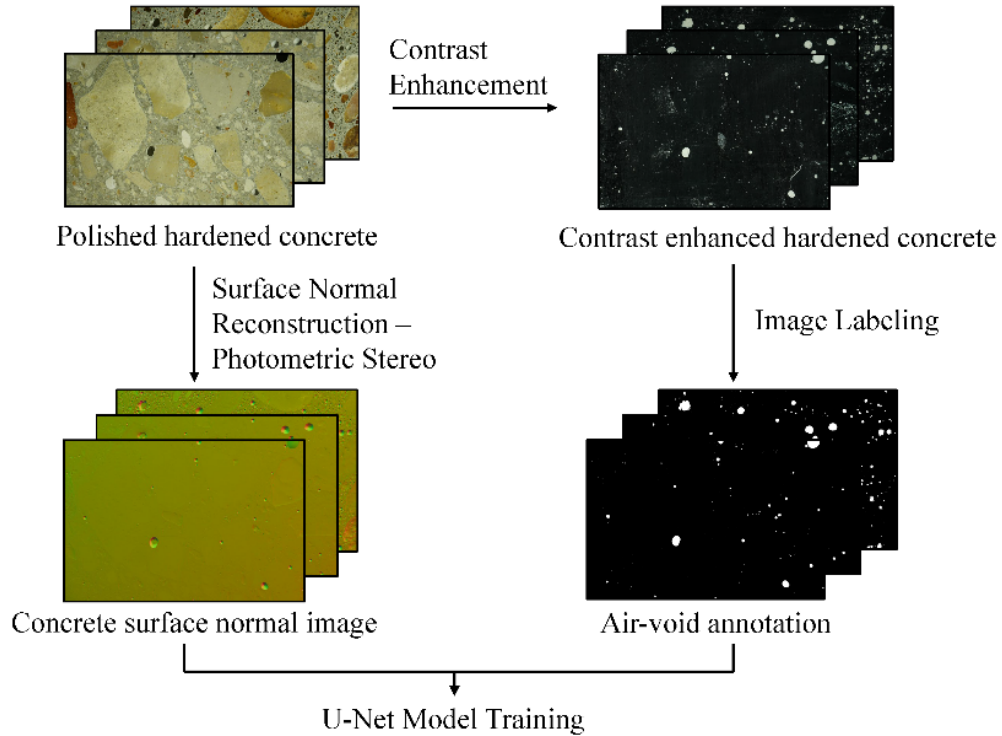


Figure 8. Steps of U-Net model training. The concrete surface normal images and air-void annotations were utilized for the training process.

There are 1,941,105 trainable parameters incorporated in the U-Net model. During the training process, cross-entropy was selected as the loss factor to evaluate the discrepancy between the training results and labels after each epoch. The Adam optimizer was adopted for updating the weights in U-Net.

3.3 Stereological Analysis – the Saltykov Method

The air-void segmentations generated using the method described above provide a feasible way for the measurement of air-void parameters based on the ASTM C457 standard. As a potential successors for Power’s method, the protected Paste Volume (PPV) method has been proved as a new way to characterize the freeze-thaw performance of hardened concrete. One limitation of the up-to-date PPV analysis is that it only

experiment with a single 2D surface plane of a polished concrete specimen, which can be restricted by the limited information that can be provided by 2D analysis. 3D air-void distribution is necessary for improving the reliability of the PPV analysis.

3.3.1 Estimation of In-Section Air Voids

The Saltykov method provides a feasible way to estimate the 3D air-void radius distribution using the information of 2D air-void intersections. For an IUR (isotropic, uniform, and random) mono-sized sphere system with sphere radii equal to R , the radius r of the sphere sections intersected by any cutting plane should follow a distribution. Russ et al. inferred the mathematical relationship between the sphere and its 2D intersections (Russ and Dehoff 2012). For a 3D sphere with radius R , the probability of its 2D intersections $P(r)$ with a radius of r follows Equation (15).

$$P(r) = \frac{r}{R\sqrt{R^2 - r^2}} \quad (15)$$

For a given 3D sphere with radius R , the probability of its 2D intersection with a radius between 0 and r can be calculated using Equation (15). In most cases, the characteristics of probability density functions are more meaningful and identifiable than cumulative density functions. Consequently, the probability density function of Equation (15) is presented in Equation (16). By using Equation (16), the probability of the air-void intersections within a specific radius range can be integrated.

$$P(r_i < r < r_{i+1}) = \frac{N_{Ri}}{N_R} = \frac{\sqrt{R^2 - r_i^2} - \sqrt{R^2 - r_{i+1}^2}}{R} \quad (16)$$

where r_i and r_{i+1} are the radius range of the intersected sphere sections, i indicates the

class sequence number of the prescribed radius range $i \in (1, 2, \dots, j)$, j is the number of total bin classes, N_{Ri} is the number of 3D voids with radius R involved with the intersected voids with radius between r_i and r_{i+1} , N_R is the total number of 3D voids with radius R , and P is the probability of the radius of a random intersection from a sphere with radius R in the interval from r_i to r_{i+1} .

For a set of void intersections generated from an idealized system with mono-sized air voids, the distribution of the radius of the void intersections can be obtained. By using the distribution of the void intersection radius and Equation (16), the 3D actual void size can be unfolded. As mentioned before, the actual air-void system in hardened concrete is a multi-sized void system. A basic concept for unfolding a multi-sized void system is assuming that the multi-sized void system is a superposition of multiple mono-sized distributions. Consequently, the following procedures were designed and programmed to unfold the actual 3D void distribution based on the distribution of the 2D void intersection radius.

(1). The consecutive distribution of the 2D void intersection radius is transferred into a discrete distribution using a histogram transformation. The total number of bin classes j needs to be predefined before the transformation. In the transferred discrete distribution, the boundary (r_i and r_{i+1}) and the number of 2D void intersections n_{ri} of each bin class are recorded for continuous analysis purposes.

(2). The upper boundary of each bin class is considered as the approximated 3D void radius. The upper boundary of the largest 2D void intersection bin class is considered as the approximated radius for the largest 3D void bin class R_j . All the 2D void intersections in the largest 2D void intersection bin are assumed to be yielded from the largest-sized

3D voids near their centroids.

(3). The unfolding process is started with the bin class with the largest 2D void intersection radius. With approximated radius and count of the largest 3D void bin known, Equation (16) can be used to determine the total number of voids in the largest 3D void bin class.

(4). According to the calculated number of voids in the largest 3D void bin, the number of the 2D void intersections generated by the largest 3D voids in each smaller bin can be calculated $(N_{R_{jj-1}}, N_{R_{jj-2}}, N_{R_{jj-3}}, \dots, N_{R_{j1}})$.

(5). By subtracting the count of observed 2D void intersections $(n_{rj-1}, n_{rj-2}, n_{rj-3}, \dots, n_{r1})$ with the count of unfolded 2D void intersections cut from the largest 3D voids $(N_{R_{jj-1}}, N_{R_{jj-2}}, N_{R_{jj-3}}, \dots, N_{R_{j1}})$, a new distribution of the 2D void intersections is generated. The second-largest bin now becomes the largest in the resultant histogram and its actual count can be analyzed using the above-stated steps (steps 2-4).

(6). Iterating steps 2-4 down to the smallest bin class, until a final determination of actual void size distribution is achieved.

As mentioned in many previous studies, one known problem of using the Saltykov method for 3D air void unfolding is the negative value calculated from smaller bins (Fonseca and Scherer 2015, Lopez-Sanchez and Llana-Fúnez 2016). In this study, if negative values appear, they will be replaced with zero. To simulate the air-void intersections in hardened concrete surface, the synthetic air-void model will be sliced by a virtual plane. The information of any 3D air voids in the synthetic model that intersected with the plane will be recorded. Same as the radius and coordinate of the 2D

air-void intersections.

3.3.2 Estimation of Out-Section Air Voids

The out-section air voids cannot be observed through the 2D air-void intersections in concrete surfaces, but it has a significant protective effect on the concrete paste. In the research by Song et al., the relationship between the number of in-section air voids and the number of out-section air voids was inferred using Equation (16) (Song et al. 2020a). For a given protection range p , the larger radius associated with the out-section void ($R + p$) should be considered in the calculation. Consequently, when a section cuts right on the air void boundary, the radius of the out-section protection t is maximized:

$$t_{max} = \sqrt{(R + p)^2 - R^2} \quad (17)$$

Therefore, the probability of getting an intersection with the radius between 0 and t_{max} from an out-section air void with the radius of $R + p$ can be presented as:

$$P_{out}(0 < r < t_{max}) = \frac{\sqrt{(R + p)^2 - 0} - \sqrt{(R + p)^2 - t_{max}^2}}{R + p} = \frac{p}{R + p} \quad (18)$$

while the probability for an in-section air void is:

$$P_{in}(t_{max} < r < R + p) = \frac{\sqrt{(R + p)^2 - t_{max}^2} - \sqrt{(R + p)^2 - (R + p)^2}}{R + p} \quad (19)$$

$$= \frac{R}{R + p}$$

The ratio of in-section and out-section air voids can be estimated using Equation (20).

$$\alpha_{in/out} = \frac{R}{p} \quad (20)$$

Consequently, the out-section air voids can be calculated according to the count of in-section air voids in each bin using Equation (20).

4. AUTOMATED IMAGE SEGMENTATION OF AIR VOIDS IN HARDENED CONCRETE USING PHOTOMETRIC STEREO THREE-DIMENSIONAL RECONSTRUCTION METHOD

One of the biggest hinders to segment the air voids in hardened concrete surfaces is the low contrast between the air voids and cement paste. Considering the three-dimensional (3D) nature of the air voids, it is reasonable to adopt the profile information of air voids for air-void segmentation. The photometric stereo method, one major component of vision-based 3D techniques, which has been effectively used in reverse engineering, industrial testing, and archaeology due to its advantages of simple operation, high resolution, and low cost could be utilized to capture the 3D information of air voids in a hardened concrete surface. The objective of this chapter is twofold. One is to investigate the feasibility of using the photometric stereo method to contrast the air voids in hardened concrete surfaces. The other one is to propose a method to segment the air voids using the captured 3D information without the use of contrast enhancement. The segmentation of paste and aggregates is not included in the scope of this research.

In this chapter, a photometric stereo system with one Charge-coupled Device (CCD) camera and six light-emitting diodes (LED) lights was first set up and used to capture concrete surface images under different lighting conditions. Then, the performance of one basic photometric stereo model and two robust photometric stereo models was evaluated. Consequently, two air-void interpretation approaches were introduced for the air-void segmentation. Finally, a set of post-processing procedures were conducted to refine the air-void segmentation results.

4.1 Data Acquisition and Description

4.1.1 Instrument Setup

Conventional photometric stereo systems use three LED lights to reconstruct 3D information of an object. A recent study reported that the photometric stereo system with more LED lights could improve the reconstruction accuracy (Quéau et al. 2017). In our study, a photometric stereo system with six LED lights (as shown in Figure 9) was assembled to capture concrete surface images under different lighting conditions.

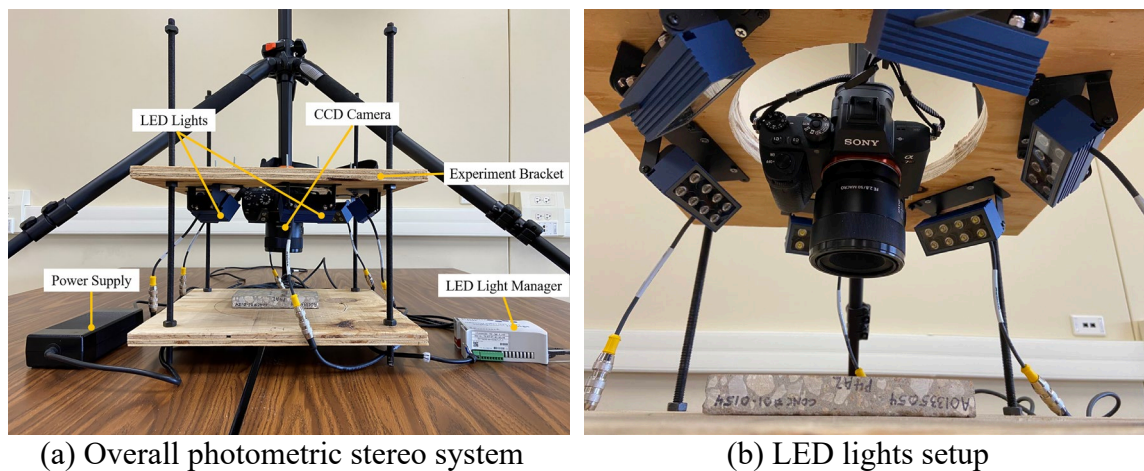


Figure 9. Six LED light photometric stereo system

The Sony α 7R II camera with a fixed-focus lens was used to capture the images of concrete specimens. The camera was located above the specimen and fixed by a tripod. The pixel resolution which is the actual distance on a sample surface mapped by one pixel is a key parameter for the camera system. The maximum magnification ratio represents the maximum ratio of the Complementary Metal Oxide Semiconductor (CMOS) sensor size and the captured object size. Both CMOS sensor size and the maximum magnification ratio decide the size of the smallest air voids that can be captured by the camera. In this research, if the maximum magnification ratio is 1, the

minimum focus distance would be 16 cm, and the size of the CMOS sensor would be 3.58 cm × 2.38 cm. When the distance between the camera and the specimen surface is set to 16 cm, the smallest concrete surface area of size 3.58 cm × 2.38 cm exposed to the CMOS sensor would be captured. Under this situation, the pixel resolution could achieve 4.5 μm/pixel. The specifications for both the camera and the lenses are listed in Table 1.

The six LED lights are from Smart Vision Lights Inc. and the model used was LM75. For the LED lights, both the uniformity of illumination and the size of the illumination region are two important parameters. The LED light equipped with an 80° wide angle lens which could generate an approximately 16 cm × 16 cm uniform illumination at a working distance of 16 cm could provide a wide-angle uniform light projection, and could simulate the parallel light emitted from a point light source at an infinite distance. The six LED lights were fixed in a 16 cm diameter circle with equal spacing from each other and the tilt angle of each LED light was 45° which is shown in Figure 9(b). The LED light manager was used to control the six LED lights in turn and a total of six concrete surface images were captured for each concrete sub-specimen. The power supply which could provide a maximum of 24 V and 17 A output was selected as power input for the photometric stereo system. The size of the experiment bracket was 40 cm × 40 cm × 20 cm. To minimize the uncertain disturbance caused by ambient light, the whole system was covered by shade cloth when in use.

Table 1. Technical Specifications of Sony α 7R II CCD Camera and Sony FE 50 mm F2.8 Macro Lenses

	Technical specifications	Value
Camera	Resolution	42.2 megapixel
	CMOS sensor	35.9 mm * 24.0 mm
	Pixel size	5.66 μ m
Lenses	Focal length	20 cm
	Smallest focus distance	16 cm
	Maximum magnification ratio	1
	Aperture	f/2.8
	Shutter time	1/16
	ISO	100

4.1.2 Hardened Concrete Samples

Three polished concrete specimens used in this study were provided by a concrete laboratory of the Texas Department of Transportation (TxDOT). All these three concrete specimens were drilled and sampled from an in-service concrete pavement. The size of the concrete specimens is approximately 15 cm \times 8 cm. The concrete specimens were carefully polished according to the guidance in ASTM C457 (ASTM 2012). In order to capture the smallest air voids in the concrete specimens, the projected area of the camera should be as small as possible. However, a shadow would be generated by the camera lens if the camera is set in a very low position. In this research, the camera height was set to 18cm which was slightly larger than the smallest focus distance of the lens. A concrete surface area of the size of 4.5 cm \times 3.1 cm was captured. In this way, the camera could take a high-resolution image of 5.66 μ m/pixel which could capture air voids with a minimum diameter of 10 μ m and avoid shadow caused by the camera lens (Kosmatka et al. 2002). Each concrete specimen was divided into 5 sub-specimens and a total of 15 concrete sub-specimens were collected. In this research, the total area for each concrete specimen was approximately 120 cm² and the total area surveyed for each concrete

specimen was 69.75 cm². The description of the concrete samples used in this research is shown in Table 2 and the concrete surface images are shown in Figure 10. The types of aggregates and pastes were observed and determined by an experienced petrographic technician using a microscope.

It should be mentioned that a minimum concrete surface survey area is required by ASTM C 457 for reliable air-void measurements based on the maximum size of aggregate in concrete (ASTM 2012). A larger survey area may reduce the uncertainty for the determination of air-void parameters in practice. However, the area of concrete surface surveyed should have very limited influence on the experiment result for testing the proposed automated segmentation method.

Table 2. Description of Concrete Samples

Specimen No.	Total scan	Description on Material constituent			Air content	Air void size
		Coarse aggregate	Fine aggregate	Cement		
1	5	Crushed siliceous gravel consisting of igneous, quartzite and minor amounts of other metamorphic rocks	Quartz, and siliceous sand	Type I	4.43%	Mostly in small size
2	5	Limestone	Quartz, limestone, feldspar and chert	Type I	7.26%	Mostly in small size with few in medium size
3	5	Limestone	Quartz, limestone, feldspar and chert	Type I	8.44%	Large air-void size variation with some big air voids

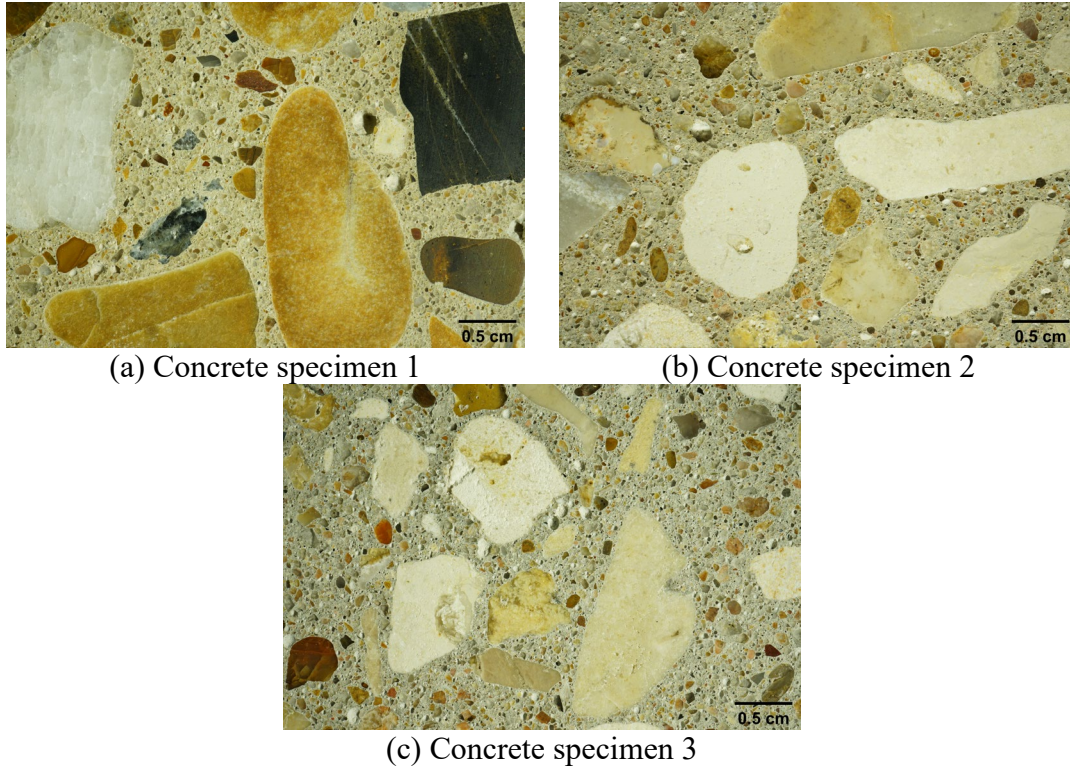


Figure 10. Concrete specimen images

4.2 Accuracy Assessment

The accuracy of the segmented results was assessed manually by manual rating and the accuracy assessment procedure developed by Song et al. (Song et al. 2020b) was followed in this research. The purpose of the accuracy assessment procedure was to provide a quantitative evaluation of the accuracy performance of the proposed 3D air-void segmentation method. The manual measurement procedure should not be required in the practical use of the proposed automated method. A 100×100 dot matrix was selected from each raw image with its corresponding segmentation result. Each dot in the dot matrix was manually annotated as air void or non-air-void by two human raters. In order to maximize the reliability and accuracy of the manually annotated ground truth data, the annotated results generated by different raters were carefully double-checked. If a

significant discrepancy was found between the annotated results generated by the two raters, the annotation process would be redone until the discrepancy was resolved. Then, pixelwise comparisons were conducted to measure the difference between the manually annotated results and segmentation results. An accuracy measurement MIoU (Mean of Intersection over Union) which is calculated by Equation (21) was utilized to evaluate the accuracy of the segmentation results.

$$MIoU = \frac{IoU_{air\ voids} + IoU_{non-air-voids}}{2} \quad (21)$$

where $IoU_{air\ voids}$ is the accuracy measurement of air voids which equals $\frac{TP}{TP + FP + FN}$;

$IoU_{non-air-voids}$ is the accuracy measurement of non-air-voids which equals $\frac{TN}{TN + FN + FP}$;

TP is the number of dots that are correctly segmented as air voids; TN is the number of dots that are correctly segmented as non-air-void; FP is the number of dots that are incorrectly segmented as air voids; FN is the number of dots that are incorrectly segmented as non-air-void.

4.3 Results and Analysis

4.3.1 Surface Normal Reconstruction

The performance of three photometric stereo models (i.e., the basic photometric stereo method, the Low-rank minimization method, and the SBL) were evaluated in this study. Computation cost and accuracy were two evaluation metrics that were utilized to evaluate the performance of the photometric stereo method. Among the three photometric stereo models, the basic photometric stereo method had the simplest computation structure assuming the concrete surface is an ideal Lambertian surface. The SBL was

theoretically the most ideal method because it considered the corruptions like attached shadow and specularities into BRDF. However, the Sparse Bayesian Learning required iterative optimization to calculate the best-fit parameters in BRDF, which may cause a higher computation cost. The performance of the Low-rank minimization method was theoretically between the basic photometric stereo method and the SBL method. Some useful depth information may be smoothed out because the method discarded corruption as outliers. A concrete specimen surface captured by the photometric stereo system is shown in Figure 11. All three photometric stereo methods were programmed using Python.

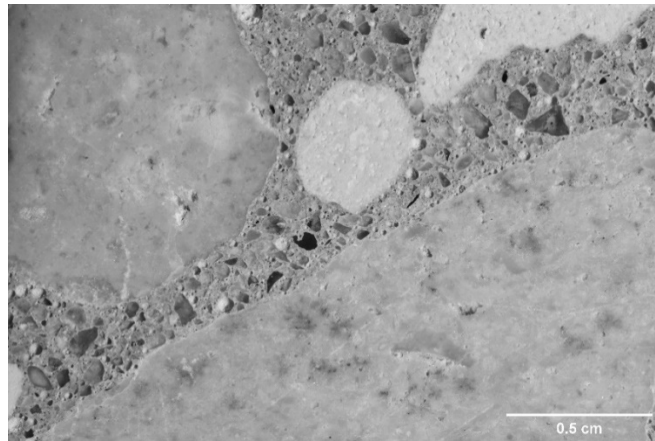
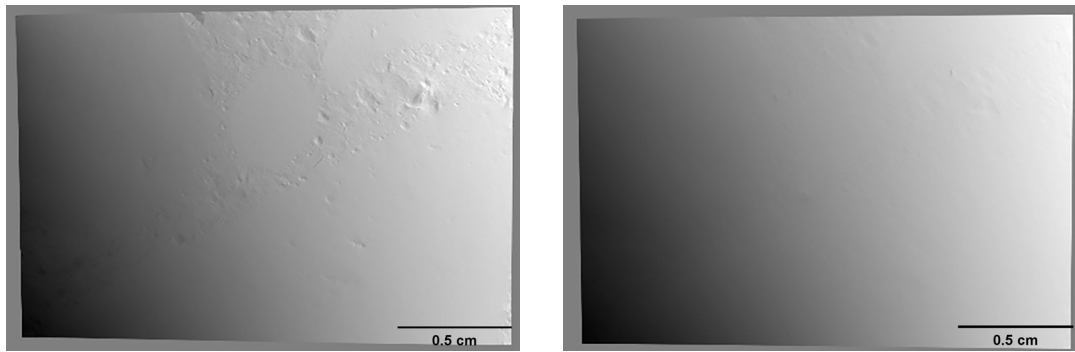


Figure 11. Concrete specimen surface



a) Basic photometric stereo method

b) Low-rank minimization method

Figure 12. Reconstructed 3D surfaces

Figure 12 presents both the depth maps of the basic photometric stereo method and the Low-rank minimization method. The depth map of the SBL is not shown in Figure 12. In this experiment, the SBL took 2 hours to calculate the normal vector of only 8,000 pixels. One possible reason could be that the six LED lighting directions were not sufficient for the SBL to construct a suitable piecewise linear function (Equation (8)) to approximate the BRDF model. Consequently, a great number of iterations were required for the SBL method to approximate the best-fit parameters in each pixel. Therefore, the SBL was not chosen for further analysis. In Figure 12, both the reconstructed concrete surfaces using the Basic photometric stereo method and the Low-rank minimization method show a slight slant. It can be clearly seen from Figure 12 that the Basic photometric stereo method presents more depth information than the Low-rank minimization method. Even though the normal vector information of some aggregates has some bias, the air voids can be clearly seen in the result of the Basic photometric stereo method. The Low-rank minimization method reduces the normal vector bias in aggregate regions, but the normal vectors in air voids regions are also over smoothed. Some air

voids cannot be clearly distinguished in the result of the Low-rank minimization method. A possible explanation is that the Low-rank minimization method discarded the attached shadows caused by air voids as outliers, and the normal vectors of most of the air-void regions were smoothed out. In addition, the Low-rank minimization method took 435 seconds to calculate the normal map of a concrete surface sample, while the Basic photometric stereo method took only 10 seconds. Based on the above comparisons and considerations, the Basic photometric stereo method was selected for the concrete surface normal calculation in the research work that followed.

4.3.2 Air-Void Segmentation

4.3.2.1 *Surface Plane Approach*

The surface plane approach requires the depth information of a concrete surface to distinguish air voids from the solid phase. The result of surface normal integration that is shown in Figure 12(a) is not a flat plane but a skewed plane. The slight skewness could be caused by error accumulation during the surface normal integration process. A Gaussian filter with a large σ^2 of 50 was utilized in this study to remove low-frequency outliers. The concrete surface profile processed with a Gaussian filter is shown in Figure 13. The biased concrete surface profile is flattened, and the air voids are well retained.

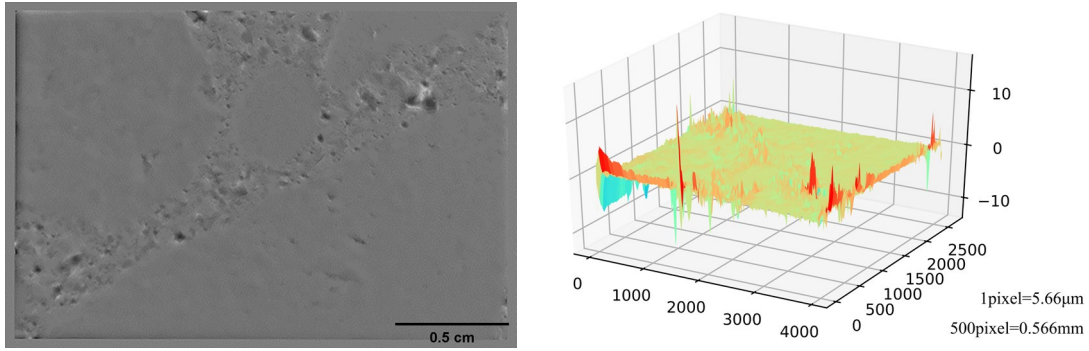


Figure 13 . Gaussian filter processed concrete surface profile

The air-void segmentation result with a rectified surface profile is shown in Figure 14. The edge of the rectified concrete surface was incorrectly identified as air voids. The reason might be that the edges of the concrete profile were not well rectified by the Gaussian filter. The Surface Plane Approach assumes that the concrete surface is a flat plane, and the air voids are the hollows in the concrete surface. The regression equation as shown in Equation (12) was used to estimate the concrete surface plane. The points below the regressed concrete surface plane were classified as air voids. The regressed concrete surface was bent and distorted due to imperfect illumination and error accumulation during the surface normal integration process and the Gaussian filter could not completely rectify the edges of the integrated concrete surface. Consequently, those points in the edge region of the concrete surface were incorrectly segmented as air voids. A portion of dark aggregates and transparent aggregates were incorrectly identified as air voids. In our study, the surface plane method did not retain the shape of air voids well. The morphology difference between the segmented air voids and aggregates was not significant enough, which discouraged further refinement. Therefore, the surface plane based approach was not chosen for further analysis.

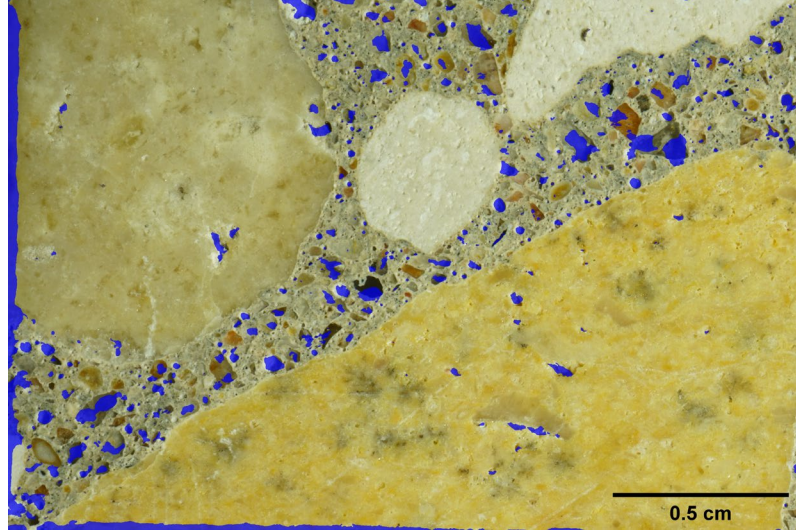


Figure 14. Air voids segmentation result with rectified concrete surface

4.3.2.2 Normal Map Approach

The surface normal approach measured the surface normal angle θ with the Z axis (calculated by Equation (11)) of each pixel based on the calculated normal map. The measurement result is presented in Figure 15. Nearly 90% of pixels in the observed concrete surface region have a slant angle under 15° . This result is consistent with the expectation on the concrete surface in which most regions have no air voids and the air voids only are distributed in a small portion of the concrete surface. Typically, the air voids in the concrete surface are regions with large slant angles. In our research, only 10% of the pixels in the observed concrete surface region had a slant angle larger than 15° . The maximum surface angle θ is around 43° because the illumination angle of the LED lights in this study was set at 45° . The actual concrete air voids have a sharper surface slant angle than the measurement result. It was because the concrete surface point with a slant angle larger than 45° would be blocked and could not be illuminated. Therefore, the maximum surface angle θ depends on the set-up slant angle of the LED

lights of the photometric stereo system.

Figure 16 presents the air-void segmentation results with surface angles 15° , 27° and 35° . The white pixels are air voids, and the black pixels represent the concrete surface. Many false positives are observed in Figure 16(a). Compared with the concrete specimen surface, it is obvious that some dark aggregates and transparent aggregates are identified as air voids. For dark aggregates, a reasonable explanation is that the basic photometric stereo method assumes the observed surface to be a Lambertian surface, while the polished concrete surface is actually not an ideal Lambertian surface. Both diffuse and specular reflectance occur on the specimen surface, especially on the polished aggregates. The transparent aggregates are another main reason causing false positives. The light passing through transparent aggregates were reflected by the cement under the aggregates. The slant angle of the cement under transparent aggregates was captured and a slant surface normal vector was calculated in the region of transparent aggregates. The bottoms of the air voids are also not correctly segmented, and the reasons are twofold. For most of the shallow air voids, the normal vectors at the bottom of air voids have relatively small surface angles. By selecting a threshold of surface angle larger than 15° , those air-void pixels that had small surface angles would always be neglected as non-air-voids. For most of the deep air voids, the bottom of the air voids is not well illuminated. The photometric stereo method assumes that the slant surface shows different illumination intensities under various illumination conditions. The 45° incident light could be blocked by the edge of deep air voids, which made the bottom of the air voids show the same dark color under various illumination conditions. Consequently, the photometric stereo method may have recognized the bottom of the air voids as a 'surface

plane' which had surface angles approximately to 0° .

As shown in Figure 16(b) and 15(c), by choosing a larger surface angle threshold, the false positives caused by aggregates are eliminated to some extent, but the number of missing air voids is increasing. Increasing the surface angle threshold of air voids can significantly reduce false positive air voids, but some shallow and small air voids could be omitted causing more false negatives. In order to capture most of air voids in concrete specimen surfaces, 15° was selected as the threshold of surface angle. The surface pixels with a slant angle larger than 15° were segmented as air voids. It should be noted that the 15 degree threshold was used to separate air voids and concrete surface/solid phase based on the experiment data from this research. It should also be mentioned that some small air voids were missed in the segmentation result of the normal map method, even though the high-resolution camera could capture the smallest air voids of $10\ \mu\text{m}$ in diameter. Actually, different types of voids including entrained air voids, voids in aggregates, and entrapped air voids could be segmented as air voids using this method.

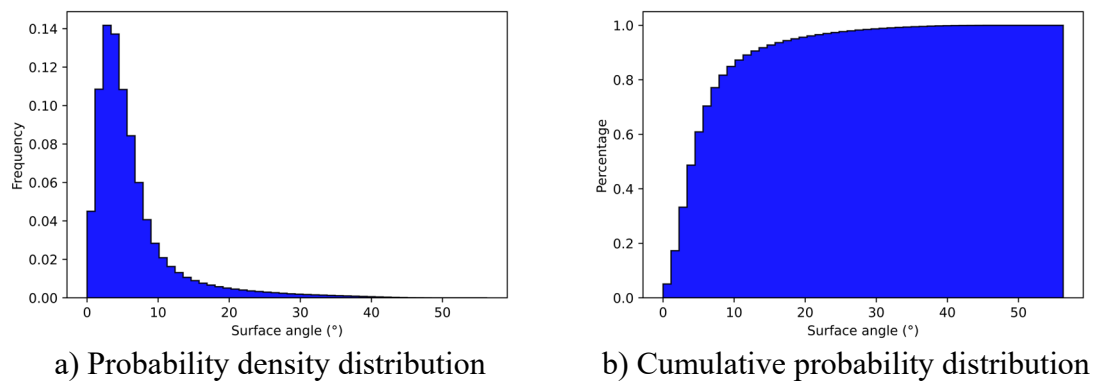


Figure 15. Measurement results of surface angle θ

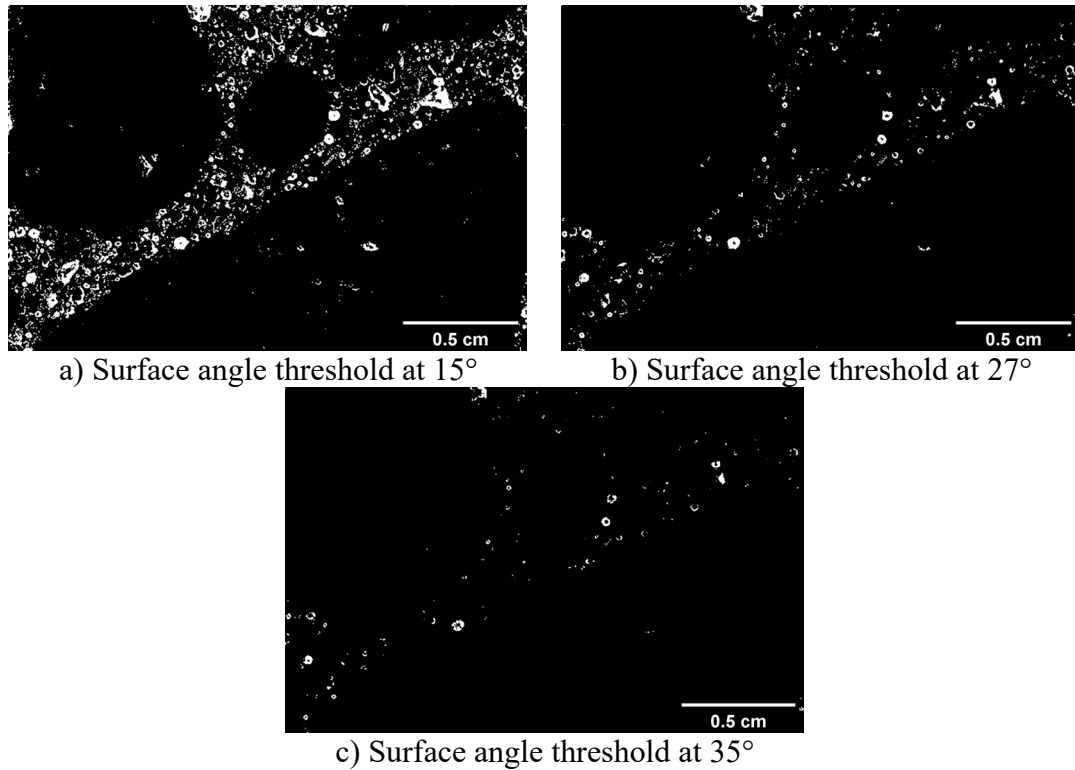
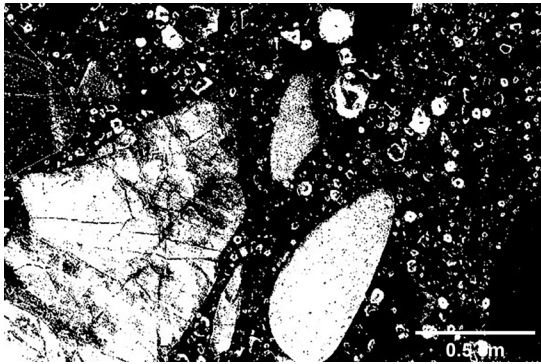


Figure 16. Air voids segmentation results with surface angle thresholds 15°, 27° and 35°

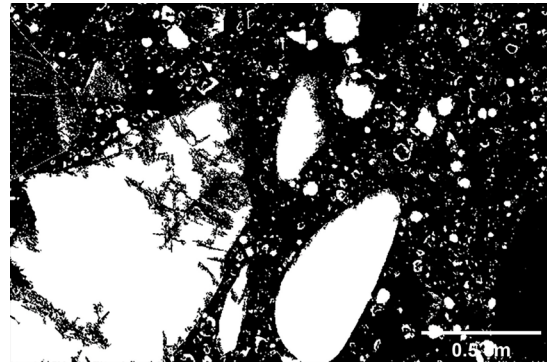
4.3.2.3 Segmentation Refinement

Figure 17 shows the segmentation results refined by the FillHole method. It can be clearly seen that the holes of the segmented shapes are filled up. It should be mentioned that not only the ‘holes’ in air voids, but also the ‘holes’ in aggregates were filled up. After numerous tests, 0.4 was selected as the threshold for distinguishing air voids and aggregates. The segmentation result is presented in Figure 18. The accuracy variations of some concrete specimens under different area ratios are shown in Figure 19. By investigating Figure 19, both sample 1 and sample 2 achieve the highest MIoU with an area ratio at 0.4. However, due to the diversity of aggregates, 0.4 may not be always the best threshold for every concrete specimen to separate air voids and aggregates. Some correctly segmented air voids could have an aggregate appearance and some incorrectly

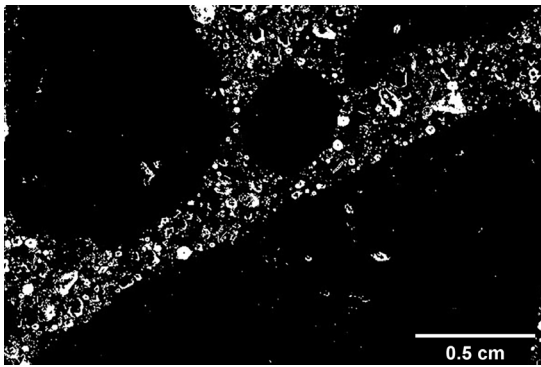
segmented air voids could have an air-void appearance. The most significant difference between the segmented shape with a large area ratio and the segmented shape with a small area ratio would be in the probabilities for which the segmented shape is an air void or an aggregate. The segmented area with a small area ratio is more likely to be an aggregate, and the segmented area with a large area ratio is more likely to be an air void. It is worth noting that the dark or transparent aggregates with round shapes may not be ideally removed by using the AreaRatio method. Most of the voids in aggregates are well removed by the AreaRatio method due to the irregular shape. However, the AreaRatio method may not work well for rounded or well-rounded voids in aggregates. As shown in Figure 18(c), there are many tiny white dots on the left of the image. The white dots are rounded voids in coarse aggregates. Both issues could be alleviated by further improving 3D reconstruction technologies, combining depth/normal information with color information, and using Artificial Intelligent methods. Given the limited space of this article, this issue will not be furtherly discussed. As shown in Figure 19(c), sample 3 achieves the highest MIoU with an area ratio less than 0.4 but 0.4 is still selected as the threshold value to eliminate false positive air voids. One of the reasons was that those large aggregates could be effectively removed when the area ratio was larger than 0.4. And the concrete specimens with a best-fit area ratio less than 0.4 always showed a comparable MIoU when the area ratio was set to 0.4.



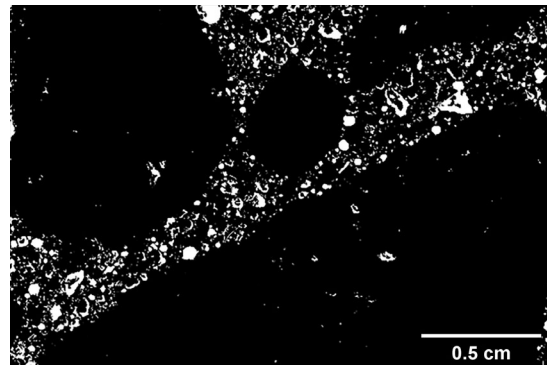
i) Before
(a) Sample in specimen 1



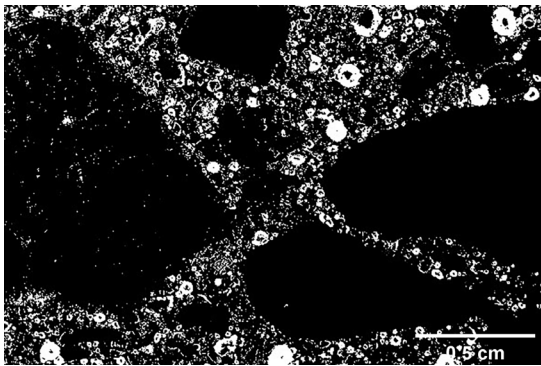
ii) After



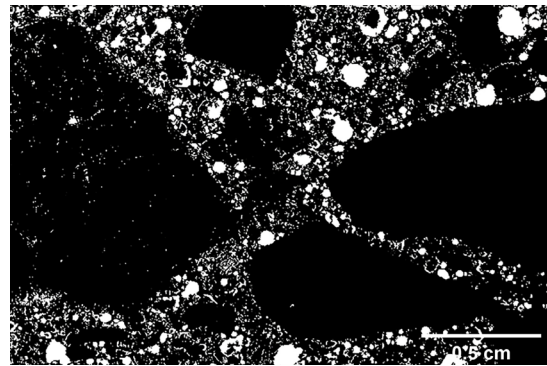
i) Before
(b) Sample in specimen 2



ii) After

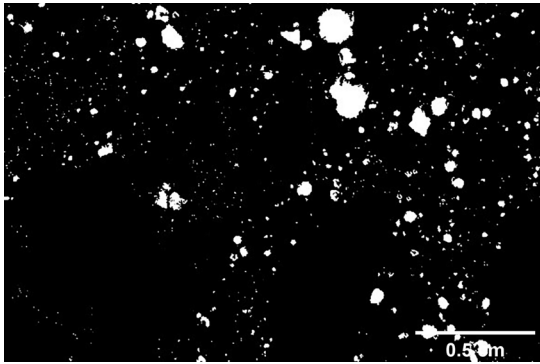


i) Before
(c) Sample in specimen 3

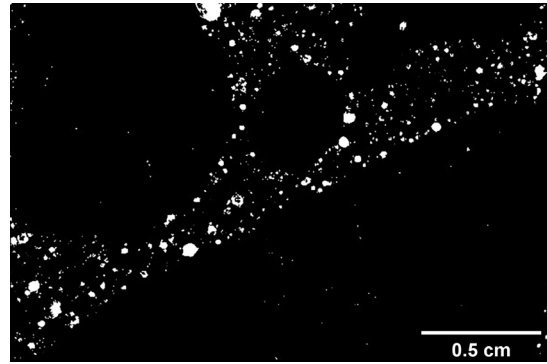


ii) After

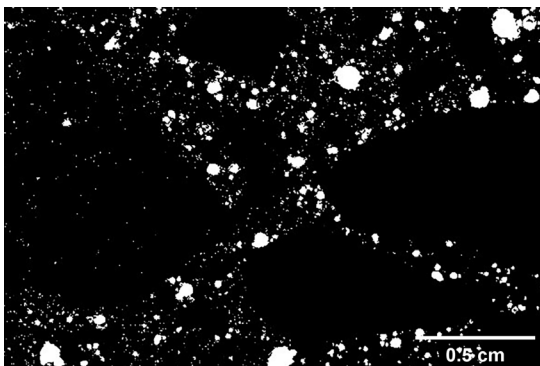
Figure 17. Segmentation result using FillHole



(a) Sample in specimen 1

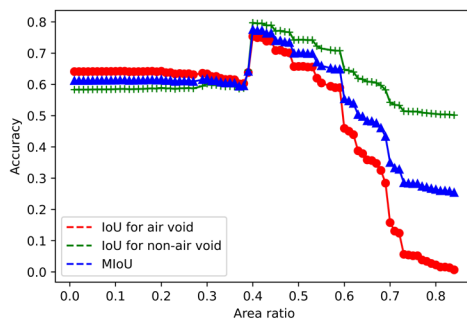


(b) Sample in specimen 2

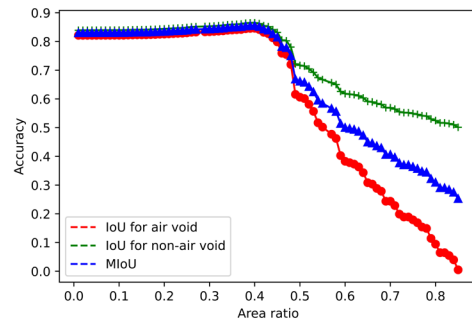


(c) Sample in specimen 3

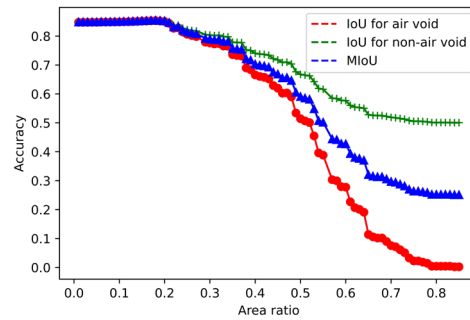
Figure 18. Segmentation result using AreaRatio



a) Sample in specimen 1



b) Sample in specimen 2



c) Sample in specimen 3

Figure 19. Segmentation accuracy under various of area ratios

The accuracy statistics of the segmented concrete specimen are shown in Table 3. In Table 3, both the MIoU measurements calculated with an area ratio of 0.4 and best-fit area ratio are presented. The best-fit area ratio is the area ratio that corresponds to the highest segmentation accuracy. No significant difference was found between the segmentation accuracy of various concrete specimens. The MIoU of the segmentation result with an area ratio of 0.4 is 0.725 and the MIoU of the segmentation result with best-fit area ratio is 0.797, which indicates that the proposed method can distinguish the air voids from the concrete surface and possesses a comparable accuracy with the manual method. The best-fit MIoU is a little higher than the MIoU with an area ratio of 0.4 and most of the concrete samples reach the highest segmentation accuracy with area ratios around 0.2. Although some concrete samples could achieve a more accurate segmentation result by choosing an area ratio of 0.2, 0.4 is more robust for removing large false positives caused by large dark aggregates. The total computation time for the proposed air-void segmentation method was around 20s by using a desktop equipped with an ‘Intel i7 8th gen’ CPU and 32GB RAM.

Table 3. Segmentation Accuracy for Concrete Specimens

Specimen No.	Sub-specimen No.	IoU with area ratio 0.4			Best-fit IoU			
		Air voids	Non-air voids	MIoU	Air voids	Non-air voids	MIoU	Area ratio
1	1	0.623	0.822	0.722	0.652	0.821	0.737	0.24
	2	0.754	0.797	0.775	0.754	0.797	0.775	0.4
	3	0.560	0.742	0.651	0.645	0.761	0.703	0.15
	4	0.664	0.744	0.704	0.843	0.857	0.850	0.26
	5	0.725	0.773	0.749	0.779	0.801	0.790	0.2
2	1	0.846	0.865	0.856	0.846	0.865	0.856	0.4
	2	0.627	0.704	0.665	0.716	0.743	0.730	0.23
	3	0.607	0.712	0.659	0.746	0.788	0.767	0.22
	4	0.718	0.766	0.742	0.819	0.825	0.822	0.25
	5	0.737	0.785	0.761	0.844	0.854	0.849	0.2
3	1	0.637	0.716	0.676	0.725	0.755	0.740	0.27
	2	0.666	0.740	0.703	0.853	0.857	0.855	0.18
	3	0.780	0.813	0.797	0.875	0.879	0.877	0.21
	4	0.645	0.721	0.683	0.833	0.828	0.830	0.08
	5	0.709	0.753	0.731	0.764	0.773	0.769	0.21
Average				0.725	0.797			

4.4 Summary

In this chapter, a photometric stereo based automated air-void segmentation method was proposed. The new method can be applied directly to the concrete specimen without contrast enhancement and could distinguish air voids from the concrete surface time-efficiently. The research results have shown that:

(1). Compared with the SBL and the Low-rank minimization method, the Basic photometric stereo method shows a good performance both in 3D reconstruction accuracy and computation cost. However, the Basic photometric stereo method is designed for Lambertian surfaces and the polished concrete surface cannot be considered as an ideal Lambertian surface. Specularity which is a kind of non-Lambertian effect can be found in concrete surface images and lead to errors. According to the size of the specularity, the specularity observed in the concrete image can be classified into two

categories. The specularities with a small size can always be found in transparent aggregates and has a limited influence on air voids segmentation, whereas the specularities with a large size which can be found in dark aggregates has a significant influence on air-void segmentation. A photometric stereo method that incorporates the image corruption into the surface normal calculation with an acceptable computation cost could improve the accuracy of air-void segmentation;

(2). The shadow caused by air voids should be reserved for the photometric stereo method to correctly extract the normal vector of air voids. The photometric stereo method which considers the image corruptions as outliers could over smooth the concrete surface normal map and neglect air voids;

(3). Compared with the surface plane approach, the normal map approach is more effective. On one hand, more computation procedures are required by the surface plane approach. The Gaussian filter-refined surface normal integration method which takes more than 5 mins to be finished is required by the surface plane approach. On the other hand, the surface normal approach tends to retain more boundary and shape information of air voids than the surface plane approach;

(4). The FillHole method can fill up the 'holes' in the bottom of most air voids. However, the FillHole method does not work well when the segmented air void does not show in the shape of a closed circle. Those unfilled air voids generally have irregular shapes and are prone to be removed by the AreaRatio method which causes false negatives. A photometric stereo system with more lighting directions may reduce such false negatives;

(5). The AreaRatio method could be designed and used to eliminate the false positives caused by dark aggregates and transparent aggregates like chert and quartz. For dark aggregates, the specular reflectance on the specimen surface leads to biases in 3D reconstruction results. For transparent aggregates, the light passing through transparent aggregates is reflected by the cement paste under the aggregates instead of the aggregate surface. The photometric stereo method fails to reconstruct an accurate 3D surface of neither the dark aggregates nor the transparent aggregates, which therefore leads to confusion between air voids and the dark or transparent aggregates during the segmentation process. The false positives caused by the coarse aggregates are much easier to be eliminated than the false positives caused by the fine aggregates such as natural sand. The false positives caused by fine aggregates always have similar morphology characteristics as air voids. The fine dark aggregates and fine transparent aggregates are the two main error sources of false positives in this study.

5. REFINEMENT OF THE AUTOMATED AIR-VOID SEGMENTATION RESULTS USING DEEP LEARNING METHODS

According to the research results in chapter 4, the photometric stereo method does contrast the air voids from the hardened concrete surface to some extent, while the air voids cannot be accurately segmented from the contrasted concrete surface using conventional image processing methods. As a subarea in artificial intelligence (AI), deep learning (DL) has achieved great success in semantic segmentation. During the semantic segmentation process, a classification label is predicted on each pixel, which may greatly fulfill the objectives of air-void segmentation. The deep convolutional neural networks (DCNN), which is an important branch in DL, show good potential in detecting target objects in noisy images at pixel resolution. Another advantage of DCNN is the end-to-end segmentation manner. Significant fewer human interventions are required to be involved in the segmentation work. Song et al. (Song et al. 2020b) made an innovative attempt at using DCNN methods to segment the phases in hardened concrete surfaces. The proposed air-void segmentation method outperformed the contrast-enhancement method and achieved much higher accuracy in the boundary area between each phase. However, the air voids still need to be highlighted using orange chalk powders, which made the method not fully automatic.

The objective of this chapter is to propose an end-to-end automated segmentation method that could detect air voids in concrete surfaces without contrast enhancement. In the chapter, an air-void image dataset including a set of surface normal images and air-void annotations was first developed. The surface normal images were generated from the surface normal vectors of concrete surfaces which were estimated using the

photometric stereo method. The annotations were first obtained using the contrast-enhancement method and then refined by human raters. Consequently, as a DCNN model, U-Net was trained using the air-void dataset for detecting air voids in hardened concrete images. Finally, the segmentation results were manually evaluated using a set of accuracy measurement indexes.

5.1 Data Acquisition and Description

5.1.1 Hardened Concrete Samples

Deep learning methods require a large-scale image dataset for training purposes. Therefore, additional hardened concrete specimens were requested and provided by the concrete laboratory of the Texas Department of Transportation (TxDOT). Considering the fact that the appearance of the concrete specimens could affect the semantic segmentation results, the concrete specimens with various aggregate types and cement types were selected as experimental specimens. All the selected concrete specimens were drilled and sampled from an in-service concrete pavement structure. The details of the experimental specimens are described in Table 4. The specimen surfaces were polished according to the specifications in ASTM C457. To fit the field-of-view of the photometric stereo system, the original samples were sub-sliced into $4\text{cm} \times 5\text{cm}$ small pieces, and a region of $3\text{cm} \times 4.5\text{cm}$ was captured as the field-of-view. Consequently, A total of 12 pieces of sliced concrete samples were utilized for the training purpose. For each category of the hardened concrete samples, one slice was utilized for testing purposes. There were a total of 5 pieces of sliced concrete samples utilized for the testing purpose.

Table 4. Description of experimental specimens

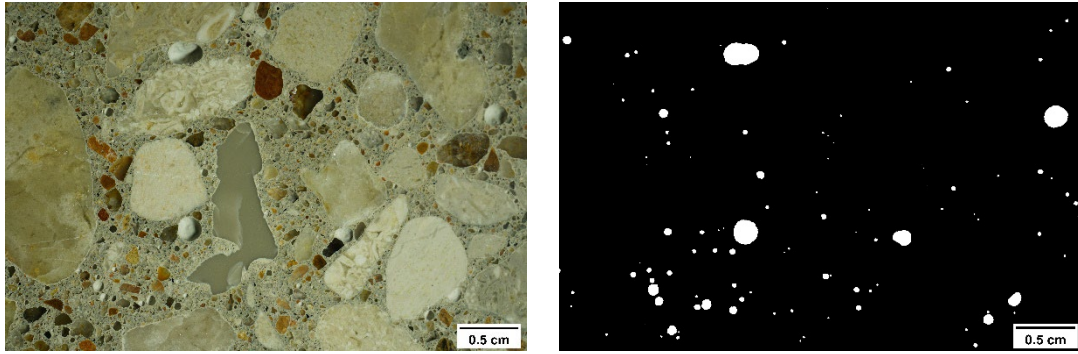
Specimen No.	Total scan	Description of material constituents	
		Coarse aggregate	Fine aggregate
1	3 1(test)	Limestone	Quartz, limestone, chert, granite and feldspar
2	2 1(test)	Limestone	Manufactured sand, quartz, feldspar and chert
3	1 1(test)	Limestone, quartz and chert	Quartz, limestone, sandstone, igneous and siliceous
4	3 1(test)	Limestone, siliceous, igneous chert and quartzite	Limestone, siliceous, igneous chert and quartzite
5	3 1(test)	Sandstone, limestone and igneous	Quartz, limestone, sandstone, igneous and siliceous

5.1.2 Data Annotation and Registration

The labels of training data were first annotated using a contrast-enhancement method, and then manually refined. Acrylic ink and a rubber brayer were adopted to blacken the polished concrete surfaces (Fonseca and Scherer 2015). The applied acrylic ink could generate a thin dark layer without filling out air voids. In case some aggregates cannot be ideally painted, the missed regions were carefully re-painted with a marker pen. The specimens were then left to air dry at room temperature for 30 minutes. After the ink was dried thoroughly, a barium sulfate powder with an average particle size of $3\mu\text{m}$ was used to highlight the air voids into white color. The barium sulfate powders were scattered on the hardened concrete surface and then pressed into air voids using hand fingers. The excess powders were removed with the edge of a silicone spatula. The images of the contrast enhanced concrete surfaces were captured using the photometric stereo system that is shown in Figure 9. The system consisted of six LED lights and was designed for illuminating the concrete samples in different directions. The details of the setup and utilization of the photometric stereo system are described in section 4.1.1 ‘Instrument Setup’ section. All six LED lights were lighted to generate a uniform

illumination on the concrete surfaces. Finally, an image-processing software (ImageJ) was used to segment the air voids from the enhanced concrete images by setting a gray value threshold. The Otsu method was utilized to provide an optimal threshold. In the case when the Otsu method did not generate an ideal threshold, the generated threshold may be manually adjusted. The non-air-void regions in the concrete images such as cracks, voids in aggregates and the region with residual barium sulfate powder were double-checked and removed by the rater using Adobe Photoshop. It is worth mentioning that the contrast enhancement process is only used for data preparation. During the 3D reconstruction and image segmentation process, no contrast enhancement is required for concrete samples.

The raw concrete images and the enhanced concrete images were captured in two different scans in sequence. The hardened concrete surface was first scanned using the photometric stereo system to obtain the 3D surface normal image of the hardened concrete surface. The concrete specimen was then taken away from the testbed of the photometric stereo system for contrast-enhancement procedure. After the enhancement procedure, the concrete sample was relocated to the testbed and scanned to capture the contrast-enhanced image. Even though careful locating was exercised to ensure the hardened concrete was aligned to the same position as the first scan, slight displacements were still observed between the two scans. The DCNNs require accurate annotations, and the labels and image features are expected to correspond at the pixel level. Therefore, the images of the two scans were manually adjusted using Adobe Photoshop to match up at each pixel in the two scans. An example of a hardened concrete image and its annotated air-void image is shown in Figure 20.



(a) Hardened concrete surface

(b) Annotated air voids

Figure 20. An example of the manually annotated air-void image.

5.1.3 Surface Normal Image Capturing

As discussed in Chapter 3, various photometric stereo methods were compared for the extraction of 3D air-void information. The conventional photometric stereo method that was proposed by Woodham outperformed the other photometric stereo methods and could extract the gradient of air voids. The Woodham's photometric stereo method, which is shown in Equation (2), utilizes the relationship between incoming lighting direction $L \in \mathcal{R}^{k \times 3}$, surface normal $N \in \mathcal{R}^{3 \times 1}$, and observed intensity $I \in \mathcal{R}^{k \times 1}$ to compute the surface normal of each pixel (Woodham 1980).

A diagram of an estimated surface normal vector on a hardened concrete surface is shown in Figure 21. n_x , n_y , and n_z are the components of surface normal vector in x, y and z directions at the point (x,y,z) . The components n_x , n_y , and n_z in the computed surface normal vector were then normalized to the $(-1, 1)$ scale. Whereas the DCNNs are designed for RGB images and the intensity of pixels in each channel is between 0 to 255. To ensure the surface normals compatible with the DCNNs, the n_x , n_y , and n_z of each pixel were mapped from $(-1, 1)$ to $(0, 255)$. An example of the mapping process with a 4

pixels \times 4 pixels image is shown in Figure 22. N_x , N_y , and N_z are surface normal matrices that contain the components that are involved in x, y, and z directions. The r , g , and b are pixel intensities in red, blue, and green channels. For example, n_{x11} , n_{y11} , and n_{z11} are the components of the surface normal at pixel (1,1) in x, y, and z directions. The r_{11} , g_{11} , and b_{11} , which are mapped by n_{x11} , n_{y11} , and n_{z11} , are the pixel intensity of the pixel (1,1) in red, blue, and green channels, respectively.

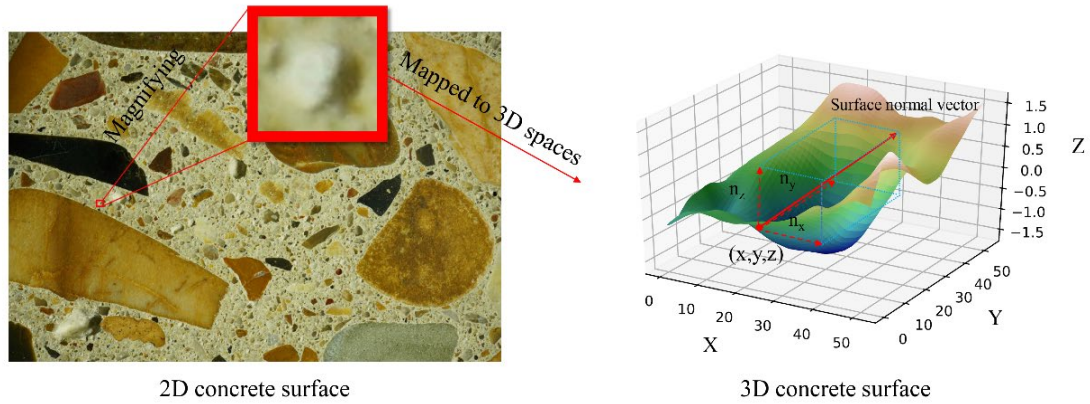


Figure 21. Illustration of surface normal vector on a concrete surface.

$$\begin{aligned}
 & \left(\begin{matrix} n_{x11} & n_{x12} & n_{x13} & n_{x14} \\ n_{x21} & n_{x22} & n_{x23} & n_{x24} \\ n_{x31} & n_{x32} & n_{x33} & n_{x34} \\ n_{x41} & n_{x42} & n_{x43} & n_{x44} \end{matrix} + \begin{matrix} 1 & 1 & 1 & 1 \\ 1 & 1 & 1 & 1 \\ 1 & 1 & 1 & 1 \\ 1 & 1 & 1 & 1 \end{matrix} \right) * \frac{255}{2} = \begin{matrix} r_{11} & r_{12} & r_{13} & r_{14} \\ r_{21} & r_{22} & r_{23} & r_{24} \\ r_{31} & r_{32} & r_{33} & r_{34} \\ r_{41} & r_{42} & r_{43} & r_{44} \end{matrix} \\
 & \hspace{10em} \text{Red Channel} \\
 & \left(\begin{matrix} n_{y11} & n_{y12} & n_{y13} & n_{y14} \\ n_{y21} & n_{y22} & n_{y23} & n_{y24} \\ n_{y31} & n_{y32} & n_{y33} & n_{y34} \\ n_{y41} & n_{y42} & n_{y43} & n_{y44} \end{matrix} + \begin{matrix} 1 & 1 & 1 & 1 \\ 1 & 1 & 1 & 1 \\ 1 & 1 & 1 & 1 \\ 1 & 1 & 1 & 1 \end{matrix} \right) * \frac{255}{2} = \begin{matrix} g_{11} & g_{12} & g_{13} & g_{14} \\ g_{21} & g_{22} & g_{23} & g_{24} \\ g_{31} & g_{32} & g_{33} & g_{34} \\ g_{41} & g_{42} & g_{43} & g_{44} \end{matrix} \\
 & \hspace{10em} \text{Green Channel} \\
 & \left(\begin{matrix} n_{z11} & n_{z13} & n_{z13} & n_{z14} \\ n_{z21} & n_{z22} & n_{z23} & n_{z24} \\ n_{z31} & n_{z32} & n_{z33} & n_{z34} \\ n_{z41} & n_{z42} & n_{z43} & n_{z44} \end{matrix} + \begin{matrix} 1 & 1 & 1 & 1 \\ 1 & 1 & 1 & 1 \\ 1 & 1 & 1 & 1 \\ 1 & 1 & 1 & 1 \end{matrix} \right) * \frac{255}{2} = \begin{matrix} b_{11} & b_{12} & b_{13} & b_{14} \\ b_{21} & b_{22} & b_{23} & b_{24} \\ b_{31} & b_{32} & b_{33} & b_{34} \\ b_{41} & b_{42} & b_{43} & b_{44} \end{matrix} \\
 & \hspace{10em} \text{Blue Channel} \\
 & \text{Matrix of surface normal} \hspace{15em} \text{RGB space}
 \end{aligned}$$

Figure 22. Mapping surface normal to RGB space.

5.2 Image Augmentation

To make the training process more efficient, a set of data augmentation procedures were conducted on the training data. Considering the shapes of the air voids can be a critical differentiation factor for distinguishing the air voids, the ineffective modifications can lead to a decreased segmentation accuracy. For example, the compressing and stretching modifications, which change the height and width ratio of the air-void image, change the shape of the air voids and thus make the air voids confused with the air-void like noises. In this research, the effectiveness of using various image augmentation procedures was evaluated. Random combinations of flipping, rotating, and scaling modification were applied. Scaling and rotating operations significantly increased the number of images for the training. However, both scaling and rotating operations generated a margin between the augmented images and the edges of the pictures. Consequently, two fill modes were introduced to fill the margins. Three image augmentation strategies, as shown in Table 5, were developed to investigate the best augmentation strategy for the segmentation of air-void images. An example of the augmented image using different augmentation strategies is shown in Figure 23. During the training process, the images were randomly cropped into 256 pixels \times 256 pixels small pieces and 10,200 cropped images were generated. 80% of the crops were adopted as training data and 20% of the crops were adopted as validation data.

Table 5. Augmentation strategies

Augmentation Strategy	Flipping	Rotating	Scaling	FillMode	Images for Training
Augmentation 1	√	√	√	wrap	27,000
Augmentation 2	√	√	√	constant	27,000
Augmentation 3	√	×	×	×	18,000

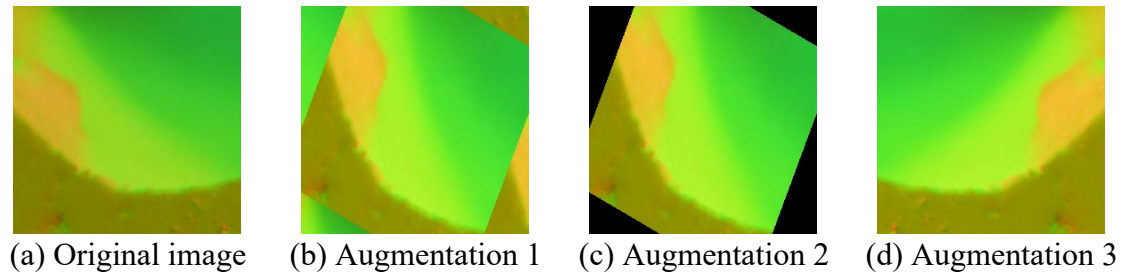


Figure 23. Augmented images using different augmentation strategies

5.3 Accuracy Assessment

The accuracy assessment procedure in this section is similar to the accuracy assessment procedure in 3.3 ‘Accuracy Assessment’. An accuracy measurement procedure that is similar to the Modified Point Count method (ASTM 2012) was utilized for evaluating the accuracy of the proposed method. Song et al. also adopted a similar accuracy measurement procedure in one of their previous research studies (Song et al. 2020b). A 100×100 dot matrix was generated and appended to both the segmented images and the raw concrete images. The pixels in the raw concrete images that are corresponding to the appended dot-matrix were manually observed by an experienced petrographer. According to the observation, the dots in the dot matrix were labeled as air voids and non-air voids. The dots in the dot matrixes that were appended to the segmented images were also labeled by identifying the color of the corresponding pixel in the segmented images. The dot that was appended to a white pixel was labeled as air voids. The dot that was appended to a black pixel was labeled as non-air voids. The labeling process for the segmented images was done automatically using a program coded in Python. Consequently, accuracy measurements including MIoU (Mean of Intersection over Union), P (precision), R (Recall), and F_1 , which can be calculated by Equations (22)-(27), were utilized to evaluate the accuracy of the segmentation results.

$$IoU_{air\ voids} = \frac{TP}{TP + FP + FN} \quad (22)$$

$$IoU_{non-air-voids} = \frac{TN}{TN + FN + FP} \quad (23)$$

$$MIoU = \frac{IoU_{air\ voids} + IoU_{non-air\ voids}}{2} \quad (24)$$

$$P = \frac{TP}{TP + FP} \quad (25)$$

$$R = \frac{TP}{TP + FN} \quad (26)$$

$$F_1 = \frac{2TP}{2TP + FP + FN} \quad (27)$$

TP is the percentage of dots that are correctly segmented as air voids; TN is the percentage of dots that are correctly segmented as non-air-void; FP is the percentage of dots that are incorrectly segmented as air voids; FN is the percentage of dots that are incorrectly segmented as non-air-void.

5.4 Results and Analysis

5.4.1 Surface Normal Image Generated Using Photometric Stereo Method

An example of the raw concrete surface and the mapped surface normal image is shown in Figure 24. Compared with the original concrete surface image, the surface normal image increased the contrast in uneven areas. The areas with a slant surface normal can be distinguished by identifying the color changes on the surface normal map. The areas with uniform pale green are the solid phase (aggregates and paste). The round

areas with large color variations in a circle are the air voids.

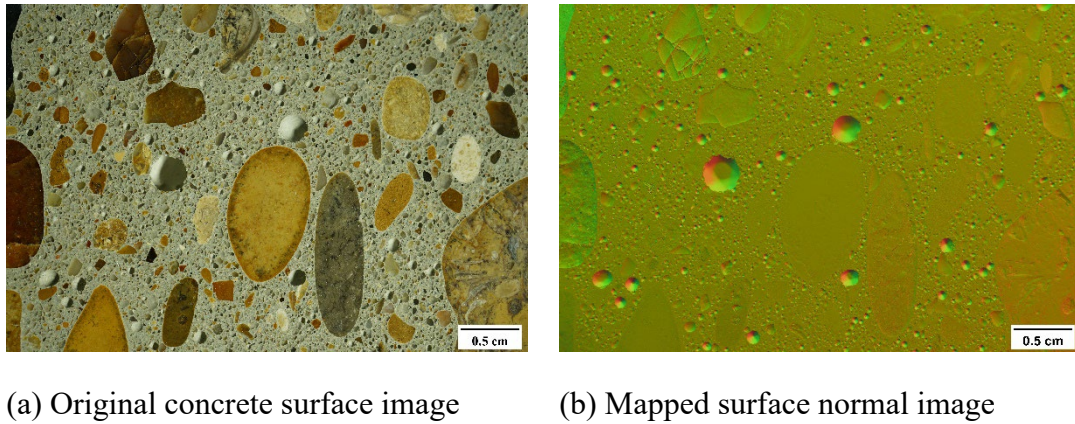


Figure 24. The air voids in original concrete surface image and surface normal image.

As shown in Figure 24, the air voids in the mapped surface normal image present a clear pattern and can be easily identified by naked eyes. Figure 25 presents various appearances of air voids and air-void like noises on concrete surface normal images. As shown in Figure 25, the regions of some dark or transparent aggregates also present a color variation. The photometric stereo method estimates the surface normal of a target object by the intensity of reflected light. Under various lighting directions, a slant surface presents a great intensity variation, while a flat surface generates an identical surface intensity. The dark aggregates were apt to produce specularities under a specific lighting angle and thus lead to a biased slant surface normal estimation. For the transparent aggregates, the lights are transmitted down to the bottom of the aggregates and reflected by the paste. Biased slant surface normal estimations were produced by the transparent aggregates. Consequently, the photometric stereo method inaccurately estimates the normal information in the region within some transparent aggregates and dark aggregates.

The biased estimation generated air-void like appearances in the surface normal map. The similarity made the automated identification of air voids in hardened concrete a challenge. In addition, the air voids are not the only ‘hollows’ in concrete surfaces. The voids and cracks in aggregates are another kind of ‘hollows’ in concrete surfaces that can be mistaken as air voids.

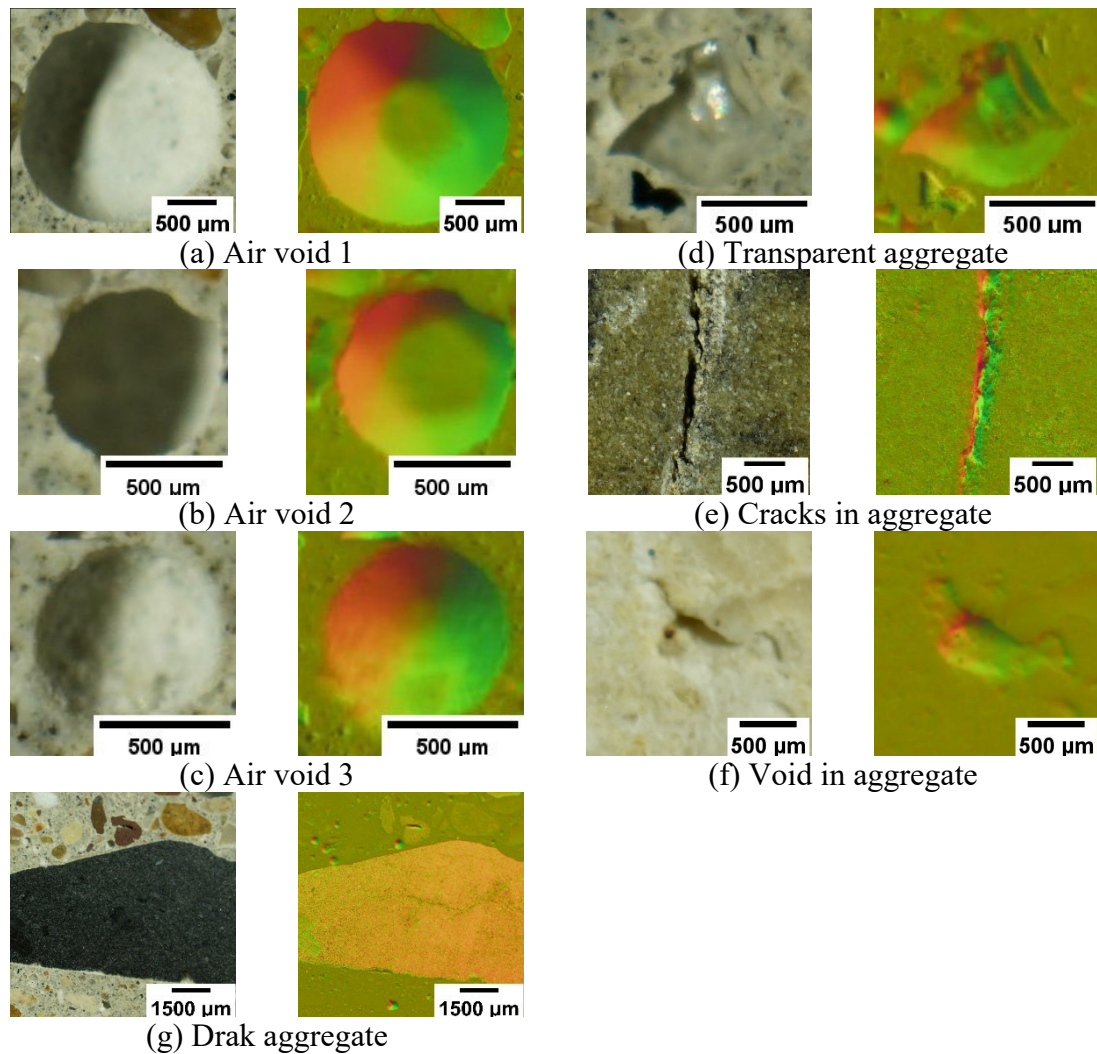


Figure 25. Air-void appearances and air-void like noises generated by components on concrete surfaces.

The air voids with different sizes and depths presented different appearances. Inside

some deep air voids, a ‘flat region’ can be observed. The ‘flat regions’ were caused by occlusions. The lights were blocked by the edge of air voids and did not reach the bottom of the air voids. Thus, the photometric stereo system failed to capture the information at the bottom of the air voids. The system assumed those regions as a flat plane because there was no intensity variation captured in the blocked regions. On the other hand, in shallow air voids, the color variation was too little and sometimes can be mistaken as non-air-void regions. Therefore, even though the air voids were highlighted in the surface normal image, the diversity of air-void appearances and various air-void like noises made the air-void detection a tough work.

5.4.2. Evaluation of Different Augmentation Strategies

Table 6 presents the evaluation results of the U-Net model trained with different image augmentation strategies. All 3 models were trained for 780 epochs to ensure convergence. As shown in Table 6, the training result of Augmentation 1 is almost the same as the evaluation result of Augmentation 2. Whereas a 3.7% difference is observed between the evaluation results of validation data. The comparison between Augmentation 1 and Augmentation 2 indicates that the ‘constant’ fill mode helps the U-Net model improve robustness. By comparing Augmentations 1 and 2 to Augmentation 3, the U-Net model which was trained with the images augmented with the strategy of Augmentation 3, is significantly better than the other two U-Net models. It is worth noting that the number of images generated by Augmentation 3 is $\frac{2}{3}$ of the total images generated by Augmentation 1 or Augmentation 2. A reasonable explanation for the observation is that the shape information, which is important for distinguishing air voids, is well retained in the training data using the strategy of Augmentation 3. Consequently, the strategy of

Augmentation 3 was used in the research.

Table 6. Training results of U-Net model using different augmentation strategies

Augmentation Strategy	Epochs	Learning Rate	Best Train MIoU	Best Val MIoU
Augmentation 1	780	0.001	0.681	0.610
Augmentation 2	780	0.001	0.691	0.647
Augmentation 3	780	0.001	0.814	0.706

5.4.3 Air-Void Segmentation Results of U-Net model

The U-Net was trained using surface normal images and annotated air-void masks. The model was trained for 780 epochs and the training work took about 15 hours to accomplish. The variations of MIoU and loss during the training process were recorded in each epoch and presented in Figure 26.

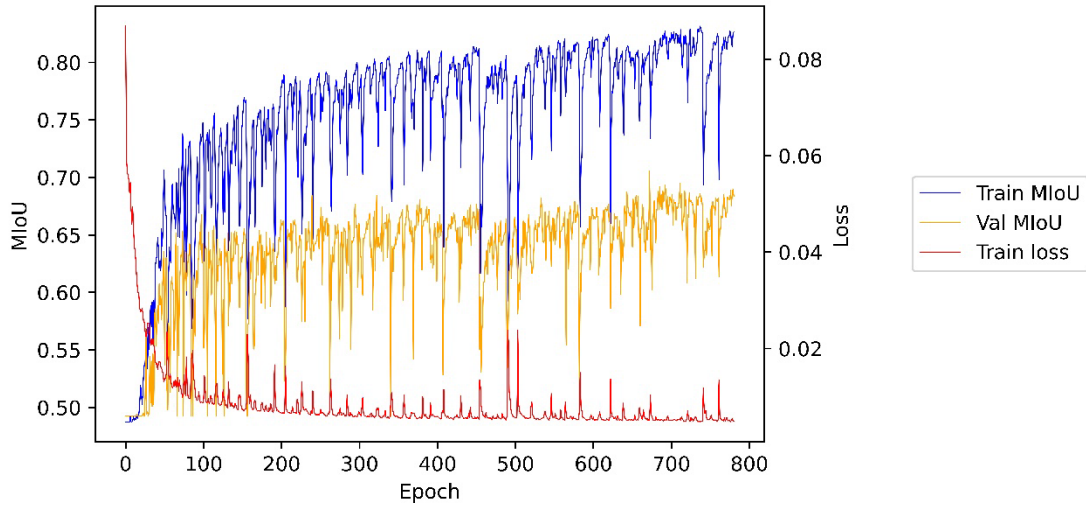


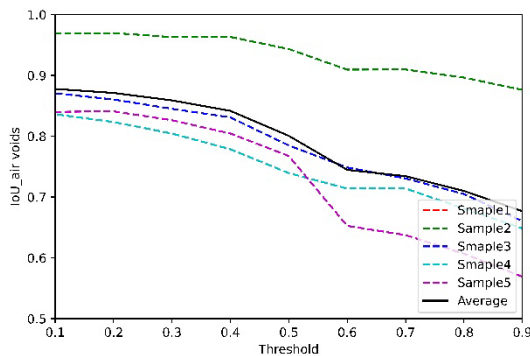
Figure 26. The loss and MIoU curves of the U-Net model training.

The loss estimates the discrepancy of predicted results and labels, and a lower loss indicates a better segmentation performance. The loss curve presents some fluctuations and shows a decreasing trend. The variation trend of the loss curves slows down with the

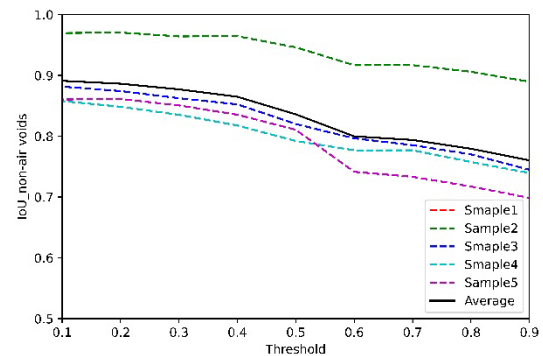
increase of the number of epochs and becomes stabilized when the loss value approaches 0.005. The train_MIoU and val_MIoU measure the similarity of predicted results and labels for the training set and validation set, respectively, and a higher MIoU indicates a better segmentation performance. The MIoUs of the training dataset and validation dataset are combining, and an increasing trend is found for both curves. The loss curve reversely correlates with the MIoU curves. As shown in Figure 26, the decreasing trend of the loss curve stabilizes after 650 epochs, which indicates that the model is converged.

The size of the input of the U-Net model was 256 pixels \times 256 pixels which was much smaller than the size of the raw concrete surface images. Consequently, the raw concrete surface images were cropped into 256 pixels \times 256 pixels small pieces and fed into the trained U-Net, one cropped image at a time to generate an output. After all the cropped images were processed, the processed images were then stuck together as the segmentation result of the raw concrete surface image. The U-Net model computed on each pixel and output a 256 \times 256 matrix. Each value in the matrix was from 0 to 1, where 0 means the pixel was most likely from the background (non-air-void) and 1 means the pixel was most likely from the target object (air voids). Some raw output values that are close to 0 are found inside some air-void regions. To make a binary air-void segmentation, the selection of a threshold between 0 to 1 is needed to classify a pixel as air void or non-air void. The accuracy measurements of the test samples with different thresholds are presented in Figure 27. As the threshold increases, the IoUs show slight downward trends. Consequently, 0.1 was chosen as the threshold for achieving the best MIoU. To evaluate the influence of the threshold to air-void parameters, the estimated air-void parameters of each threshold were also calculated. As the concrete samples did

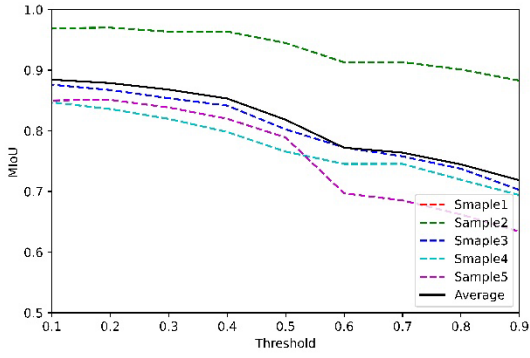
not come with the measured paste content, 27%, which is recommended as a good estimation in FHWA petrographic manual, was used as the estimated paste content (Walker et al. 2006). The air-void parameters were measured using the Procedure B Modified Point-Count Method. As shown in Figure 27(d) and 26(e), it can be observed that the best-fit threshold for air content is 0.5 and the best-fit threshold for spacing factor is 0.6. The results indicate that the importance of the segmentation error in different locations is not the same. By observing the segmentation results, it can be found that a lower threshold helps to reduce the FN segmentation error inside large air voids, while a lower threshold increases the FP segmentation errors which are mainly FP fine air voids. Most of the FP fine air voids are caused by the misidentified fine aggregates. The discretely distributed fine FP air voids have a significant impact on the measurement of air content and spacing factor. It is worth mentioning that even though a lower threshold has a significant influence on FP fine air voids, but it barely impacts the segmentation result of TP fine air voids. Consequently, the correct segmentation of fine air-voids and aggregates is highly important for the accurate measurement of air-void system.



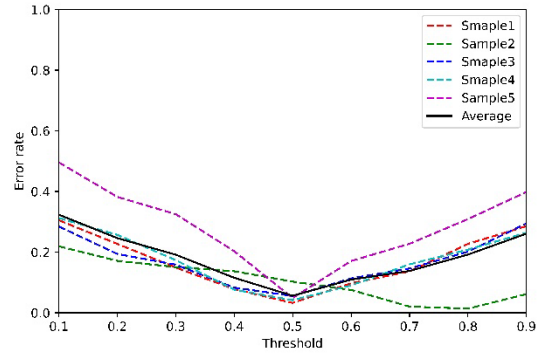
(a) $\text{IoU}_{\text{air voids}}$



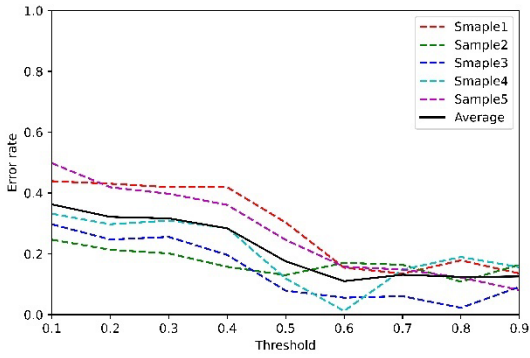
(b) $\text{IoU}_{\text{non-air voids}}$



(c) MIoU

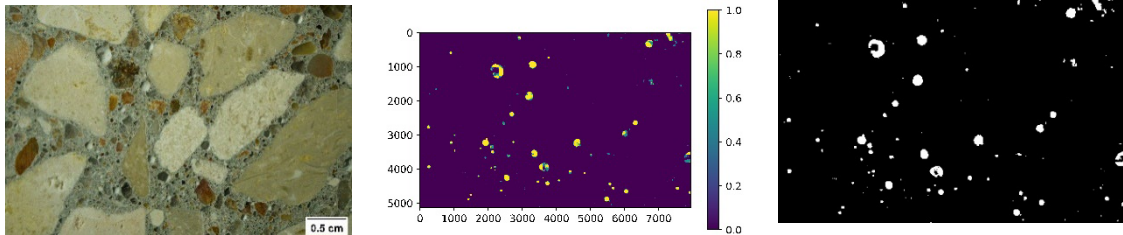


(d) Air content

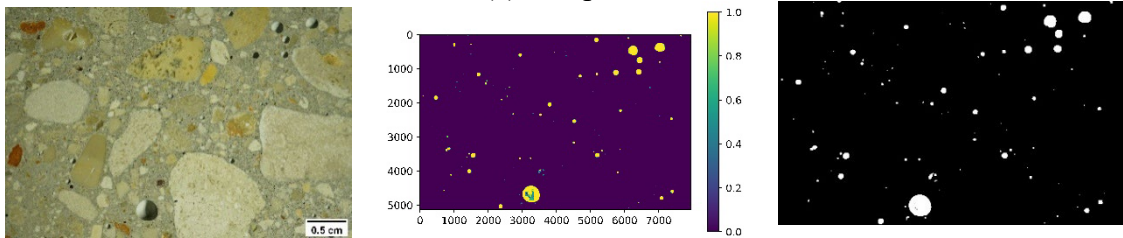


(e) Spacing factor

Figure 27. Accuracy measurement of test samples with different thresholds.



(a) Sample 1



(b) Sample 2

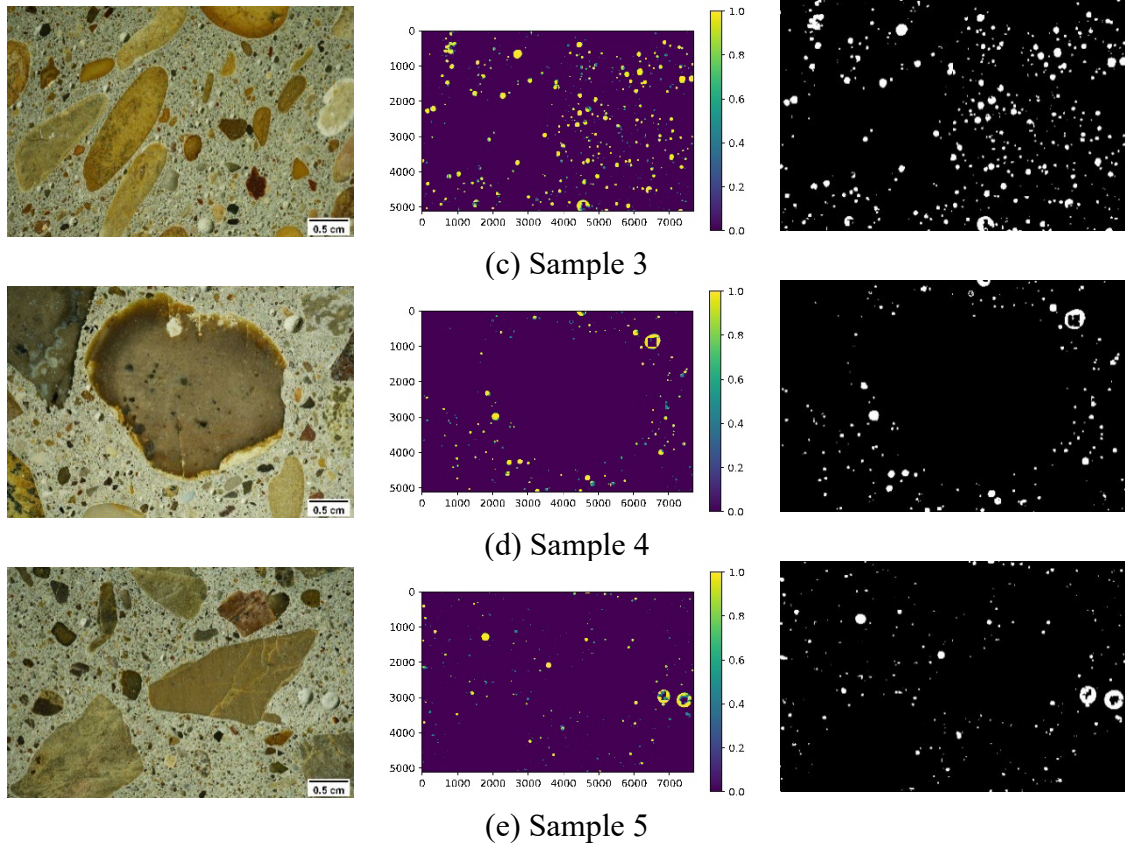


Figure 28. Air-void segmentation results of test concrete samples. The sequence of each image in the subplot is raw hardened concrete image, raw segmentation result (raw output by the U-Net model), and binary segmentation result (segmented air-void image using 0.1 as threshold).

The segmented concrete images with the threshold of 0.1 are presented in the binary segmentation results of Figure 28. The air voids are labeled as white, and the non-air voids regions are labeled as black. As discussed previously, many air-void like noises can be generated in surface normal images using photometric stereo methods. The trained model correctly identified most of the biased regions and only a small percent of the biased regions was incorrectly identified as air voids. Some well-rounded fine aggregates can be false positively segmented as air voids, while the percentage of those FP

segmentations is not significant. In addition, most of the voids and cracks in aggregates were well identified as non-air voids. However, some well-rounded voids in aggregates were still incorrectly segmented as air voids. Also, some missing air voids were observed in the segmentation result. Most of the missing air voids were deep air voids. Those air voids generally could be easily identified using naked eyes, but these kinds of air voids presented a significantly different appearance in the surface normal map, which caused interference to the correct air-void image segmentation. One of the reasons that led to the missing segmentation could be the quantity of training data was not sufficient for the U-Net to learn the pattern of tiny or shallow air voids. Another explanation could be the 256 pixels \times 256 pixels sliced training images were not big enough to entirely contain some large-size air voids. Consequently, the U-Net model failed to capture valid features to represent the large size air voids. As shown in Figure 29, 3 image sizes were selected to make a random cropping from an image with a large air void and an image with a large aggregate. It can be clearly observed that the air void and the aggregate can barely be differentiated from the 256 pixels \times 256 pixels cropped images. As the image size becomes larger, the patterns of air voids and aggregates can be identified more easily.

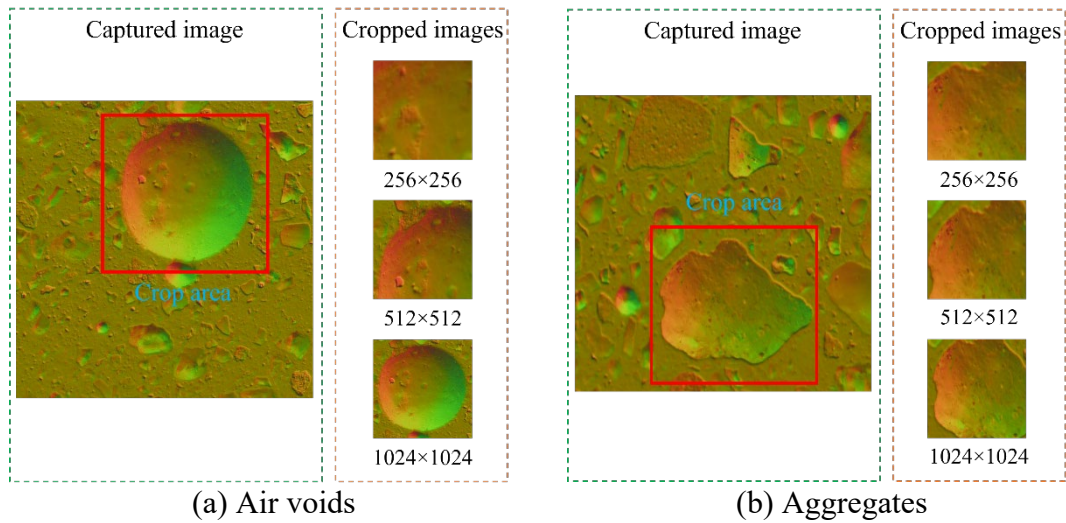


Figure 29. Random cropping using different cut sizes

To further quantify the observations of the segmentation results. The accuracy measurements for the testing samples are presented in Table 7. The testing samples were first scanned using the photometric stereo system and the surface normal images were then mapped from the estimated surface normal vectors. All the air-void segmentation results were output by the trained U-Net512 model based on the surface normal images. Equations 19-24 were adopted for calculating the accuracy indices. As shown in Table 7, the average of the MIoU of five testing samples is 0.884, which indicates that the proposed method could detect the air voids in hardened concrete surface with a relative good accuracy. The average FP is 0.009 and the average P is 0.990, which indicate that the proposed method could differentiate the air voids from most of the air-void like noises and only a small portion of air-void like noises was incorrectly identified as air voids. The average FN is 0.115 and is almost 10 times as great as FP. In addition, R is 0.885 which is nearly 0.1 less than P. Both FN and R indicate that the misidentification was the major source of segmentation errors.

Table 7. Accuracy measurement for testing samples

Specimen No.	FP	FN	TP	TN	P	R	F ₁	IoU _{air-void}	IoU _{non-air-void}	MIoU
1	0.007	0.121	0.879	0.993	0.992	0.879	0.932	0.873	0.886	0.880
2	0.004	0.027	0.973	0.996	0.996	0.973	0.984	0.969	0.970	0.969
3	0.019	0.113	0.887	0.981	0.979	0.887	0.931	0.871	0.882	0.876
4	0.006	0.159	0.841	0.994	0.993	0.841	0.911	0.836	0.858	0.847
5	0.007	0.154	0.846	0.993	0.991	0.846	0.913	0.840	0.860	0.850
Average	0.009	0.115	0.885	0.991	0.990	0.885	0.934	0.878	0.891	0.884

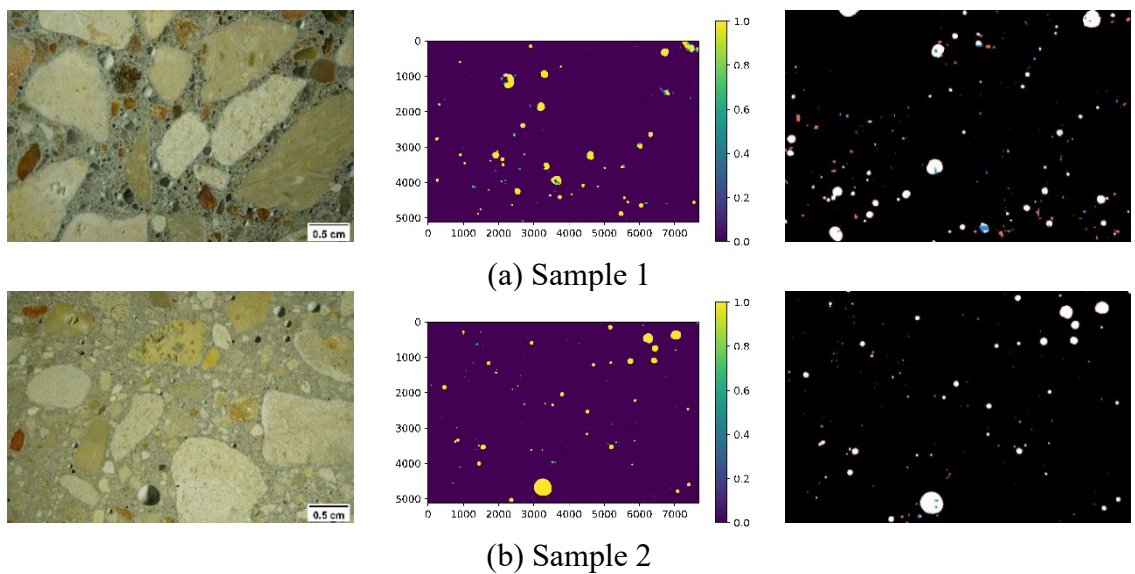
Consequently, the segmentation results of the concrete surface images using the U-Net model trained with different cropped image sizes (256×256, 512×512, and 1024×1024) are presented in Table 8. After various experiments, it can be observed that the image size has an impact on the air-void segmentation performance. The U-Net512, which was trained using 512 pixels × 512 pixels images, showed a slightly better performance in generalization than the other two models. Even though a higher train accuracy is observed for U-Net256, the U-Net512 performs better in validation data.

Table 8. U-Net models trained with different image sizes

Model	Image Size	Augmentation Strategy	Images for Training	Batch Size	Best Train MIoU	Best Val MIoU
U-Net256	256 × 256	Augmentation 3	18,000	32	0.814	0.706
U-Net512	512 × 512	Augmentation 3	10,187	16	0.794	0.724
U-Net1024	1024 × 1024	Augmentation 3	1,906	4	0.825	0.707

Figure 30 shows the air-void segmentation results using U-Net512. In the raw segmentation results, the output value of a purple pixel is close to 0 and the output value of a yellow pixel is close to 1. TP pixels are marked in white color, TN pixels are marked in black color, FN pixels are marked in blue color, and FP pixels are marked in red color. Compared with the segmentation results using U-Net256, the large air voids can be

identified more completely. Also, some air-void like noises can be better differentiated using U-Net512. The detailed accuracy measurements of U-Net512 are estimated and presented in Table 9. As shown in Table 9, the average MIoU is 0.914 and indicates that U-Net512 model was quite capable of precisely distinguishing the air voids from the non-air-void regions. Compared to the segmentation measurements of U-Net256, the average MIoU of U-Net512 is 0.03 higher than the average MIoU of U-Net256. Additionally, the U-Net512 significantly reduces the number of misidentified air voids. The FN is reduced by 0.03 and the R is increased by 0.03. While the U-Net512 does not show a significant impact on the FP and P. Both FP and P are slightly increased by 0.001. The size of the minimum air void that can be segmented by U-Net512 is around $22\mu\text{m}$ (4-pixel length). Table 10 presents the measurement of air-void parameters using U-Net512 results and ground truth. The air-void parameters are measured using the Procedure B Modified Point-Count Method. 27% is assumed as the measured paste content. As shown in Table 10, the average measurement errors of air content, specific surface, and spacing factor for the three hardened concrete specimens are 7.87%, 9.36%, and 12.23%, respectively.



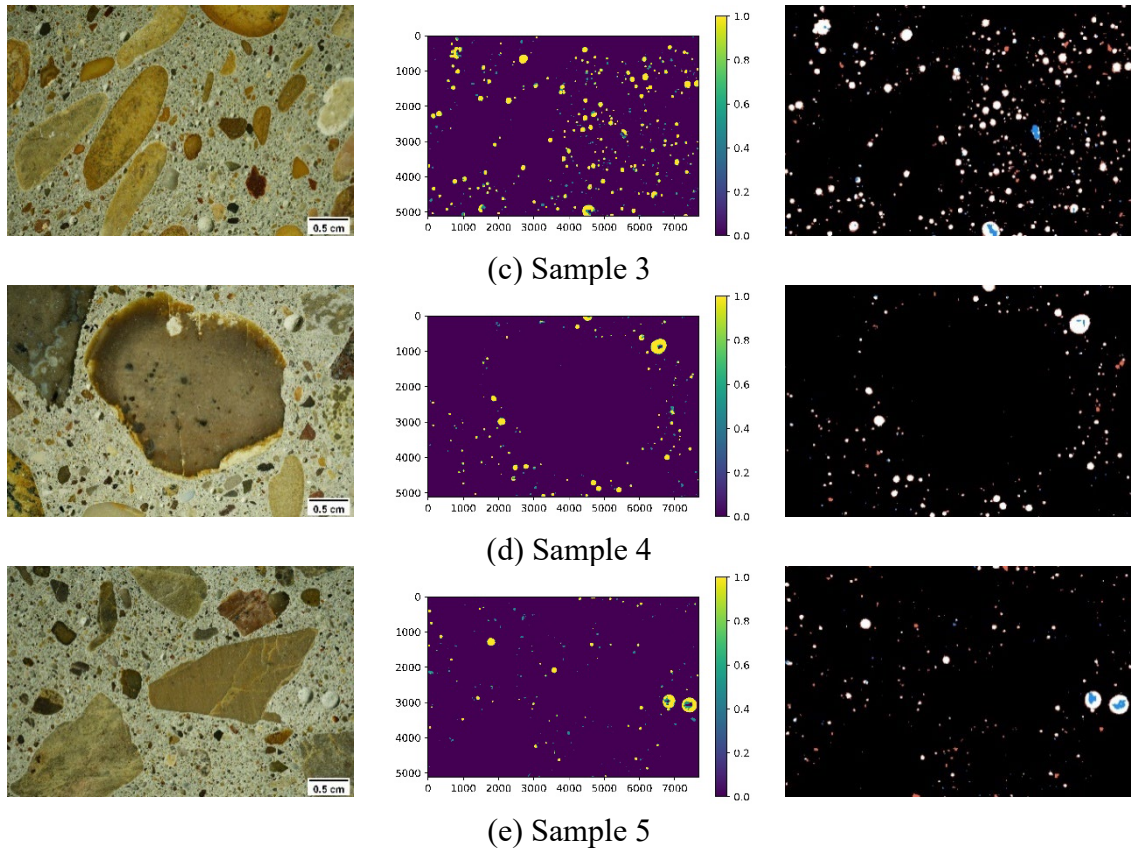


Figure 30. Air-void segmentation results of test concrete samples using U-Net512. The sequence of each image in the subplot is raw hardened concrete image, raw segmentation result (raw output by the U-Net model), and binary segmentation result.

Table 9. Accuracy measurement for testing samples using U-Net512

Specimen No.	FP	FN	TP	TN	P	R	F ₁	IoU _{air void}	IoU _{non air-void}	MIoU
1	0.008	0.115	0.885	0.992	0.991	0.885	0.935	0.878	0.890	0.884
2	0.003	0.014	0.986	0.997	0.997	0.986	0.991	0.983	0.983	0.983
3	0.019	0.092	0.908	0.981	0.980	0.908	0.943	0.892	0.899	0.895
4	0.006	0.073	0.927	0.994	0.994	0.927	0.959	0.922	0.927	0.924
5	0.006	0.115	0.885	0.994	0.993	0.885	0.936	0.879	0.891	0.885
Average	0.008	0.082	0.918	0.992	0.991	0.918	0.953	0.911	0.918	0.914

Table 10. Air-void Parameters Measured on U-Net512 results and Ground Truth using Point Count Method

		Air content (%)		Specific surface (mm-1)		Spacing factor (mm)	
		Measurement value	Error (%)	Measurement value	Error (%)	Measurement value	Error (%)
1	U-Net512	1.64	6.49	13.152	25.75	0.288	25.32
	Ground truth	1.54		10.459		0.386	
2	U-Net512	1.63	11.64	10.397	1.29	0.367	11.57
	Ground truth	1.46		10.264		0.415	
3	U-Net512	4.08	2.77	17.644	10.16	0.086	11.67
	Ground truth	3.97		16.016		0.098	
4	U-Net512	1.6	11.11	16.194	2.15	0.24	11.89
	Ground truth	1.44		15.854		0.272	
5	U-Net512	1.32	7.32	15.491	7.45	0.304	0.68
	Ground truth	1.23		16.738		0.302	
Average error (%)			7.87		9.36		12.23

Compared with contrast enhancement based method, the proposed method also achieved a significant improvement in efficiency and comparable accuracy. For a concrete surface image with a resolution of 7953*5304 pixels, the construction of the surface normal image of concrete surface took 10 to 15 seconds to accomplish, and the segmentation of a concrete surface normal image took 15 to 20 seconds to accomplish. The segmentation time for air voids in hardened concrete is significantly reduced to around half a minute.

5.5 Summary

This chapter investigated the potential of combining deep learning and 3D reconstruction techniques to detect air voids in hardened concrete surfaces, extracted and processed from concrete pavement structures. The proposed method can automatically detect the air voids in hardened concrete surfaces without the use of contrast enhancement, which reduces labor intensiveness and improves time efficiency. The research has achieved the following: 1) An air-void dataset, which consists of a group of surface normal images and air-void annotations, was developed for DCNN training. 2) The surface normal images of concrete surfaces were captured using a 3D reconstruction method. In the surface normal images, the air voids were automatically highlighted by color variations without the use of contrast enhancement method. 3) A DCNN model was trained using the developed air-void dataset for air-void detection. 4) A rigorous manual verification was conducted to obtain a reliable reference for evaluating the segmentation accuracy pixel-to-pixel. The research results have shown that:

(1) The 3D reconstruction method can capture depth variations and automatically highlight the air voids in the hardened concrete surface, while some transparent aggregates, dark aggregates, and voids in aggregates are highlighted as well. Most of the air-void like noises can be effectively identified using the proposed method.

(2) The appearance of air voids in surface normal images can vary. Some deep air voids can generate a significantly different appearance in the surface normal images, which could greatly harm the segmentation results. Increasing the number of training data that contains deep air voids or refining the illumination angle of the photometric stereo system can help improve the segmentation results of deep air voids.

(3) Shapes and gradient variations of air voids are two important characteristics of air-void segmentation. Inappropriate augmentation methods can change the appearances of air voids in training data set and then cause a poor generalization. The selection of image augmentation methods has a significant impact on the air-void segmentation results.

(4) The over 0.9 average MIoU of the DCNN segmentation indicates that the DCNN has a good potential in extracting the features from the surface normal images and making predictions at the pixel level. The U-Net model can correctly segment most of the air-void regions. The mis-identified air voids are the key error resources. The FP segmentation of some fine aggregates has the most significant impact on the measurement of air-void system.

6. EVALUATION OF THE SALTYKOV METHOD FOR RESTORING SPATIAL AIR-VOID DISTRIBUTION

The air-void segmentation methods proposed in previous chapters provide a feasible way for the measurement of air-void parameters based on the ASTM C457 standard. However, the Power's spacing factor, which is generally accepted as an air-void parameter for the evaluation of concrete freeze-thaw performance, is calculated based on the assumption that the air voids in hardened concrete form a mono-sized sphere system. The major difference between the concrete void system and the mono-sized sphere system is that the population of air voids varies significantly with the void size. As a result, the reliability of the Power's spacing factor has been debated in many research studies. A lot of attention has been paid to proposing a new evaluation index for the freeze-thawing performance of hardened concrete.

Recently, Larson et al. proposed a Protected Paste Volume (PPV) method as a new way to characterize the freeze-thaw performance of hardened concrete (Larson et al. 1967). The PPV method assumes that each air void can protect the concrete paste within a certain range. By measuring the percentage of concrete paste protected, the freeze-thawing performance can be estimated. According to Song et al. (Song et al. 2021), the spatial air-void distribution is important for reliable PPV analysis, while the state-of-the-art PPV analysis is conducted solely based on the information from 2D air-void intersections, which can result in many uncertainties. The Saltykov method, which was originally proposed by Russ et al. (Russ and Dehoff 2012), has been used to estimate the actual 3D air-void distribution. However, no study has precisely analyzed the reliability of using the Saltykov method to estimate the 3D air-void distribution. Most of the studies

acknowledged the reliability of Power's method due to its aggressive assumptions and unreliable measurement results, nevertheless, they still use air-void parameters measured by Power's method as ground truth to evaluate the 3D air-void distribution estimated using the Saltykov method. In this chapter, the reliability of the Saltykov method will be evaluated in a more intuitive way.

6.1. Synthetic Spatial Air-void Model

6.1.1 Construction of Spatial Air-Void Model

One of the biggest obstacles to evaluate the unfolded 3D air-void distribution is the lack of accurate and feasible physical measurement methods for measuring the actual 3D air-void distribution in hardened concrete. Some research studies tried to overcome this problem by using CT scanners or ultrasonic equipment to characterize the actual distribution of air voids in hardened concrete, however, both methods have their technical limitations in practical use (Guo et al. 2016, Lu et al. 2017). In this research, a set of synthetic spatial air-void models were developed to simulate the actual air-void distribution. The synthetic air-void models will be used for the evaluation of unfolded 3D air-void radius distribution.

Specifically, entrained air voids and entrapped air voids are two major void components that need to be measured in a hardened concrete sample. Generally, the entrained air voids are spherical voids that are larger than the capillaries with a radius less than 0.5 mm. The entrapped air voids are spherical voids with a radius larger than 0.5 mm and can range up to several millimeters. Many scholars believe that the freeze-thawing performance is mainly affected by the entrained air voids and slightly affected

by entrapped air voids (Fonseca and Scherer 2015) and therefore they only include entrained air voids in concrete freeze-thaw analysis. While other scholars believe it is not the case since there is no provision made for distinguishing between entrained air voids and entrapped air voids in the ASTM C457. Hence, they consider both entrained air voids and entrapped air voids in the analysis. In this research, both situations were considered for the construction of the spatial air-void models.

In addition, the air-void size distribution is another key evaluation parameter for the measurement of the air-void system in hardened concrete. For the air-void size distribution measurement, there is no widely accepted theory that can be used as a reference. Fonseca et al. observed bubble profiles from images of typical air-entrained mortar and the distribution of air-void radius showed a lognormal-like distribution (Fonseca and Scherer 2015). Yun et al. investigated the distribution of void size distribution using CT scan techniques. Both probability density functions and corresponding cumulative distribution functions were visualized and affirmed the air-void diameter follows a lognormal trend (Yun et al. 2012). Guo et al. studied the air-void distribution in hardened concrete using a non-destructive ultrasonic scattering technique. Both lognormal distribution and normal distribution were adopted to fit the distribution of entrained air voids. Based on the research results, the normal distribution fits the measured air-void distribution better than the lognormal distribution (Guo et al. 2016). Consequently, in order to simulate the air-void system in hardened concrete with more generalizability, both lognormal distribution and normal distribution were considered as possible air-void distributions.

Based on the above analysis, the following assumptions were made to simulate the

spatial air-void model:

(1). The air-void system in hardened concrete consists of only entrained air voids or a mixture of entrained and entrapped air voids;

(2). The radius of entrained air voids should not exceed 0.5 mm;

(3). The radius of entrapped air voids should not exceed 1 mm;

(4). Both entrained air voids and entrapped air voids in the simulated system are spherical;

(5). Air voids are randomly distributed throughout the specimen without any regular packing.

The flow chart of the construction of the spatial air-void model is shown in Figure 31. A set of parameters for constructing 3D air-void models were designed first, including distribution parameters, air content, specimen boundary, void size range, and void counts. The distribution parameters and void count are then used for the generation of random radius. After that, a radius scale is calculated to rescale the generated radius. The objective of this step is to rescale the generated air voids and to make the rescaled air-void system fit the pre-designed air content. Fourthly, the range of the rescaled radius is verified with the pre-designed void size range based on the given maximum and minimum value. If the rescaled radius did not fit with the pre-designed void size range, a new set of pre-designed parameters for radius distribution will be attempted until the rescaled radius fit with the pre-designed void size range. Consequently, the coordinate of each air void was generated randomly within a restricted boundary (35.8 mm × 23.5 mm × 15 mm) and each air void was recorded using a four-dimensional vector (x_i, y_i, z_i, r_i) ,

where x_i , y_i , and z_i represents the coordinate of a generated void i , r_i is the radius of a generated void i . It is worth mentioning that the randomly generated void coordinate can be overlapped with each other. Hence, a program was developed to detect and re-allocate the overlapped air voids. More specifically, the overlap is first detected by calculating the distance between the center of any two voids. If the distance is smaller than the sum of the radius of the two voids, the two voids are then marked as 'overlap'. The void with a smaller radius is then re-allocated with a new coordinate randomly. The re-allocation process will not stop until the re-allocated void does not overlap with any other voids in the synthetic void system. Once all the voids in the synthetic void system are checked and no overlapped void pair is detected, the synthetic void system is finalized for further analysis.

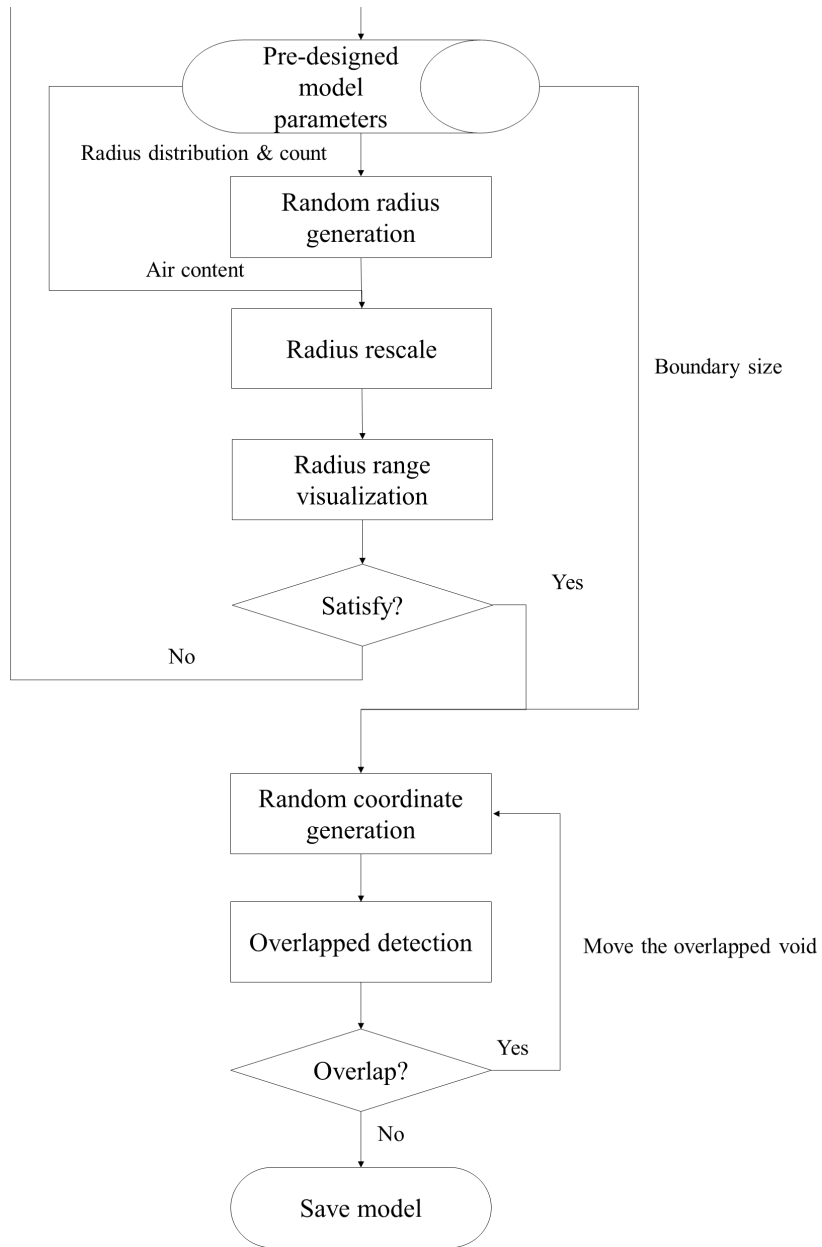


Figure 31. Flow chart for constructing the synthetic air-void model

Table 11 shows the parameters used for the construction of six synthetic spatial air-void models. 32,000 air voids are simulated within a synthetic boundary with length, width, and height equal to 3.58 cm, 2.38 cm, and 1.5 cm, separately. Mu and Sig are distribution parameters for both lognormal and normal distributions, while the meanings

of Mu and Sig in different distributions are different. For the lognormal distribution, Mu and Sig are the mean and the standard deviation of the distribution of log(void radius), respectively. For the normal distribution, Mu and Sig are the mean and the standard deviation of the distribution of void radius, respectively.

Table 11. Parameters used for the construction of synthetic air-void model

Sample No.	Mu	Sig	Distribution	Air content	Count
1	-0.7	0.5	Lognormal	0.1	32000
2	-0.7	0.5	Lognormal	0.07	32000
3	-0.7	0.5	Lognormal	0.05	32000
4	0.2	0.06	Normal	0.1	32000
5	0.2	0.06	Normal	0.07	32000
6	0.2	0.06	Normal	0.05	32000

6.1.2 Visualization of Spatial Air-Void Model

The synthetic air-void models are shown in Figure 32. The air voids with different radii are marked with different colors. It can be observed that most of the air voids in samples 1, 2, and 3 are purple, and few air voids are green and yellow. In samples 4, 5, and 6, most of the air voids are green, and a few air voids are green and yellow. The preliminary observation indicates that the distribution of the air voids in the constructed air-void models is consistent with the pre-designed distribution. Samples 1, 2, and 3 simulated the scenarios where both entrained and entrapped air voids are in the hardened concrete. Samples 4, 5, and 6 simulated the scenarios where only entrained air voids are in the hardened concrete.

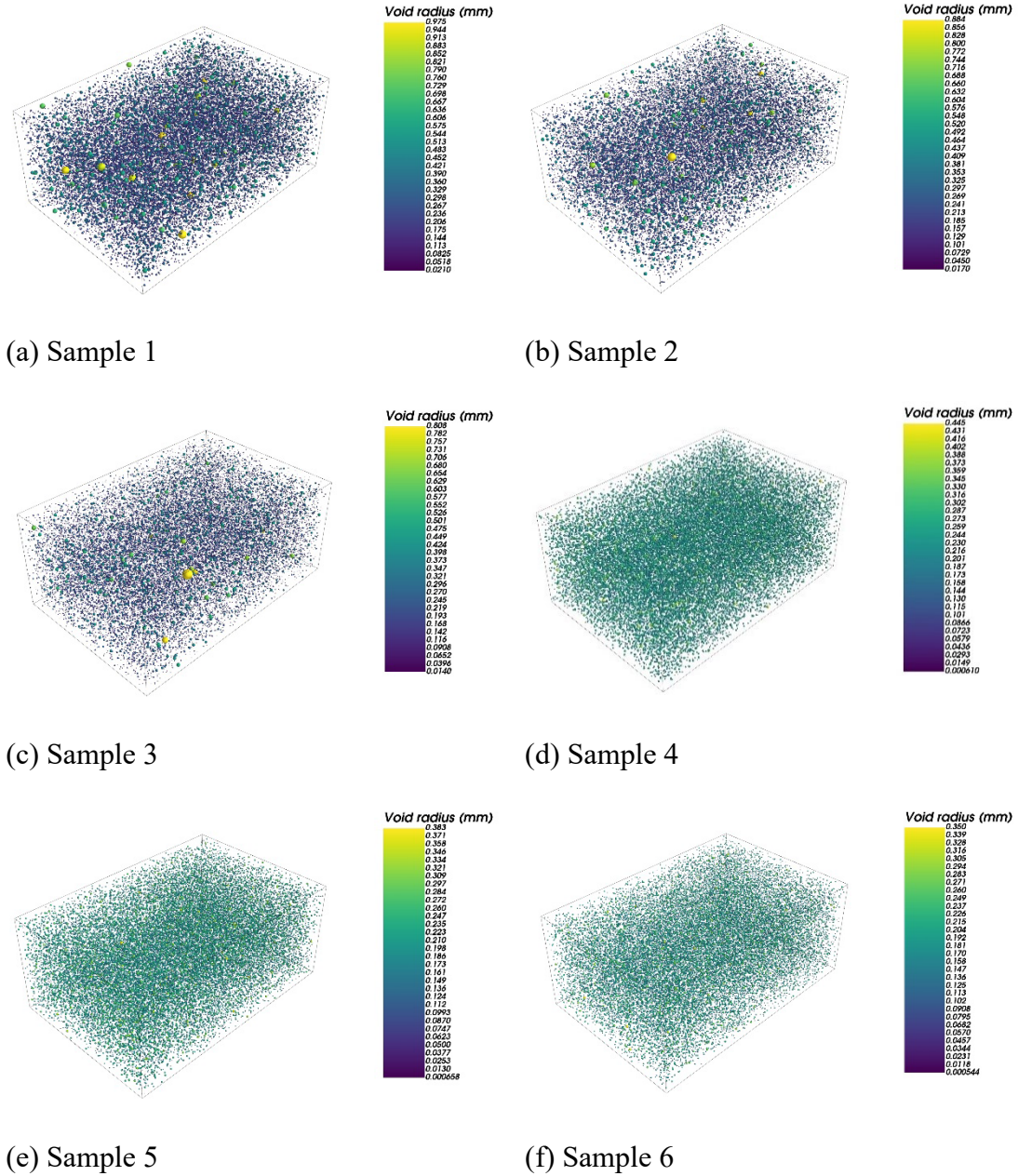
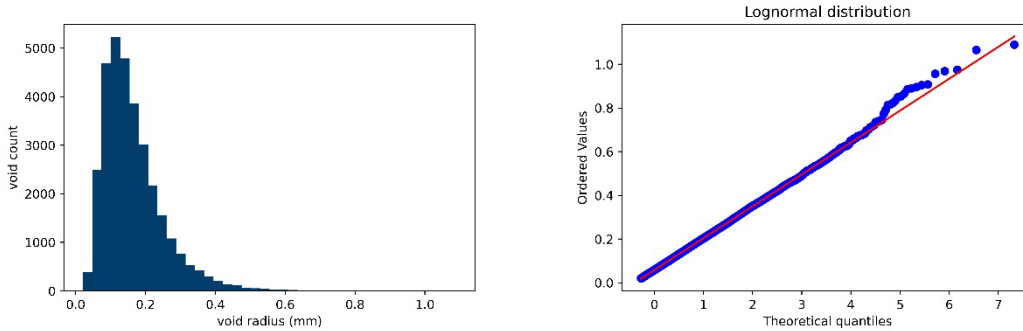


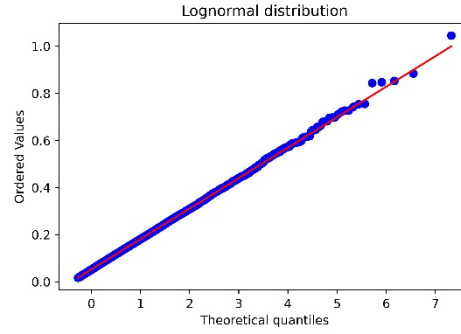
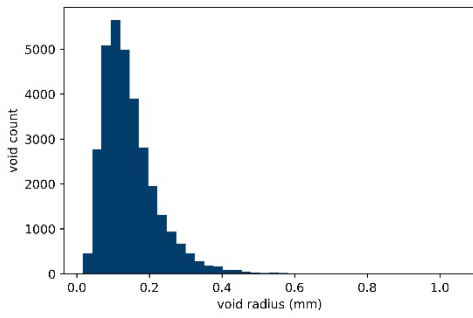
Figure 32. Visualization of the synthetic air-void model

The detailed distributions of void radius are extracted from the obtained synthetic air-void models. The probability density plot and probability plot of the air-void radius in different models are shown in Figure 33. The probability density plots present the density distribution of the air-void radius. The probability plots assess whether or not a data set

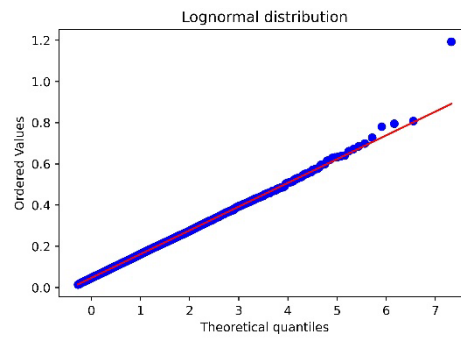
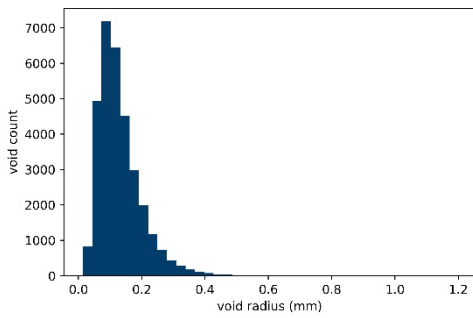
follows a given distribution. Theoretically, after the radius rescale operation (as shown in Figure 31), the lognormal distribution can be slightly changed. As shown in Figures 32(a), (b), and (c), most air voids in the air-void radius strictly follow a lognormal distribution, and only a few air voids at the tail of the distribution do not strictly follow a lognormal distribution. The radius of air voids in samples 1, 2, and 3 can be considered as a lognormal-like distribution. For the normal distribution, the radius rescaling operation does not change the distribution type. As shown in Figures 32(a), (b), and (c), the radius of air voids in samples 4, 5, and 6 can be considered as a normal-like distribution with a slight bias for some small air voids. The bias is caused during the random radius generation process (as shown in Figure 31). All the randomly generated air-void radii are changed into absolute values to avoid negative air-void radii. In conclusion, the generated air-void radius distribution in the synthetic air-void model satisfies the expectation.



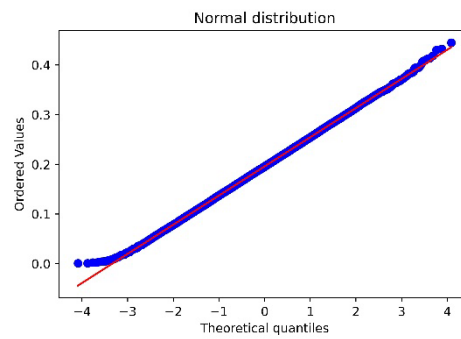
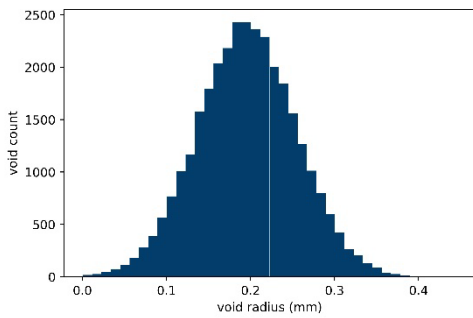
(a) Sample 1



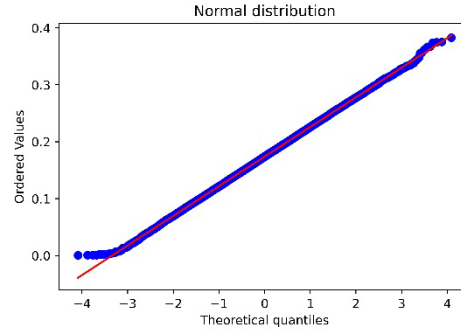
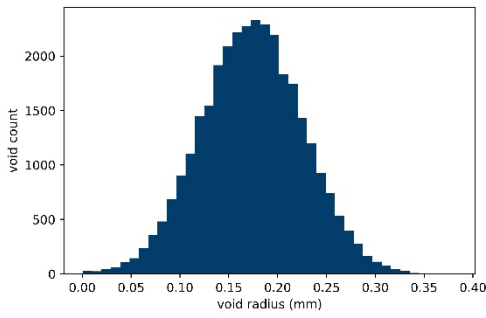
(b) Sample 2



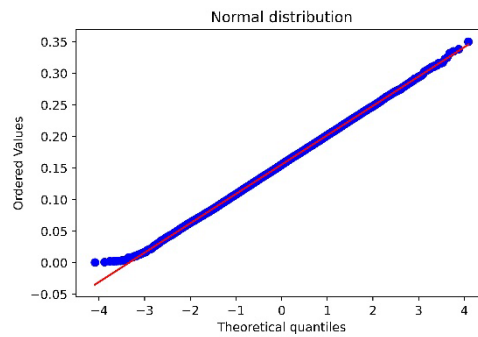
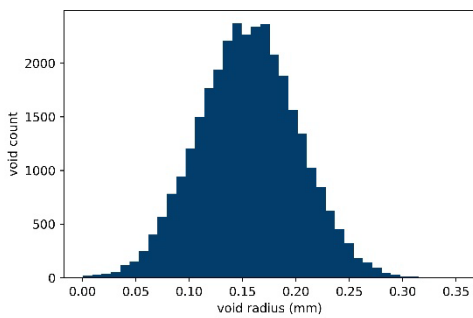
(c) Sample 3



(d) Sample 4



(e) Sample 5



(f) Sample 6

Figure 33. The distribution and probability plot of the air void count distribution in each synthetic air-void model

6.2. Evaluation of Influence Factors for 2D and 3D PPV Analysis

With advances in understanding the role of air voids in mitigating freeze-thawing damages, the reliability of spacing factor calculation using Powers' hypothesis has been debated in several research studies (Philleo 1983, Snyder 1998). Recently, a PPV method, originally proposed by Larson et al., was studied for the petrographic analysis of the air-void system (Larson et al. 1967). The PPV analysis assumes that each air void protects a certain range of paste from being damaged by freeze-thawing effects. During the PPV analysis process, a certain protection range will be assigned to each air void to simulate

the protection effect generated by the air-void system. Then, the freeze-thawing performance of concrete specimens can be estimated using the percentage of paste protected by the air-void system. The PPV analysis better represents the actual air-void system compared with the Power's method. And also, the evaluation parameter calculated using the PPV analysis better correlated with the concrete freeze-thaw performance (Larson et al. 1967, Song et al. 2021). However, one limitation of the up-to-date PPV analysis is that it only experiments with a single 2D surface plane of a polished concrete specimen, which can be restricted by the limited information that can be provided by 2D analysis.

To investigate the limitation of the 2D PPV analysis, a simulation analysis was conducted. As shown in Figure 34, a surface plane was randomly generated in the synthetic air-void model. All the involved air voids were marked with a protection range - shown in a transparent coat form, as visualized in Figure 34. The involved air voids include in-section and out-section two types of air voids. The air voids marked in red are in-section air voids that directly intersected with the generated surface plane. The air voids marked in blue are out-section air voids that do not intersect with the generated surface plane directly, instead, their protection range intersects with the generated surface plane. In the simulation, the protection range is set as 200 μm which is in accordance with the minimum spacing factor specified by American Concrete Institute (Hill et al. 2008). Based on the observation of in-section and out-section air voids presented in Figure 34, a significant amount of concrete surfaces can be protected by out-section air voids which cannot be observed through the polished hardened concrete surface. Therefore, 2D PPV analysis will often lead to an underestimation of paste protection due

to the fact that it by nature overlooks the effects of out-section air voids. To accurately estimate the level of actual paste protection, the 3D distribution information of out-section air voids is needed.

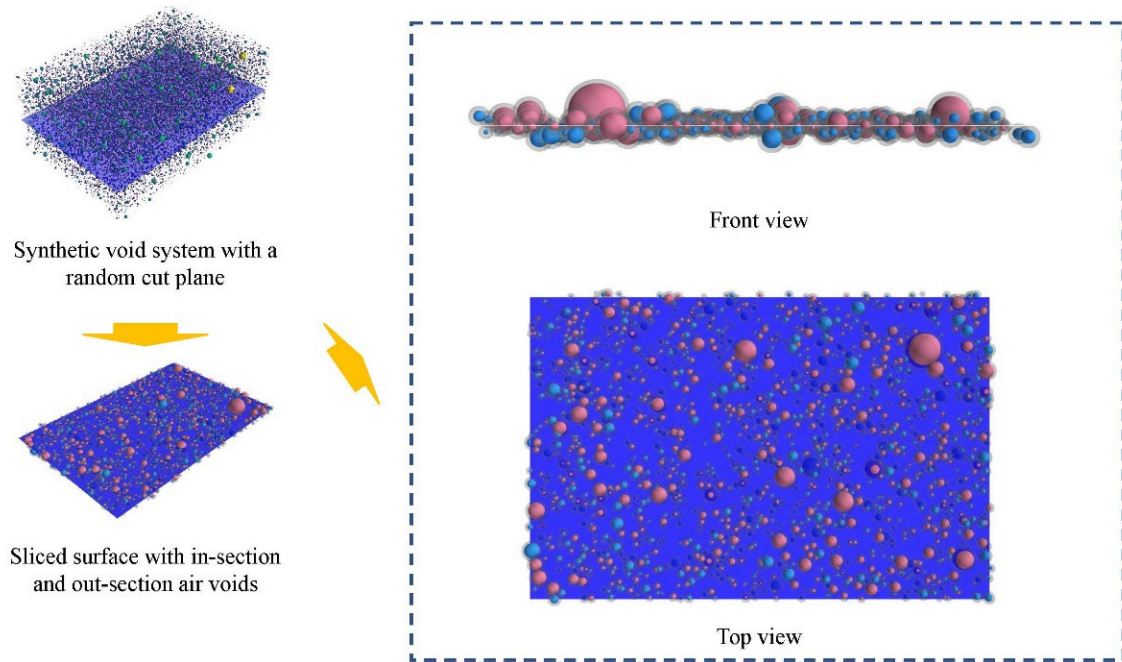
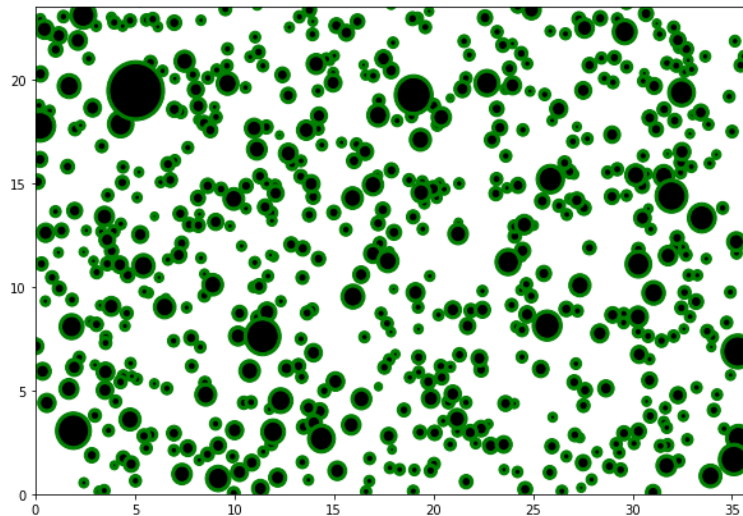


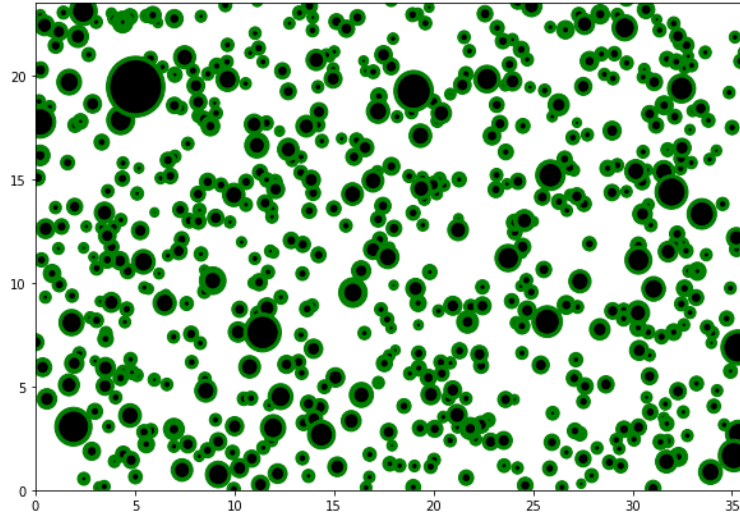
Figure 34. Diagram for the in-section and out-section air voids intersected with a concrete plane

To better understand the protective effect of both in-section and out-section air voids, the protection range and air voids were mapped from 3D space to a 2D concrete surface plane. As shown in Figure 35, the mapped air voids are shown in black color, the protection ranges generated by in-section air voids are shown in green color, and the protection ranges generated by out-section air voids are shown in yellow color. Figure 35(a) presents the protection range estimated using the in-section air voids observed through the 2D air-void intersections. Due to the lack of spatial and size information that can be used to restore the actual air-void location in 3D space, the 200- μm protection

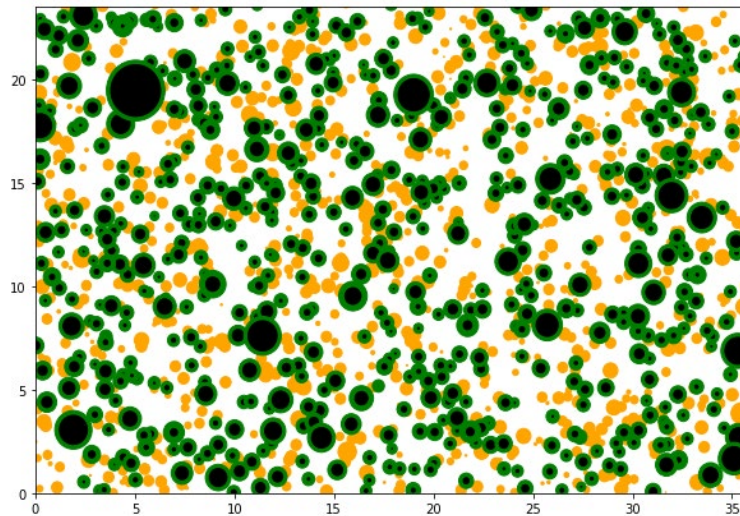
range was directly used as a protection range for each 2D air-void intersection. However, based on the observation of Figure 35(b), the 200- μm protection range from 3D air voids can also generate a protection range on a 2D concrete plane larger than 200 μm . This is caused by the 3D and 2D surface projection effects. Therefore, directly using the protection range to approximate the projected protective effect on 2D concrete surfaces can result in an underestimation of the overall paste protection. Figure 35(c) presents the projected protection range estimated using both in-section and out-section air voids from the synthetic 3D air-void space. It is obvious that the out-section air voids can provide a comparable amount of protection to the concrete specimen surface compared with the in-section air voids. Hence, the spatial information of in-section and out-section air voids are critical for the accurate PPV analysis.



(a) PPV analysis using in-section air voids observed in the 2D concrete section



(b) PPV analysis using in-section air voids observed in 3D space



(c) PPV analysis using both in-section and out-section air voids observed in 3D space

Figure 35. PPV analysis using the air-void information from 2D and 3D perspective

6.3. Accuracy Assessment

An appropriate assessment method is vital to evaluate the accuracy of the unfolding 3D air-void distribution. As shown in Figure 36, the measurement of the difference

between two different continuous distributions can be accomplished by integrating the regions that do not coincide with each other. As mentioned earlier, the Saltykov method generates a discrete 3D air-void size distribution. The upper boundary of each bin is considered as the radius of all the restored air voids in the bin class. The number of the restored air voids in each bin class can be represented as a set X_R .

$$X_R = (X_{R1}, X_{R2}, X_{R3}, \dots, X_{Rj}) \quad (28)$$

The number of the actual air voids in each bin class can be represented as a set Y_R .

$$Y_R = (Y_{R1}, Y_{R2}, Y_{R3}, \dots, Y_{Rj}) \quad (29)$$

Consequently, the difference between the restored 3D air voids and the actual 3D air voids can be evaluated through a similarity measurement. In this research study, the Minkowski Distance d is adopted for similarity measurement. The Minkowski Distance of order p (where p is an integer) between X_R and Y_R is defined as:

$$d(X_R, Y_R) = \left(\sum_{i=1}^j |X_{Ri} - Y_{Ri}|^p \right)^{\frac{1}{p}} \quad (30)$$

Considering both X_{Ri} and Y_{Ri} are one-dimensional variables, the Minkowski Distance used to measure the similarity of the probability density function of X_{Ri} and Y_{Ri} can be simplified as:

$$d_{density}(X_R, Y_R) = \frac{(\sum_{i=1}^j |X_{Ri} - Y_{Ri}|)}{\sum_{i=1}^j Y_{Ri}} \times 100\% \quad (31)$$

In this study, Equation (31) is utilized for the calculation of the accuracy of the unfolded in-section and out-section 3D air-void radius using Saltykov method.

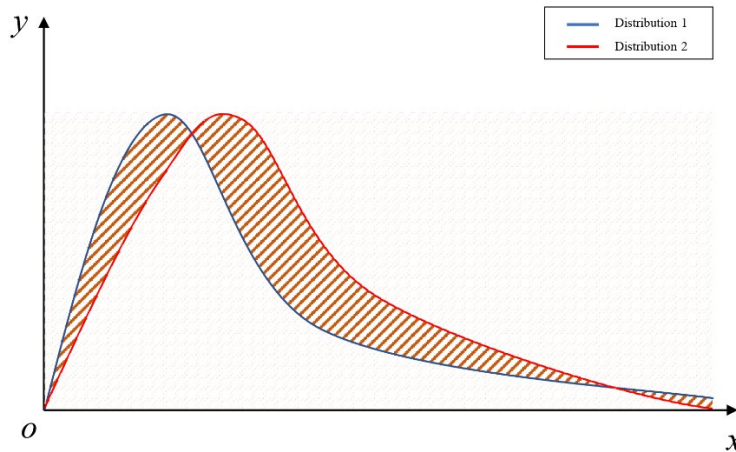


Figure 36. Diagram of difference between two distributions

6.4. Results and Analysis

As a statistic method, the Saltykov method is sensitive to many factors such as the number of observed 2D air-void intersections and the number of bin classes. All these factors can impact the accuracy of unfolding accuracy using the Saltykov method. However, limited research efforts have been paid to analyze the effect of those factors on unfolding an air-void system. Currently, as reported in the research by Fonseca et al., the selection of related parameters for the Saltykov method is solely dependent on trial and error using 2D air-void analysis results (Fonseca and Scherer 2015). Hence, it is important to further explore the relationship between these influence factors and the unfolding accuracy and provide experiences for 2D to 3D air-void unfolding using the Saltykov method.

To simulate the concrete surface plane that intersected with a various number of air voids, the most straightforward method is to construct as many synthetic concrete

samples with different sizes and void counts as possible. However, building the synthetic air-void system is time-consuming. Specifically, varies with the air content, void size, and void count, the construction process for one synthetic model can take up to 15 hours to be finished. The air void overlap detection and reallocation are the two major steps that account for most of the modeling time. By nature, the value of air content and void size of hardened concrete are relatively small. Hence, the air voids in hardened concrete can be considered as a loosely packed void system. As a result, it takes less time for an overlapped air void to be reallocated in a free area. That is to say, the void count is the most significant factor that affect the computation cost because the overlap detection process for each air void requires the traversal of all the other air voids. It makes the computation cost increase exponentially. To overcome this problem, an equally effective way to explore the relationship between the number of observed air-void intersections and unfolding error is to generate more random slices from the same synthetic air-void model. The air-void intersections observed from different slices can be appended together to simulate the situation in which different numbers of air voids are observed. A diagram as shown in Figure 37 illustrates this procedure.

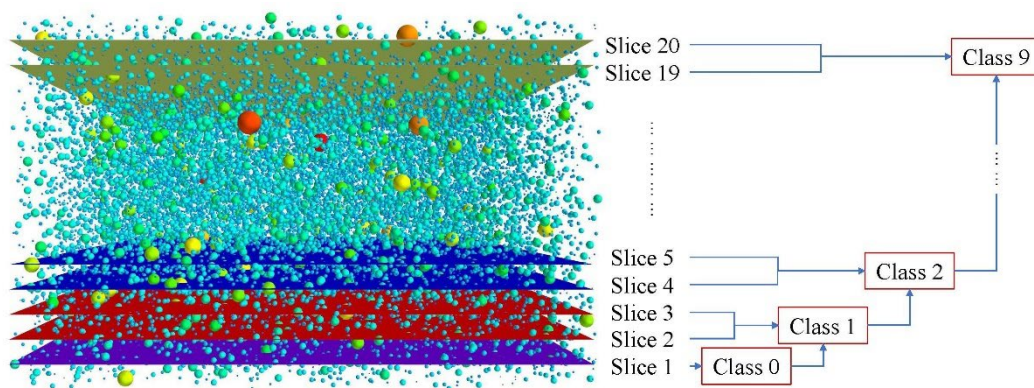


Figure 37. Diagram for appending air-void intersections from different slices

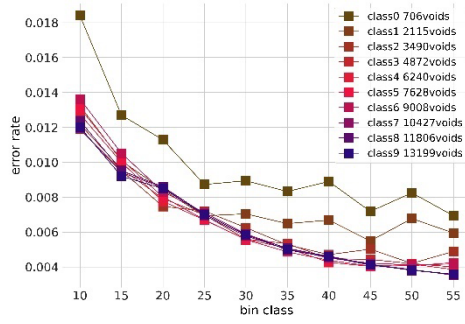
6.4.1 In-Section Air Voids

The in-section air voids, which are directly intersected with the concrete surface, are analyzed first. Figure 38 presents the unfolding accuracy of each synthetic air-void model with the different number of bin classes and air-void observations. As the number of bin classes increases, a decreasing trend can be observed for the unfolding bias, and the decreasing rate slowed down gradually. It indicates that a larger number of bin classes helps the Saltykov method to achieve better unfolding accuracy. And also, as the number of bins exceeds a specific threshold, the benefit of increasing it weakened. The bias curve in Figure 38 presents the frequency differences between unfolded air voids and actual air voids which are intersected with the concrete surface plane. Generally, the up boundary of each bin class is used to approximate the unfolded air void radius in a specific range. The radius of the unfolded air voids can be more precisely presented in situations where a large number of bin classes is used. Therefore, the benefits of using a large bin number for the Saltykov method are twofold. One is for the improvement of the unfolding accuracy measured by frequency bias. The other one is for the improvement of radius approximation.

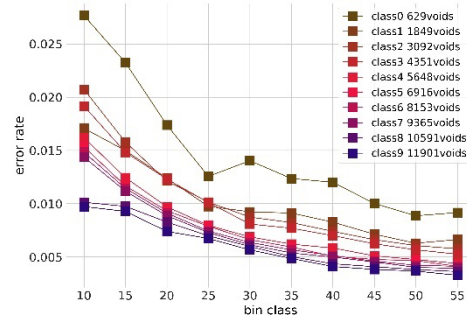
For the error curve with limited air-void observations, fluctuations can be observed. The same phenomenon was also observed in the research by Song et al. and was explained by the periodicity of the round-off error (Song et al. 2021). The round-off error is caused by the negative void count unfolded by the Saltykov method from a smaller bin class when the number of observed air voids in a bin is lower than its expected value (Sahagian and Prousevitich 1998). This phenomenon indicates that the benefit of increasing bin number is tenable only when enough air voids are being observed.

Moreover, the type of distribution of air voids can also affect the unfolding accuracy. As shown in Figure 38, compared with the bias curve generated from the synthetic model with normal-like void distributions, the unfolding results of the synthetic model with lognormal-like distributions are more sensitive to the number of bin classes. And also, more fluctuations can be observed in the bias curve from the normal-like void model.

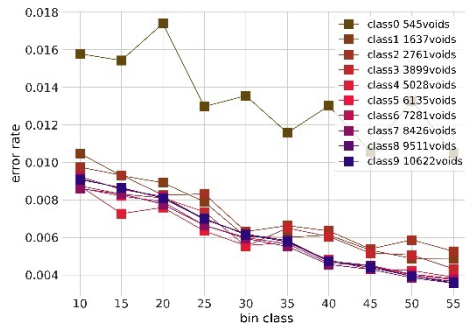
In this research, the error rates for all the estimated air-void radius unfolded with 55 bin classes and with over 10,000 void observations are lower than 0.5%. Even in the case where lower than 1,000 air voids were observed and 10 bin classes were adopted, most of the overall error rates for the unfolded air-void distribution are lower than 3.5%. Both 0.5% and 3.5% can be considered as low error rates. The error rate as mentioned in the previous section was calculated by treating air voids with different radii the same, that is to say, all the air voids with different radii were simply added up to get the final error rate. However, in fact, the air voids with different radii have different influences on the protection of concrete paste. The air voids with small radii are more important for concrete freeze-thaw performance. Therefore, it is also important to investigate the unfolding results for the air voids with different radii.



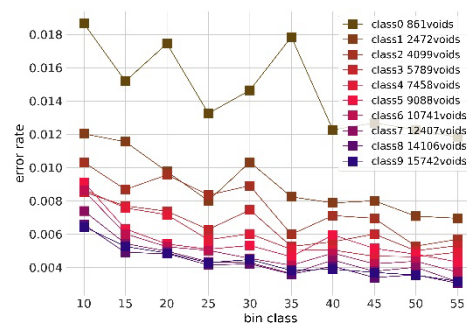
(a) Sample 1



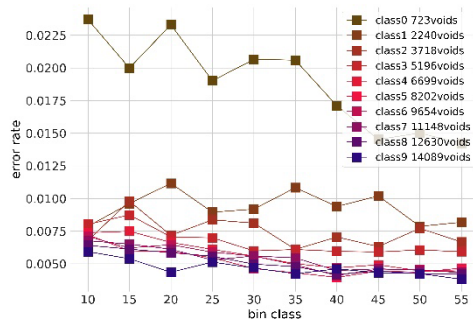
(b) Sample 2



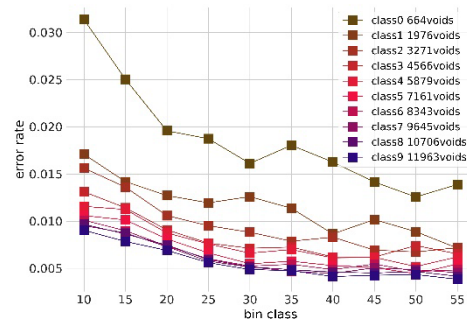
(c) Sample 3



(d) Sample 4



(e) Sample 5

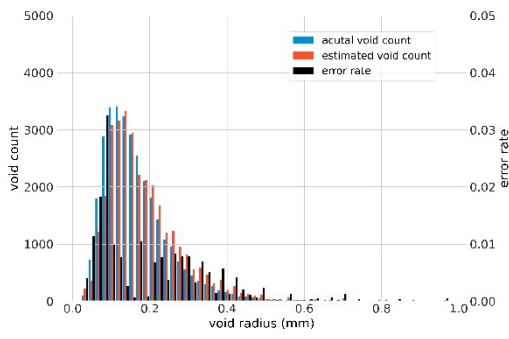


(f) Sample 6

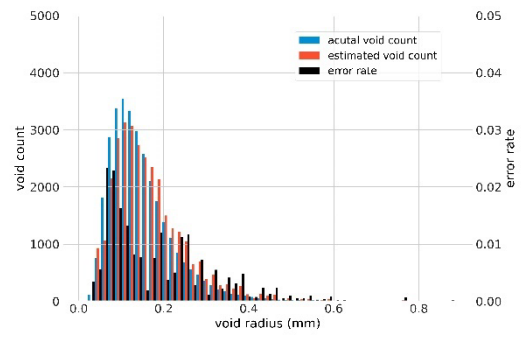
Figure 38. Unfolding error rate with different air-void observations and bin classes

Figure 39 presents the unfolding results and corresponding error rate for each bin class. The unfolding results are generated using the ‘class 9’ void intersection data of

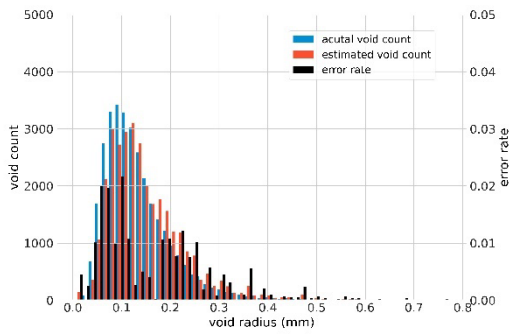
each synthetic void model with 55 bin classes. As shown in Figures 38(a), (b), and (c), it is obvious that the air voids with smaller radii have a higher error rate. For the large air voids, the error rate is close to 0. Therefore, the small air voids contribute to most of the unfolding error. As a result, the actual error rate between the actual freeze-thawing performance of hardened concrete and the freeze-thawing performance estimated using the unfolded air voids should be higher than the observed unfolding error. For the biased error rate distribution, one possible explanation is that not enough bin classes are used to represent a concentration of small radii air voids. This phenomenon further corroborated the conclusion drawn from Figure 38, that is, the number of bin classes used for the Saltykov method is critical to unfolding accuracy. In short, concentrated air voids represented by few bin classes are undesired. For example, in Figure 39(a), even 55 bin classes are utilized during the unfolding process, only 10 bin classes are located between $0\mu\text{m}$ and $0.2\mu\text{m}$ radius to represent more than 50% air voids, and 45 bin classes are used to represent the rest of 50% air voids. The same phenomenon can also be observed in Figures 38(d), (e), and (f) where the distribution of air voids is more evenly, the variance of unfolding error between different bin classes becomes lower than the variance of unfolding error in Figures 38(a), (b), and (c).



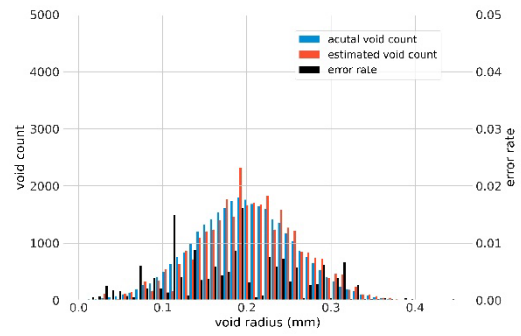
(a) Sample 1



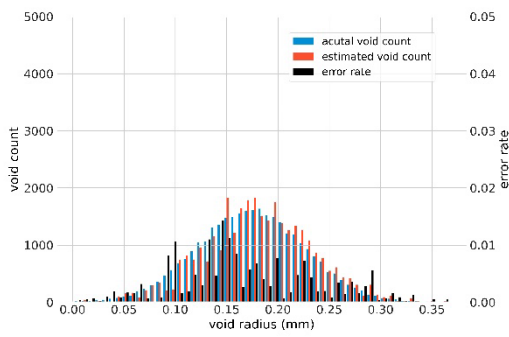
(b) Sample 2



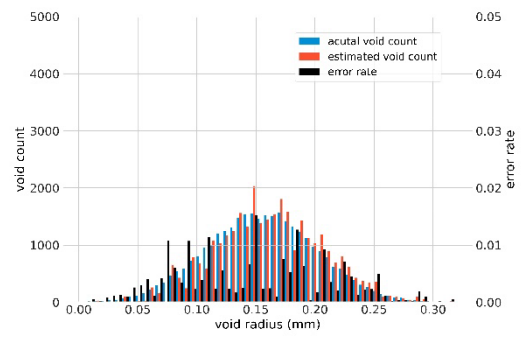
(c) Sample 3



(d) Sample 4



(e) Sample 5

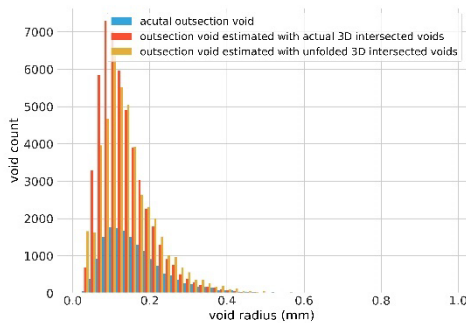


(f) Sample 6

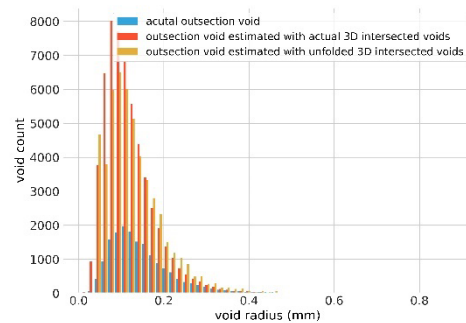
Figure 39. Comparison of actual void distribution and unfolding results

6.4.2 Out-Section Air Voids

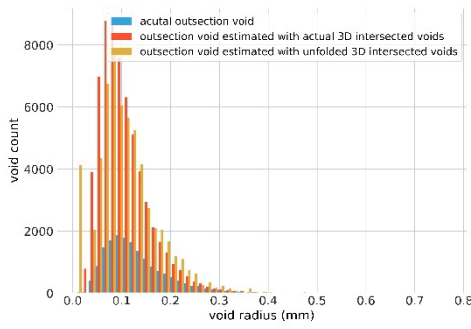
Given in-section air voids distribution, the out-section air voids can be calculated using Equation (20). In this study, out-section air-void radius distributions are calculated based on two different in-section air void distributions: the void radius distribution obtained directly from the cutting plane (served as the control group) and the unfolded air voids. In this way, the effect of the unfolding error of in-section air voids on the restoration of out-section air-void radius distribution can be evaluated. As shown in Figure 40, no significant difference can be observed between the out-section air voids calculated from the actual in-section air voids and the unfolded in-section air voids. It means the effects of unfolding error of in-section air voids on the out-section air voids calculation is not significant. However, there is a significant difference between the actual out-section air voids and the unfolded out-section air voids. The number of unfolded out-section air voids is significantly higher than the number of actual out-section air voids. Therefore, if Equation (20) is utilized to restore the actual air void distribution for PPV analysis, there is no doubt that the freeze-thawing performance of hardened concrete can be greatly overestimated.



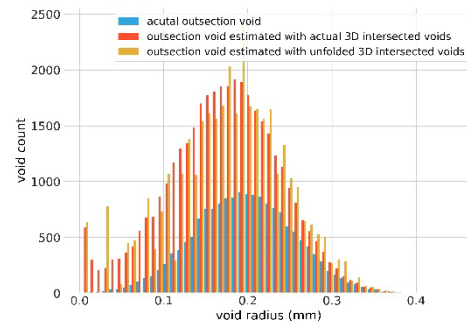
(a) Sample 1



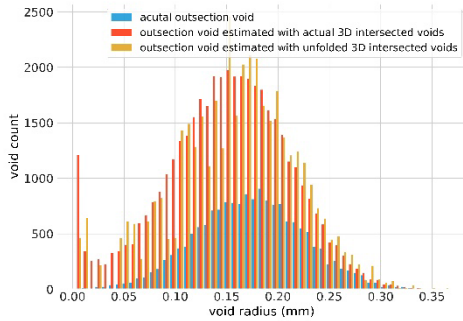
(b) Sample 2



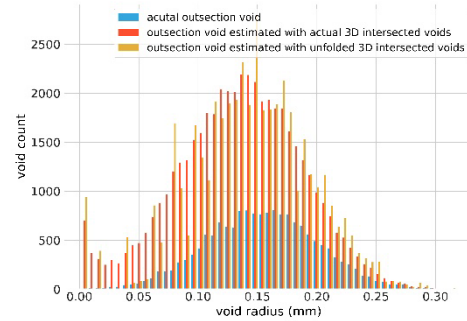
(c) Sample 3



(d) Sample 4



(e) Sample 5

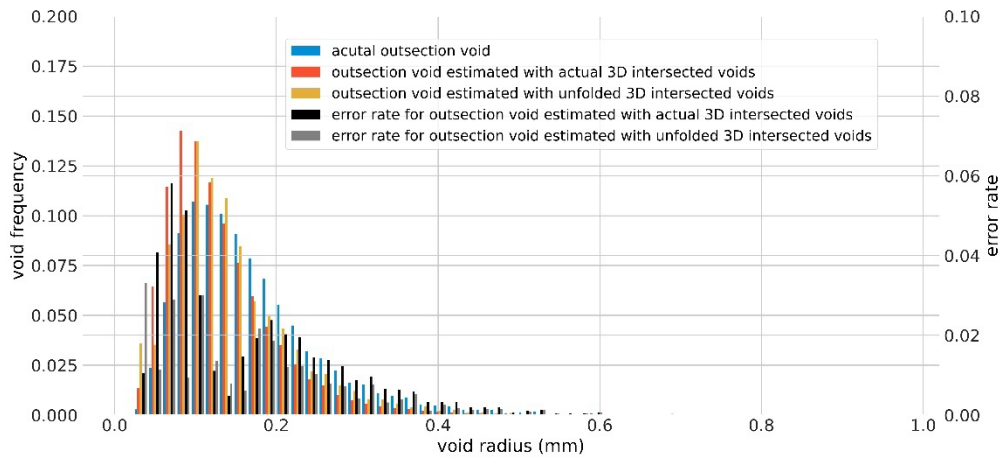


(f) Sample 6

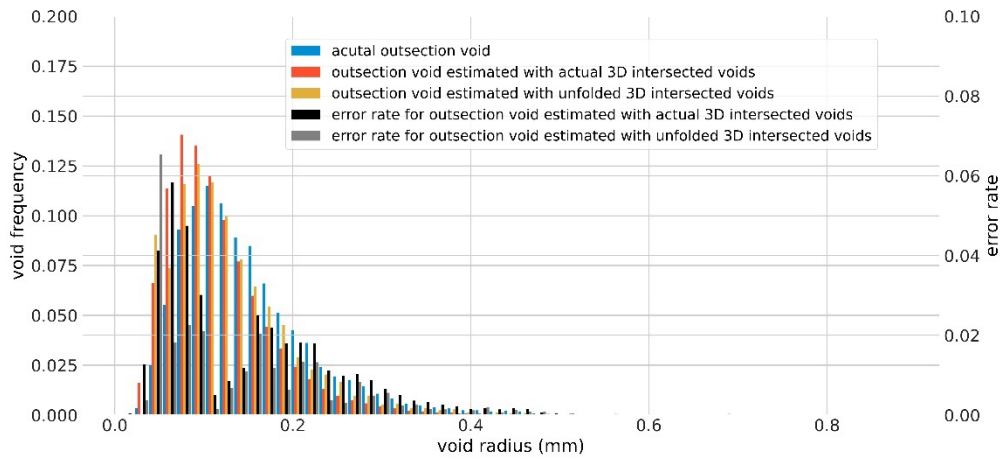
Figure 40. Unfolding results for out-section air voids

Figure 41 presents the histograms of the unfolding results of out-section air. As shown in Figure 41, the distribution pattern of the error rate is very similar to the error rate of the unfolded in-section air voids. However, one significantly higher error rate is observed. It indicates that the unfolding error for in-section air voids can be enlarged when calculating the out-section air voids. While the overall error rate is still within an acceptable level, it is worth mentioning that the frequency of out-section air voids cannot be directly utilized for the restoration of spatial air-void distribution due to the lack of a reference system. Different from the in-section air voids which can be observed through

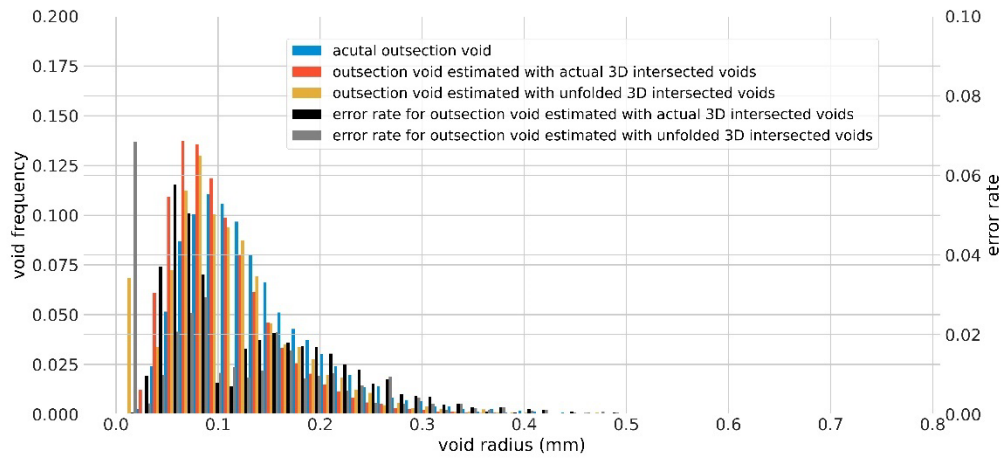
air-void intersections, there are no intersections that can be used as a reference for out-section air voids. As a result, the number of out-section air voids cannot be inferred using the air-void intersections and restored using the frequency value. Therefore, according to the experiment results, even the difference between the frequency value of unfolded air voids and the frequency value of actual air voids is not big, the out-section air voids cannot be accurately unfolded.



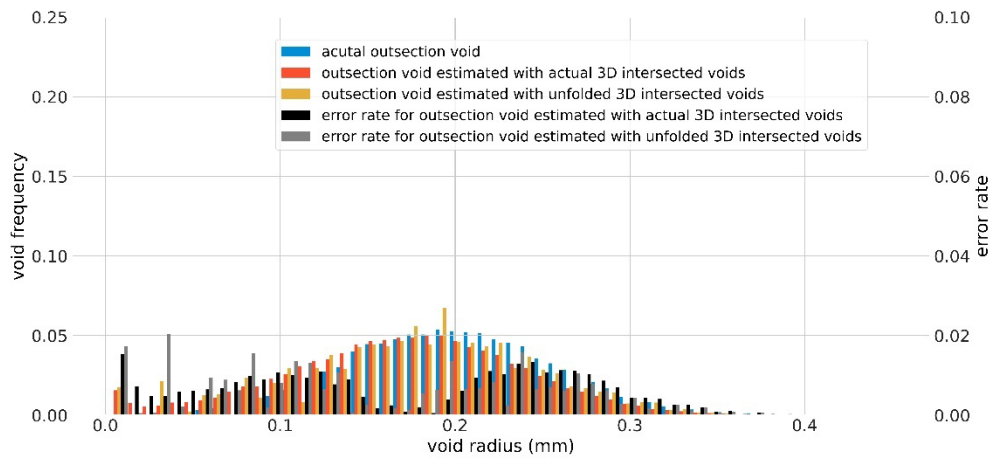
(a) Sample 1



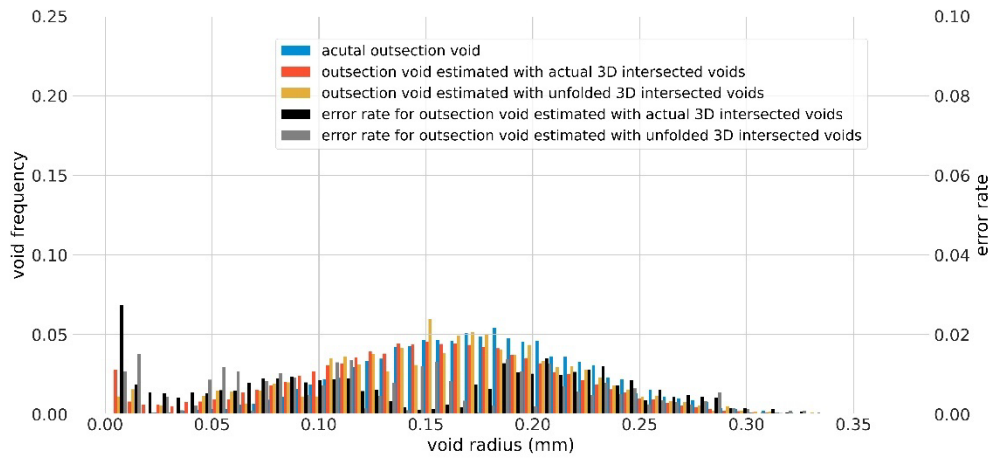
(b) Sample 2



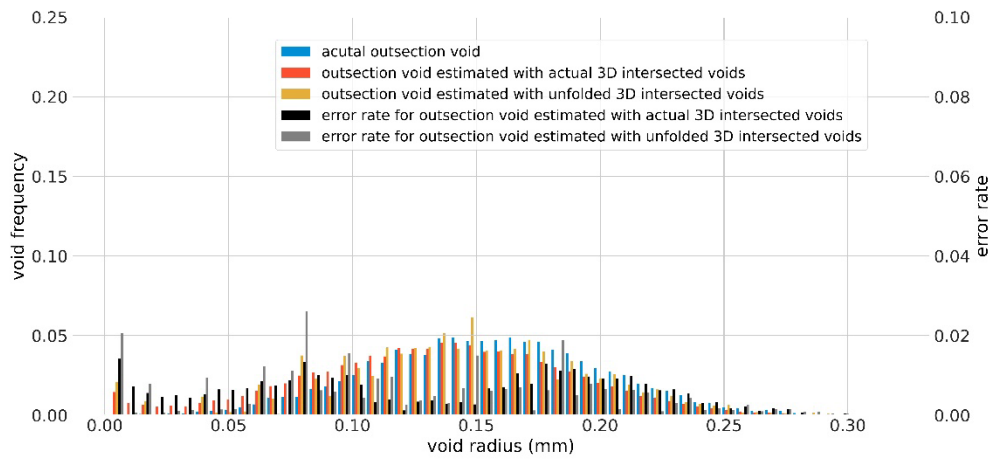
(c) Sample 3



(d) Sample 4



(e) Sample 5



(f) Sample 6

Figure 41. Unfolding results for out-section air voids with error rate

Simply put, even the radius of in-section air voids can be estimated using the Saltykov method with a relatively satisfying result, the inaccurate unfolding results for out-section air voids can significantly affect the restored spatial air-void system.

6.5 Summary

In this chapter, the feasibility of using the Saltykov method for restoring 3D air-void radius was investigated using a set of synthetic air-void models. The Saltykov method can be used for the accurate unfolding of in-section air voids. And the overall accuracy of the unfolded in-section void distribution can be quite reliable when a large number of air voids are observed from a hardened concrete surface. For the out-section air voids, even its probability density distribution can be estimated with acceptable accuracy, due to the lack of a reference for the number of intersected out-section air voids, the number of out-section air voids for each radius bin class cannot be restored. Consequently, the Saltykov method can be used to estimate the actual air-void radius distribution using 2D void intersections, while significant refinements are still required by the Saltykov method to satisfy the requirements for PPV analysis. The other research findings are described below:

(1). The PPV analysis that is solely based on the air-void information from 2D air-void intersections can generate an underestimated protection estimation. The size information of both in-section and out-section air voids is important for accurate PPV analysis.

(2). The insufficient number of 2D air-void intersections used for 3D air-void radius restoration can lead to a higher error rate and round-off errors. There is a minimum air-void observation that is required by the Saltykov method to achieve a satisfactory unfolding result. The required minimum air-void observation can be changed according to the void radius distribution type.

(3). The number of bin classes utilized for the Saltykov method has a positive effect on the unfolding accuracy. However, due to the nonuniform distribution nature of the air-void radius and the uniform binning strategy, a large percentage of air voids is represented by a small percentage of bin classes. The portion of the air voids, which is insufficiently represented by the limited number of bin classes, can result in a higher unfolding error rate.

(4). The number of out-section air voids cannot be accurately estimated using the state-of-the-art method. Significant biases can be observed.

7. CONCLUSIONS

7.1 Summary of Observations

In this research, the feasibility of using three-dimensional (3D) reconstruction methods to automatically contrast the air voids in hardened concrete surfaces was investigated first. Then, a series of artificial intelligence-based image processing methods (conventional image processing methods and convolution neural networks) were introduced for the segmentation of air voids in 3D concrete surface images. Finally, the reliability of using the Saltykov method to restore the 3D air-void radius was evaluated. The key conclusions are as follows:

(1). Compared with the Sparse Bayesian Regression method (SBL) and the Low-rank minimization method, the Basic photometric stereo method shows a good performance with good 3D reconstruction accuracy and acceptable computation cost. A photometric stereo method that incorporates the image corruption into the surface normal calculation with an acceptable computation cost could improve the accuracy of air-void segmentation.

(2). Transparent aggregates, dark aggregates, and voids in aggregates can be contrasted in the surface normal image and generate air-void like patterns. These air-void like patterns can be hardly differentiated using the conventional image processing technique methods. However, the convolution neural networks are able to generate highly abstract features to accurately distinguish the air voids from most of these air-void like patterns. The air-void like patterns that are generated by fine aggregates has the most significant impact on the segmentation results and measurement of air-void system. The experimental results showed that the deep convolutional neural networks (DCNN) could

accurately distinguish air voids from hardened concrete images with the detection accuracy of over 0.9 in only less than a minute. The accuracy rates for air content, specific surface, and spacing factor were 0.92, 0.91, and 0.89, respectively.

(3). The photometric stereo method provides a feasible way to automatically contrast the air voids from the hardened concrete surface. Shapes and gradient variations of air voids in the surface normal images are two important features can be utilized for air-void segmentation. The appearance of air voids in surface normal images can vary. Some deep air voids can generate a significantly different appearance in the surface normal images, which could greatly harm the segmentation results. Increasing the number of training data that contains deep air voids or refining the illumination angle of the photometric stereo system can help improve the segmentation results of deep air voids.

(4). The Mean of Intersection over Union (MIoU), which is the accuracy measurement metric utilized in this research for the training and evaluation of convolution neural networks, does not positively correlate with the accuracy of the air-void parameters measurements. The MIoU measures the overall performance of the convolution neural networks to segment all the air voids in concrete surface normal image. The air voids with different radius share the same weight while calculating the MIoU. However, the air-void parameters like spacing factor and specific surface care more about the fine air voids. The adoption of MIoU as an accuracy measurement metric may not help the convolution neural networks to converge at the optimum point for air-void parameters measurement.

(5). The Saltykov method can be utilized to restore the 3D in-section air void radius using the air-void intersection information with a good accuracy. Both the number of air-

void observations and bin classes can affect the accuracy of the Saltykov method. The larger the number of air-void observations and bin classes, the higher the accuracy. However, due to the nonuniformity of the air-void radius distribution, the small percentage of bin classes are utilized to represent the most air voids, which impact the unfolding accuracy for those densely distributed air voids.

7.2 Innovations

(1). Innovatively introduced 3D reconstruction techniques to automatically contrast the air voids in hardened concrete surfaces without contrast enhancement operation. A photometric stereo system was developed to automatically capture the concrete surface images under various illumination directions. The contrast process for a hardened concrete sample with a size of 3.58 cm × 2.38 cm takes only 10-15 seconds to accomplish.

(2). Explored the reliability of segmenting the air voids in surface normal images using conventional image processing techniques. A predefined threshold is required for accurate air-void segmentation. The subjectively determined threshold can impact the generalizability of the air-void segmentation results using conventional image processing techniques.

(3). Innovatively proposed an automated air-void segmentation method using deep learning method. In this research, U-Net was adopted for the segmentation of air voids in hardened concrete surfaces. The proposed air-void segmentation method takes 15-20 seconds to segment all the air voids in a hardened concrete sample with a size of 3.58 cm × 2.38 cm with a detection accuracy of over 0.9.

(4). An image dataset with more than 10,000 original hardened concrete surface images, concrete surface normal images, and pixel-level air-void annotations was developed. The dataset provides a basis for exploring artificial intelligence methods in automated air-void segmentation.

(5). A set of synthetic air-void models were constructed to validate the reliability of the Saltykov method for 3D air-void radius restoration. The experiment results also provide insight into the error pattern while the Saltykov method is used for 3D air-void radius restoration.

7.3 Future Works

Several useful directions for further research can be:

(1). The basic photometric stereo, SBL, and Low-rank minimization methods were investigated in 3D concrete surface reconstruction. There are other advanced photometric stereo methods that can be utilized to reconstruct the non-Lambertian concrete surfaces. In the future, the feasibility of using other advanced photometric stereo methods to reduce the noises in surface normal images can be studied.

(2). In this research, only the air voids in hardened concrete surfaces were segmented. As specified in ASTM C457, aggregates and cement paste are also required for the calculation of air-void parameters. One useful direction for further research can be to segment all the components in hardened concrete surfaces using RGB-D (Red, Green, Blue, and Depth) images.

(3). The research investigated the reliability and error patterns of the Saltykov method, which provides a basis for the improvement of the Saltykov method. In the

future, optimized binning strategies can be proposed to reduce the error rate.

(4). The applicability of the proposed air-void segmentation method on hardened concrete samples with different mix designs should be further investigated. In this study, the proposed method was tested on limited types of mix-designed samples, but the selected samples may not represent the features of all hardened concrete samples, such as porous concrete and hardened concrete with silica fume. In the future, more diverse hardened concrete samples will be tested to analyze the applicability of the proposed air-void segmentation method.

REFERENCES

- Aboufoul, M., Chiarelli, A., Triguero, I. & Garcia, A., 2019. Virtual porous materials to predict the air void topology and hydraulic conductivity of asphalt roads. *Powder Technology*, 352, 294-304.
- Adkins, D.F. & Christiansen, V.T., 1989. Freeze-thaw deterioration of concrete pavements. *Journal of Materials in Civil Engineering*, 1 (2), 97-104.
- Anon, <https://pdhonline.com/courses/s177/s177content.pdf> [online].
- Astm, 2012. Standard test method for microscopical determination of parameters of the air-void system in hardened concrete: C 457/c 457m-12. ASTM.
- Attigbo, E.K., 1993. Mean spacing of air voids in hardened concrete. *Materials Journal*, 90 (2), 174-181.
- Baumgart, C., Blair, R. & Linder, K., 2006. *Tpf-5(014) image analysis of hardened concrete*. Kansas City, Missouri: Administration, F.H., 00KCP1087.
- Bernardes, E.E., Carrasco, E.V.M., Vasconcelos, W.L. & De Magalhães, A.G., 2015. X-ray microtomography (μ -ct) to analyze the pore structure of a portland cement composite based on the selection of different regions of interest. *Construction Building Materials*, 95, 703-709.
- Bernotas, G., Scorza, L.C., Hansen, M.F., Hales, I.J., Halliday, K.J., Smith, L.N., Smith, M.L. & McCormick, A.J., 2019. A photometric stereo-based 3d imaging system using computer vision and deep learning for tracking plant growth. *GigaScience*, 8 (5), giz056.

- Besl, P.J. & McKay, N.D., 1992. Method for registration of 3-d shaped. *Sensor fusion IV: control paradigms and data structures* International Society for Optics and Photonics, 586-606.
- Bianco, G., Gallo, A., Bruno, F. & Muzzupappa, M., 2013. A comparative analysis between active and passive techniques for underwater 3d reconstruction of close-range objects. *Sensors*, 13 (8), 11007-11031.
- Biskup, B., Scharr, H., Schurr, U. & Rascher, U., 2007. A stereo imaging system for measuring structural parameters of plant canopies. *PLANT CELL AND ENVIRONMENT*, 30 (10), 1299-1308.
- Boshoff, W.P., 2019. A review of x-ray computed tomography of concrete and asphalt construction materials. *Construction Building Materials*, 199, 637-651.
- Burgess, A.J., Retkute, R., Pound, M.P., Mayes, S. & Murchie, E.H., 2017. Image-based 3d canopy reconstruction to determine potential productivity in complex multi-species crop systems. *Annals of botany*, 119 (4), 517-532.
- Buslaev, A., Seferbekov, S., Iglovikov, V. & Shvets, A., 2018. Fully convolutional network for automatic road extraction from satellite imagery. *Proceedings of the IEEE Conference on Computer Vision and Pattern Recognition Workshops*, 207-210.
- Chang, S.W. & Liao, S.W., 2019. Kunet: Microscopy image segmentation with deep unet based convolutional networks. *2019 IEEE International Conference on Systems, Man and Cybernetics (SMC)* IEEE, 3561-3566.
- Chatterji, S., 2003. Freezing of air-entrained cement-based materials and specific actions of air-entraining agents. *Cement Concrete Composites*, 25 (7), 759-765.

- Chatterji, S. & Gudmundsson, H., 1977. Characterization of entrained air bubble systems in concretes by means of an image analysing microscope. *Cement concrete research*, 7 (4), 423-428.
- Chen, L.-C., Papandreou, G., Kokkinos, I., Murphy, K. & Yuille, A.L., 2014. Semantic image segmentation with deep convolutional nets and fully connected crfsd. *arXiv preprint arXiv:*.
- Chen, L.-C., Papandreou, G., Kokkinos, I., Murphy, K. & Yuille, A.L., 2017. Deeplab: Semantic image segmentation with deep convolutional nets, atrous convolution, and fully connected crfs. *IEEE transactions on pattern analysis machine intelligence*, 40 (4), 834-848.
- Cordts, M., Omran, M., Ramos, S., Rehfeld, T., Enzweiler, M., Benenson, R., Franke, U., Roth, S. & Schiele, B., 2016. The cityscapes dataset for semantic urban scene understanding. *Proceedings of the IEEE conference on computer vision and pattern recognition*, 3213-3223.
- Dai, J., He, K. & Sun, J., 2015. Convolutional feature masking for joint object and stuff segmentation. *Proceedings of the IEEE conference on computer vision and pattern recognition*, 3992-4000.
- Du Plessis, A., Olawuyi, B.J., Boshoff, W.P. & Le Roux, S.G., 2016. Simple and fast porosity analysis of concrete using x-ray computed tomography. *Materials structures*, 49 (1-2), 553-562.
- Fonseca, P. & Scherer, G., 2015. An image analysis procedure to quantify the air void system of mortar and concrete. *Materials and Structures*, 48 (10), 3087-3098.

- Gibbs, J.A., Pound, M., French, A.P., Wells, D.M., Murchie, E. & Pridmore, T., 2018. Plant phenotyping: An active vision cell for three-dimensional plant shoot reconstruction. *Plant physiology*, 178 (2), 524-534.
- Girshick, R., Donahue, J., Darrell, T. & Malik, J., 2014. Rich feature hierarchies for accurate object detection and semantic segmentation. *Proceedings of the IEEE conference on computer vision and pattern recognition*, 580-587.
- Guo, S., Dai, Q., Sun, X. & Sun, Y., 2016. Ultrasonic scattering measurement of air void size distribution in hardened concrete samples. *Construction and Building Materials*, 113, 415-422.
- Guo, Y., Liu, Y., Georgiou, T. & Lew, M.S., 2018. A review of semantic segmentation using deep neural networks. *International journal of multimedia information retrieval*, 7 (2), 87-93.
- Hariharan, B., Arbeláez, P., Girshick, R. & Malik, J., 2014. Simultaneous detection and segmentation. *European Conference on Computer Vision* Springer, 297-312.
- He, K., Zhang, X., Ren, S. & Sun, J., 2015. Spatial pyramid pooling in deep convolutional networks for visual recognition. *IEEE transactions on pattern analysis machine intelligence*, 37 (9), 1904-1916.
- He, K., Zhang, X., Ren, S. & Sun, J., 2016. Deep residual learning for image recognition. *Proceedings of the IEEE conference on computer vision and pattern recognition*, 770-778.
- Herrero-Huerta, M., Lindenbergh, R. & Gard, W., 2018. Leaf movements of indoor plants monitored by terrestrial lidar. *Frontiers in plant science*, 9, 189.

- Hill, R., Boyd, A., Dongell, J., Hichborn, G., Neal, R., Nmai, C., Lamond, J. & Leming, M., 2008. Guide to durable concrete reported by aci committee 201.
- Iglovikov, V., Seferbekov, S., Buslaev, A. & Shvets, A., 2018. Ternaustnetv2: Fully convolutional network for instance segmentation. *Proceedings of the IEEE Conference on Computer Vision and Pattern Recognition Workshops*, 233-237.
- Iglovikov, V. & Shvets, A., 2018. Ternaustnet: U-net with vgg11 encoder pre-trained on imagenet for image segmentation. *arXiv preprint arXiv:1808.05746*.
- Ikehata, S., Wipf, D., Matsushita, Y. & Aizawa, K., 2012. Robust photometric stereo using sparse regression. *2012 IEEE Conference on Computer Vision and Pattern Recognition*, United States. Rhode Island: IEEE, 318-325.
- Jay, S., Rabatel, G., Hadoux, X., Moura, D. & Gorretta, N., 2015. In-field crop row phenotyping from 3d modeling performed using structure from motion. *Computers and Electronics in Agriculture*, 110, 70-77.
- Kosmatka, S.H., Kerkhoff, B. & Panarese, W.C., 2002. *Design and control of concrete mixtures*: Portland Cement Association Skokie, IL.
- Krizhevsky, A., Sutskever, I. & Hinton, G.E., 2012. Imagenet classification with deep convolutional neural networks. *Advances in neural information processing systems*, 25, 1097-1105.
- Larson, T., Cady, P. & Malloy, J., 1967. The protected paste volume concept using new air-void measurement and distribution techniques. *Journal of Materials*.
- Lau, S.L., Chong, E.K., Yang, X. & Wang, X., 2020. Automated pavement crack segmentation using u-net-based convolutional neural network. *IEEE Access*, 8, 114892-114899.

- Liu, W., Rabinovich, A. & Berg, A.C., 2015. Parsenet: Looking wider to see bettered. *Computer Vision and Pattern Recognition*.
- Liu, W., Wen, Y., Yu, Z., Li, M., Raj, B. & Song, L., 2017. Sphreface: Deep hypersphere embedding for face recognition. *Proceedings of the IEEE conference on computer vision and pattern recognition*, 212-220.
- Long, J., Shelhamer, E. & Darrell, T., 2015. Fully convolutional networks for semantic segmentation. *Proceedings of the IEEE conference on computer vision and pattern recognition*, 3431-3440.
- Lopez-Sanchez, M.A. & Llana-Fúnez, S., 2016. An extension of the saltykov method to quantify 3d grain size distributions in mylonites. *Journal of Structural Geology*, 93, 149-161.
- Lu, B. & Torquato, S., 1992. Nearest-surface distribution functions for polydispersed particle systems. *Physical Review A*, 45 (8), 5530.
- Lu, H., Alymov, E., Shah, S. & Peterson, K., 2017. Measurement of air void system in lightweight concrete by x-ray computed tomography. *Construction Building Materials*, 152, 467-483.
- Lu, H., Peterson, K. & Chernoloz, O., 2018. Measurement of entrained air-void parameters in portland cement concrete using micro x-ray computed tomography. *International Journal of Pavement Engineering*, 19 (2), 109-121.
- Mayercsik, N.P., Felice, R., Ley, M.T. & Kurtis, K.E., 2014. A probabilistic technique for entrained air void analysis in hardened concrete. *Cement concrete research*, 59, 16-23.

- Miyazaki, D., Hara, K. & Ikeuchi, K., 2010. Median photometric stereo as applied to the segonko tumulus and museum objects. *International Journal of Computer Vision*, 86 (2-3), 229.
- Mostajabi, M., Yadollahpour, P. & Shakhnarovich, G., 2015. Feedforward semantic segmentation with zoom-out features. *Proceedings of the IEEE conference on computer vision and pattern recognition*, 3376-3385.
- Murotani, T., Igarashi, S. & Koto, H., 2019. Distribution analysis and modeling of air voids in concrete as spatial point processes. *Cement Concrete Research*, 115, 124-132.
- Pade, C., Jakobsen, U. & Elsen, J., 2002. A new automatic analysis system for analyzing the air void system in hardened concrete. *International cement microscopy association*, Metropolis, Illinois, 204-213.
- Paszke, A., Chaurasia, A., Kim, S. & Culurciello, E., 2016. Enet: A deep neural network architecture for real-time semantic segmentation. *Computer Vision and Pattern Recognition*.
- Paulus, S., Schumann, H., Kuhlmann, H. & Léon, J., 2014. High-precision laser scanning system for capturing 3d plant architecture and analysing growth of cereal plants. *Biosystems Engineering*, 121, 1-11.
- Peterson, K., Van Dam, T. & Sutter, L., 2001a. Determination of the paste to void proximity distribution in two dimensions from a cross-section through a concrete specimen. *Proceedings of the Eighth Euroseminar on Microscopy Applied to Building Materials*, 4-7.

- Peterson, K.W., Anzalone, G.C., Nezami, S., Oh, C.Y.S. & Lu, H., 2016. Robust test of the flatbed scanner for air-void characterization in hardened concrete. *Journal of Testing Evaluation*, 44 (1), 599-614.
- Peterson, K.W., Swartz, R.A., Sutter, L.L. & Van Dam, T.J., 2001b. Hardened concrete air void analysis with a flatbed scanner. *Transportation Research Record*, 1775 (1), 36-43.
- Philleo, R., 1983. A method for analyzing void distribution in air-entrained concrete. *Cement, concrete aggregates*, 5 (2), 128-130.
- Pleau, R., Pigeon, M. & Laurencot, J.L., 2001. Some findings on the usefulness of image analysis for determining the characteristics of the air-void system on hardened concrete. *Cement Concrete Composites*, 23 (2-3), 237-246.
- Pound, M.P., French, A.P., Fozard, J.A., Murchie, E.H. & Pridmore, T.P., 2016. A patch-based approach to 3d plant shoot phenotyping. *Machine Vision Applications*, 27 (5), 767-779.
- Pound, M.P., French, A.P., Murchie, E.H. & Pridmore, T.P., 2014. Automated recovery of three-dimensional models of plant shoots from multiple color images. *Plant physiology*, 166 (4), 1688-1698.
- Powers, T.C. & Willis, T., 1950. The air requirement of frost resistant concrete. *Highway Research Board Proceedings*.
- Quéau, Y., Wu, T., Lauze, F., Durou, J.D. & Cremers, D., 2017. A non-convex variational approach to photometric stereo under inaccurate lighting. *Proceedings of the IEEE Conference on Computer Vision and Pattern Recognition*, 99-108.

- Rashed, A.I. & Williamson, R.B., 1991. Microstructure of entrained air voids in concrete, part i. *ournal of materials research*, 6 (9), 2004-2012.
- Ronneberger, O., Fischer, P. & Brox, T., 2015. U-net: Convolutional networks for biomedical image segmentation. *International Conference on Medical image computing and computer-assisted intervention* Springer, 234-241.
- Russ, J.C. & Dehoff, R.T., 2012. *Practical stereology*: Springer Science & Business Media.
- Sahagian, D.L. & Proussevitch, A.A., 1998. 3d particle size distributions from 2d observations: Stereology for natural applications. *Journal of Volcanology Geothermal Research*, 84 (3-4), 173-196.
- Saltykov, S.A., 1958. *Stereometric metallography* Metallurgizdat, Moscow.
- Saucier, F., Pleau, R. & Vézina, D., 1996. Precision of the air void characteristics measurement by astm c 457: Results of an interlaboratory test program. *Canadian Journal of Civil Engineering*, 23 (5), 1118-1128.
- Scherer, G.W. & Valenza, J., 2005. Mechanisms of frost damage. *Materials science of concrete*, 7 (60), 209-246.
- Schouenborg, B., Lindqvist, J.-E. & Sandström, M., 1995. *Air and air void structures in concrete-general overview and picture atlas*. Sweden: Institute, S.N.T.a.R., Nordtest project 1121-93.
- Shafer, S.A., 1985. Using color to separate reflection components. *Color Research Application*, 10 (4), 210-218.
- Shi, J., Wu, K., Yang, C. & Deng, N., 2021. A method of steel bar image segmentation based on multi-attention u-net. *IEEE Access*, 9, 13304-13313.

- Simon, M., 2005. *An interlab evaluation of the variability in the astm c 457 linear traverse method.*
- Simonyan, K. & Zisserman, A., 2014. Very deep convolutional networks for large-scale image recognition. *arXiv preprint arXiv.*
- Snyder, K., Hover, K. & Natesaiver, K., 1991. An investigation of the minimum expected uncertainty in the linear traverse technique. *Cement, concrete aggregates*, 13 (1), 3-10.
- Snyder, K.A., 1998. A numerical test of air void spacing equations. *Advanced cement based Materials*, 8 (1), 28-44.
- Song, Y., Damiani, R.M., Shen, C., Castaneda, D.I. & Lange, D.A., 2020a. A 3d petrographic analysis for concrete freeze-thaw protection. *Cement and Concrete Research*, 128.
- Song, Y., Huang, Z., Shen, C., Shi, H. & Lange, D.A., 2020b. Deep learning-based automated image segmentation for concrete petrographic analysis. *Cement and Concrete Research*, 135.
- Song, Y., Shen, C., Damiani, R.M. & Lange, D.A., 2021. Image-based restoration of the concrete void system using 2d-to-3d unfolding technique. *Construction and Building Materials*, 270.
- Song, Y., Zou, R., Castaneda, D., Riding, K. & Lange, D., 2017. Advances in measuring air-void parameters in hardened concrete using a flatbed scanner. *Journal of Testing Evaluation*, 45 (5), 1713-1725.
- Stock, S., 2008. Recent advances in x-ray microtomography applied to materials. *International Materials Reviews*, 53 (3), 129-181.

- Sun, L. & Wang, Y., 2017. Three-dimensional reconstruction of macrotexture and microtexture morphology of pavement surface using six light sources-based photometric stereo with low-rank approximation. *Journal of Computing in Civil Engineering*, 31 (2), 04016054.
- Szegedy, C., Liu, W., Jia, Y., Sermanet, P., Reed, S., Anguelov, D., Erhan, D., Vanhoucke, V. & Rabinovich, A., 2015. Going deeper with convolutions. *Proceedings of the IEEE conference on computer vision and pattern recognition*, 1-9.
- Szegedy, C., Reed, S., Erhan, D., Anguelov, D. & Ioffe, S., 2014. Scalable, high-quality object detection. *arXiv preprint arXiv:*.
- Tang, K.L., Tang, C.K. & Wong, T.T., 2005. Dense photometric stereo using tensorial belief propagation. *2005 IEEE Computer Society Conference on Computer Vision and Pattern Recognition (CVPR'05)*IEEE, 132-139.
- Tasar, O., Tarabalka, Y. & Alliez, P., 2019. Incremental learning for semantic segmentation of large-scale remote sensing data. *IEEE Journal of Selected Topics in Applied Earth Observations Remote Sensing of Environment*, 12 (9), 3524-3537.
- Thapa, S., Zhu, F., Walia, H., Yu, H. & Ge, Y., 2018. A novel lidar-based instrument for high-throughput, 3d measurement of morphological traits in maize and sorghum. *Sensors*, 18 (4), 1187.
- Tipping, M.E., 2001. Sparse bayesian learning and the relevance vector machine. *Journal of machine learning research*, 1 (Jun), 211-244.

- Uijlings, J.R., Van De Sande, K.E., Gevers, T. & Smeulders, A.W., 2013. Selective search for object recognition. *International journal of computer vision*, 104 (2), 154-171.
- Walker, H.N., Lane, D.S. & Stutzman, P.E., 2006. *Petrographic methods of examining hardened concrete: A petrographic manual*. United States.
- Wan, J., Wang, D., Hoi, S.C.H., Wu, P., Zhu, J., Zhang, Y. & Li, J., 2014. Deep learning for content-based image retrieval: A comprehensive study. *Proceedings of the 22nd ACM international conference on Multimedia*, 157-166.
- Wawrzeńczyk, J. & Kozak, W., 2016. Protected paste volume (ppv) as a parameter linking the air-pore structure in concrete with the frost resistance results. *Construction Building Materials*, 112, 360-365.
- Wolter, S., Uhre, F.a.H., Hasholt, M.T., Dahl, V.A. & Anton, F., 2019. Air void analysis of hardened concrete by means of photogrammetry. *Construction and Building Materials*, 226, 953-964.
- Woodham, R.J., 1980. Photometric method for determining surface orientation from multiple images. *Optical engineering*, 19 (1), 191139.
- Wu, L., Ganesh, A., Shi, B., Matsushita, Y., Wang, Y. & Ma, Y., 2010. Robust photometric stereo via low-rank matrix completion and recovered. *Asian Conference on Computer Vision* Springer, 703-717.
- Yeon, J.H. & Kim, K.-K., 2018. Potential applications of phase change materials to mitigate freeze-thaw deteriorations in concrete pavement. *Construction and Building Materials*, 177, 202-209.

- Yu, F. & Koltun, V., 2015. Multi-scale context aggregation by dilated convolutionsed. *Computer Vision and Pattern Recognition*.
- Yun, T.S., Kim, K.Y., Choo, J. & Kang, D.H., 2012. Quantifying the distribution of paste-void spacing of hardened cement paste using x-ray computed tomography. *Materials characterization*, 73, 137-143.
- Zalocha, D. & Kasperkiewicz, J., 2005. Estimation of the structure of air entrained concrete using a flatbed scanner. *Cement Concrete research*, 35 (10), 2041-2046.
- Zhang, A., Wang, K.C., Fei, Y., Liu, Y., Tao, S., Chen, C., Li, J.Q. & Li, B., 2018. Deep learning-based fully automated pavement crack detection on 3d asphalt surfaces with an improved cracknet. *Journal of Computing in Civil Engineering*, 32 (5), 04018041-1-04018041-14.
- Zhou, S., Wu, J.-N., Wu, Y. & Zhou, X., 2015. Exploiting local structures with the kronecker layer in convolutional networksed. *Computer Vision and Pattern Recognition*.